DETERMINING TEMPERATURES OF DEFORMATION IN MYLONITES FROM THE SCANDINAVIAN CALEDONIDES, WITH IMPLICATIONS FOR THE THERMAL AND KINEMATIC EVOLUTION OF OROGENS

by

Andrea Marilina Wolfowicz

A thesis

submitted in partial fulfillment

of the requirements for the degree of

Master of Science in Geosciences

Boise State University

December 2012

BOISE STATE UNIVERSITY GRADUATE COLLEGE

DEFENSE COMMITTEE AND FINAL READING APPROVALS

of the thesis submitted by

Andrea Marilina Wolfowicz

Thesis Title: Determining Temperatures of Deformation in Mylonites from the Scandinavian Caledonides, with Implications for the Thermal and Kinematic Evolution of Orogens.

Date of Final Oral Examination: 28 August 2012

The following individuals read and discussed the thesis submitted by student Andrea Marilina Wolfowicz, and they evaluated her presentation and response to questions during the final oral examination. They found that the student passed the final oral examination.

Matthew J. Kohn, Ph.D. Co-chair, Supervisory Committee

Clyde J. Northrup, Ph.D. Co-chair, Supervisory Committee

Walter S. Snyder, Ph.D. Member, Supervisory Committee

The final reading approval of the thesis was granted by Matthew J. Kohn, Ph.D. and Clyde J. Northrup, Ph.D., Co-chairs of the Supervisory Committee. The thesis was approved for the Graduate College by John R. Pelton, Ph.D., Dean of the Graduate College.

ACKNOWLEDGMENTS

I would like to thank the entire department of geosciences at Boise State University. In particular, I would like to thank my advisors, Dr. Matt Kohn, and Dr. CJ Northrup, for their supervision and guidance over the past two years; Dr. Stacey Corrie, for not only being a wonderful mentor, but also for gathering my garnet X-ray images and electron-microprobe data; Dr. Jim Crowley and Deborah Pierce for their help with sample preparation; and my friends, the other graduate students, for providing some much needed distractions, and making my time in Idaho unforgettable.

I would like to extend my thanks to Dr. Richard Hervig and Dr. Lynda Williams at the School of Earth and Space Exploration at Arizona State University, for helping me use the Secondary Ion Mass Spectrometer, even when it meant coming into the lab at all hours of the night.

Last but not least, I want to thank my family for their love and support, and Michael, for making me happy, and for using up all his vacation time to visit me in Idaho.

ABSTRACT

The Titanium-in-quartz (TitaniQ) thermobarometer was evaluated in ductilely sheared rocks (mylonites) from the Scandinavian Caledonides in comparison with several other thermometric methods, including: (1) TitaniQ thermometry in cross-cutting quartz veins, (2) garnet-biotite Fe-Mg exchange thermometry, (3) metamorphic phase equilibria, and (4) quartz microstructures as calibrated experimentally and empirically. In all instances, quartz vein temperatures mimic TitaniQ temperatures of the host rocks. Similarly, TitaniQ temperatures of dynamically recrystallized quartz, ranging from ~210°C at the thrust front to 475°C at the deepest structural levels, reflect the best estimate of the final temperature of deformation. Higher temperatures are also preserved locally and more closely reflect peak metamorphic temperatures derived from metamorphic phase equilibria. Of the two samples analyzed for garnet-biotite Fe-Mg exchange thermometry, one gives results consistent with TitaniQ temperatures and the other gives a higher temperature. A larger sample size would be necessary for more confident comparisons. Lastly, TitaniQ temperatures are mostly consistent with temperatures expected from quartz microstructures. However, TitaniQ temperatures reveal grain boundary migration recrystallization (GBM) occurred at temperatures as low as 340°C, which is much lower than previously published temperatures for GBM (Hirth and Tullis, 1992; Stipp et al., 2002).

Two competing end-member models for the steady state thermal and kinematic evolution of orogens exist: The critical wedge model and the channel flow-extrusion model. Due to the unusual and consistent exposure of thrust surfaces for ~140 km across the orogen, the Caledonides provide insights into the down-dip behavior of thrusts not determinable in other collisional orogens. Using TitaniQ, in combination with other thermometers and barometers, to obtain precise and accurate pressure-temperature estimates of quartz recrystallization in the Northern Scandinavian Caledonides, we resolve a consistent down-dip thermal gradient along the basal thrust shear zone of 1.43 ± 2°C/km. This low thermal gradient supports the critical wedge model for the evolution of the Caledonides. We suggest that the Caledonides formed from critical wedge mechanics together with general non-coaxial flow and gravitational spreading of the nappes. In addition to resolving a down-dip thermal gradient across the Caledonides basal shear zone, we calculated strain rates for quartz deformation ranging from $1.00E^{-22}$ to $1.00E^{-13}$ s^{-1}.

TABLE OF CONTENTS

LIST OF TABLES

LIST OF FIGURES

CHAPTER ONE: DETERMINING TEMPERATURES OF DEFORMATION IN MYLONITES FROM THE SCANDINAVIAN CALEDONIDES

Abstract

The Titanium-in-quartz (TitaniQ) thermobarometer was evaluated in ductilely sheared rocks (mylonites) from the Scandinavian Caledonides in comparison with several other thermometric methods, including: (1) TitaniQ thermometry in cross-cutting quartz veins, (2) garnet-biotite Fe-Mg exchange thermometry, (3) metamorphic phase equilibria, and (4) quartz microstructures as calibrated experimentally and empirically. In all instances, quartz vein temperatures mimic TitaniQ temperatures of the host rocks. Similarly, TitaniQ temperatures of dynamically recrystallized quartz, ranging from ~210°C at the thrust front to 475°C at the deepest structural levels, reflect the best estimate of the final temperature of deformation. Higher temperatures are also preserved locally and more closely reflect peak metamorphic temperatures derived from metamorphic phase equilibria. Of the two samples analyzed for garnet-biotite Fe-Mg exchange thermometry, one gives results consistent with TitaniQ temperatures and the other gives a higher temperature. A larger sample size would be necessary for more confident comparisons. Lastly, TitaniQ temperatures are mostly consistent with temperatures expected from quartz microstructures. However, TitaniQ temperatures reveal grain boundary migration recrystallization (GBM) occurred at temperatures as low as 340°C, which is much lower than previously published temperatures for GBM (Hirth and Tullis, 1992; Stipp et al., 2002).

1.1 Introduction

Presently, only a few methods are available to determine temperatures of deformation in ductilely sheared rocks (mylonites) because typical temperatures of mylonitization (<500°C to ~250°C) are not readily estimated by cation-exchange thermometers or mineral equilibria (Kohn and Northrup, 2009). Most temperatures of mylonitization are based empirically on deformation microstructures in quartz and feldspar, and the uncertainties remain large (at least ± 50°C; and strain rate dependent). To address this problem, we have evaluated the Ti-in-Qtz thermobarometer (TitaniQ) as a possible new way of determining temperatures of deformation in mylonites. Kohn and Northrup (2009) have shown that Ti contents of quartz change during mylonitization, which may allow for precise and accurate temperature estimates of dynamic recrystallization.

TitaniQ was evaluated in mylonites from the well exposed main basal thrust zone (MBT) of the Scandinavian Caledonides (Figure 1.1) in comparison with several other thermometric methods, including: (1) TitaniQ thermometry in cross-cutting quartz veins, (2) garnet-biotite Fe-Mg exchange thermometry, (3) metamorphic phase equilibria, and (4) quartz microstructures as calibrated experimentally and empirically.

In principle, recrystallized quartz might record temperatures attained prior to, during, or after the peak of metamorphism, or even relict temperatures inherited from the igneous protolith. However, mylonites texturally postdate the peak of metamorphism (Northrup, 1996b), so quartz grains that recrystallized during mylonitization should record lower temperatures than either the metamorphic peak or igneous cooling.

We analyzed TitaniQ temperatures in cross-cutting quartz veins (T_{qv}) in addition to host-rock mylonites (T_{hm}) for two reasons. First, if temperatures were decreasing during deformation, then quartz veins that postdate deformation should yield $T_{qv} \leq T_{hm}$. Second, quartz veins should have precipitated directly from a fluid, so should not contain relict grains that were inherited from the protolith or that are reflective of earlier conditions. Therefore, neoblastic quartz veins allowed us to independently check that we were sampling recrystallized quartz and not relict igneous and metamorphic grains (Figure 1.2).

We expected garnet-biotite (peak metamorphic)/Fe-Mg temperatures to exceed TitaniQ temperatures as deformation texturally post-dates metamorphism. Since the MBT of the Scandinavian Caledonides formed at conditions ranging from the mid-amphibolite facies in the west to the brittle-ductile transition at the east, we expected TitaniQ temperatures to fall within this range in temperatures (~600°C - ~280°C) across the orogen. Lastly, we expected that TitaniQ temperatures and quartz microstructures would coincide with the dynamic recrystallization regimes and associated temperatures defined by Hirth and Tullis (1992) and Stipp et al. (2002).

1.2 Background

1.2.1 The Scandinavian Caledonides

The Scandinavian Caledonides represent an ancient orogenic system that reflects the dynamic interaction between contractional and extensional processes (Northrup, 1996a). In the early Paleozoic, closure of the Iapetus Ocean and the subduction of the western margin of Baltica beneath Laurentia formed a crustal scale composite allochthon

that was thrust eastward onto the Baltic craton (Griffin and Brueckner, 1980). Erosion and extension have removed or displaced much of the original allochthon and have exposed deep crustal levels of the Caledonian Orogen. Now, the Scandinavian Caledonides consist of a relatively thin, but regionally extensive remnant of the original nappe stack, which lies structurally above autochthonous or parautochthonous rocks of the Baltic craton and its pre-Caledonian sedimentary cover (Roberts and Gee, 1985). The basal shear zone, or the MBT, separates rocks of the composite Caledonian allochthon from parautochthonous structural basement (Northrup, 1996a). The present day erosional surface closely follows the structure level at the base of the nappe stack, so progressively greater depths are exposed westward, down-dip. Mylonites in the basal shear zone contain well-developed L-S deformational fabrics, and the foliation is parallel to the structural contact at the base of the allochthon (Northrup, 1996a). The stretching lineation and inferred transport direction in the basal shear zone trends to the ESE.

Today, remnants of the original nappe stack are found in Norway, Sweden, Greenland, the British Isles, and north-central Europe. The Baltic craton can be followed from the thrust front in Sweden, via antiformal windows, to the west coast of Norway (Gee et al., 2010). Although several different orogenic events occurred in the lower Paleozoic, the Scandian, at c. 400 Ma, was the only one to affect the craton and its immediate parautochthonous cover (Roberts and Gee, 1985).

1.2.2 The Titanium in Quartz Thermobarometer (TitaniQ)

Both Silicon (Si) and Titanium (Ti) are tetravalent cations so Ti^{4+} substitutes for Si^{4+}, without having to be charge balanced by coupled substitution of another element (Wark and Watson, 2006). The equilibrium concentration of Ti^{4+} at a particular

temperature is governed by partitioning. For Ti-in-qtz, higher temperatures stabilize higher Ti contents.

Wark and Watson (2006) synthesized quartz in the presence of rutile at 600 to 1000°C at 10 kbar and showed dependence of the Ti content in quartz on temperature: $T(K) = -3765/[\log(X_{Ti,qtz}/aTiO2)] - 5.69$ where the Ti content is in ppm (by weight), and $aTiO_2$ is the activity of TiO_2 relative to that required for rutile saturation (aTiO2 =1; Wark and Watson, 2006). Thomas et al. (2010) synthesized quartz in the presence of rutile at 600 to 1000°C at 0.5-2.0 GPa and showed the dependence of the Ti content in quartz on both temperature and pressure: $RT\ln X_{qtz,TiOx} = -60952 + 1.520*T(K) - 1741*P(kbar) + RT\ln_{aTiO2}$, where R is the ideal gas constant (8.3145 J/K), X is the mole fraction of TiO_2 in quartz, and $aTiO_2$ is the activity of TiO_2 in the system (Thomas et al., 2010).

The resulting titanium-in-quartz thermobarometer (TitaniQ) has several advantages over other existing thermobarometers; most importantly, it can be applied over a wide range of rock types because quartz, the only phase that requires analysis, is stable over a wide range of temperatures and pressures (Cherniak et al., 2006; Wark and Watson, 2006). Also, as long as there is measureable Ti in the system, the system does not have to be saturated with respect to rutile (Wark and Watson, 2006). Another advantage is that domains with different Ti-content can be targeted for analysis since cathodoluminescence (CL) intensity correlates with trace element content (Rusk et al., 2008; Spear and Wark, 2009; Kohn and Northrup, 2009). Lastly, TitaniQ is unusually precise (±3°C at a specified pressure; Wark and Watson, 2006).

TitaniQ's main disadvantage is its moderate pressure-dependence. The original TitaniQ calibration (Wark and Watson, 2006) can be used to accurately determine quartz crystallization temperature for pressures near 10 kbar (Thomas et al., 2010). However, with increasing pressures, Ti-in-quartz solubility becomes unfavorable because Ti^{4+} is ~38 % larger than the tetrahedrally coordinated Si^{4+} in the quartz structure, and because quartz is anomalously compressible (Levien et al., 1980). Therefore, accurately assigning temperatures requires simultaneous application of another thermobarometer. We make a pressure correction by assuming a pressure at each location, in part based on conventional thermobarometry, to determine temperatures of deformation.

1.2.3 Ti diffusion in Quartz

The growth history of quartz may be recorded in fine-scale zoning of trace elements in individual quartz grains (Cherniak et al., 2006). Some of this zoning may be observable via variations in CL intensity, and higher Ti concentrations in quartz correlate to a higher CL intensity. Cherniak and Watson (2007) measured Ti diffusion in synthetic and natural quartz under dry 1-atm conditions. An Arrhenius relation was obtained for diffusion parallel to (001), which indicates that Ti may diffuse ~500 μm at 800°C and ~15 μm at 600°C in a million years. For temperatures of mylonitization (300-500°C), characteristic length scales for diffusion are only .001- 2 μm for a time scale of 1 m.y (Cherniak and Watson, 2007). Therefore, quartz grains that reequilibrate during recrystallization below ~500 °C will retain their compositions (Kohn and Northrup, 2009).

Consequently, thermal information provided by TitaniQ in our study depends on the temperature at which a grain or domain last recrystallized. Zoning in quartz in

mylonitic rocks may result from recrystallization of different domains at different temperatures, or from progressive growth of the quartz grains during changes in P-T conditions.

1.2.4 Deformation, Recovery, and Dynamic Recrystallization

When a differential stress acts upon a crystal at moderate to high temperatures, lattice imperfections, or dislocations, are introduced into the crystal structure, increasing the internal strain energy of the crystal. These dislocations are free to migrate through the crystal in the direction of the sense of shear, after the critical resolved shear stress is exceeded, by dislocation glide and dislocation climb, together referred to as dislocation creep. Effectively, the internal strain energy of the crystal is relieved and the crystal changes shape without loss of cohesion to the crystal structure. This process is known as ductile deformation.

Ductile deformation is accompanied by processes known as recovery and dynamic recrystallization. During recovery, dislocations will concentrate in discrete zones, or deformation bands, in the crystal. This has the effect of decreasing the dislocation density in other parts of the crystal. These parts of the crystal are referred to as subgrains, and they are separated from adjacent parts of the crystal by sharp, low relief boundaries. The crystal lattices of subgrains on either side of a deformation band may differ by up to 5° (Fitzgerald et al., 1983; White and Mawer, 1988).

Non-recovered deformation in a crystal is evidenced by undulose extinction. Undulose extinction may be sweeping, due to a large scale, regular bending of the crystal due to dislocations, or it may be patchy or irregular. Patchy or irregular extinction results from microkinks and microfractures in the crystal lattice, which is probably due to

cataclastic failure at site of dislocation tangles (Hirth and Tullis, 1992). Deformation lamellae, which consist of long, thin, solid and fluid inclusion trails, elongate subgrains, and dislocation tangles, may also be present in a deformed crystal. A lattice preferred orientation may indicate that deformation occurred by dislocation creep (Passchier and Trouw, 1998). At high temperatures, recovery and recrystallization may erase evidence for intra-crystalline deformation.

Dynamic recrystallization may be evidenced by a partially recrystallized fabric or a completely recrystallized fabric. A bimodal grain size distribution characterizes a partially recrystallized fabric. Aggregates of small grains with uniform extinction occur adjacent to larger grains with undulose extinction. The large grains will contain subgrains of approximately the same size as the small grains. However, a completely recrystallized fabric may sometimes be difficult to distinguish from a non-deformed, fine-grained rock. Evidence of complete recrystallization comes from a lattice preferred orientation of grains (LPO), and irregular grain boundaries due to pinning microstructures, window microstructures, dragging microstructures, and left-over grains (Figure 1.3; Passchier and Trouw, 1998).

The three main dynamic recrystallization mechanisms operative in quartz are Subgrain Rotation recrystallization (SR), Grain Boundary Migration recrystallization (GBM), and Bulging recrystallization (BLG; Figure 1.3). SR is caused by the progressive misorientation of subgrain crystal lattices on either side of a subgrain boundary. The progressive misorientation is due to the continued migration of dislocations by dislocation creep to these subgrain boundaries. Grains recrystallized by SR are recognized by core and mantle structures in which small, recrystallized grains surround

larger grains that contain subgrains of approximately the same size as the recrystallized grains (Passchier and Trouw, 1998; Hirth and Tullis, 1992; Stipp et al., 2002). However, core and mantle structures are not present in all samples that recrystallized by SR.

GBM, on the other hand, is driven by differences in dislocation densities between neighboring grains: if a very deformed grain with a high dislocation density neighbors a less deformed grain with a lower dislocation density, then atoms from the more deformed grain may migrate into the less deformed grain. In effect, the less deformed grain grows at the expense of the more deformed grain. Grains that recrystallized by GBM are recognized by their shape and size: The recrystallized grains are all approximately the same size and they have straight but irregular grain boundaries (Passchier and Trouw, 1998; Hirth and Tullis, 1992; Stipp et al., 2002).

BLG, like GBM, is also driven by differences in dislocation densities between neighboring grains. However, during BLG, movement of the grain boundary occurs over a localized area and not throughout the entire grain boundary. Grains that recrystallized by BLG are recognized by their irregular grain boundaries and bulges. Sometimes the bulges pinch off and form smaller, separate, recrystallized grains (Passchier and Trouw, 1998; Hirth and Tullis, 1992; Stipp et al., 2002).

Dynamic recrystallization mechanisms in quartz have been studied both experimentally and empirically. Hirth and Tullis (1992) identified three different dislocation creep regimes in experimentally deformed quartz aggregates, operative over different temperature ranges. Stipp et al. (2002) also identified three regimes in naturally deformed quartz veins in the Eastern Tonale strike-slip shear zone, Italian Alps, which were characterized by these different dynamic recrystallization mechanisms.

Temperatures across the shear zone were estimated from metamorphic phase equilibria. The microstructures and temperatures associated with the different dynamic recrystallization mechanisms in this 'natural laboratory,' for a presumed strain rate, correlate with the dislocation creep regimes defined by Hirth and Tullis (1992): BLG dominates from 280 to 400°C, SR dominates from 400 to 500°C, and both SR and GBM dominate from 500 to 700°C.

However, there are large uncertainties (at least ± 50°C) associated with determining temperatures of deformation in mylonites from deformation textures in quartz. There are two main sources for these uncertainties: First, although each of these different dynamic recrystallization mechanisms is dominant in quartz at different temperatures, each mechanism is, in fact, operative at all temperatures (Hirth and Tullis, 1992; Stipp et al., 2002). Second, the mechanical behavior of quartz is not only dependent on temperature, but also on strain rate (Hirth and Tullis, 1992). More precise temperature estimates would allow us to determine more accurate strain rates and effective viscosities of crustal materials (Kohn and Northrup, 2009).

1.2.5 Exchange Equilibria and Net Transfer Equilibria

The formal thermodynamic relationship among pressure, temperature, and mineral composition can be defined by the fundamental thermodynamic equation (Spear, 1993):

$$\Delta G(P,T,X) = 0$$

$$= \Delta H(298,1) + \int_{298}^{T} \Delta C_p dT + \int_{1}^{P} \Delta V dP - T[\Delta S(298,1) + \int_{298}^{T} \frac{\Delta C_p}{T} dT]$$

$$+ RTlnK_{eq}$$

Values of enthalpy, entropy, specific heat capacity, and volume are known from experimental calibrations or thermodynamic tables, and the value of the equilibrium constant is measured for a sample by determining the compositions of minerals. A unique equilibrium constant exists at each temperature and pressure and is thus sensitive to changes in pressure and temperature. The pressure and temperature dependence of the equilibrium constant (K_{eq}) is used to calculate metamorphic pressures and temperatures of equilibrium for a sample. After determining the K_{eq} of a sample, a line of constant K_{eq} can be drawn on a P-T diagram and it is inferred that the sample equilibrated somewhere along this line.

If two different equilibria can be evaluated, then the intersection of the two lines defines a unique pressure and temperature of equilibration. Two such equilibria are the garnet biotite Fe-Mg exchange thermometer (Ferry and Spear, 1978), and the garnet-biotite-muscovite-plagioclase barometer (Ghent and Stout, 1981; Hoisch, 1990). These equilibria allow calculation of equilibrium temperatures and pressures from the measured distribution of elements among coexisting phases (Winter, 2001).

1.2.6 Fe-Mg Garnet Biotite Exchange Geothermometer

Reactions that show strong temperature dependence of the equilibrium constant are good geothermometers. One such geothermometer is the garnet-biotite Fe-Mg

exchange geothermometer. The distribution of Fe and Mg between garnet and biotite is a function of pressure and temperature, and the differential discrimination of Fe and Mg between garnet and biotite decreases as temperature increases. This occurs because the energetic distinction between different elements becomes smaller as temperatures increase, so the crystals display less of a preference for one element over another (Spear, 1993).

Ferry and Spear (1978) calibrated the partitioning of Fe and Mg between Ca-free garnet, $(Fe, Mg)_3Al_2Si_3O_{12}$, and biotite, $K(Fe, Mg)_3AlSi_3O_{10}(OH)_2$ in the cation exchange reaction $Fe_3Al_2Si_3O_{12} + KMg_3AlSi_3O_{10}(OH)_2 = Mg_3Al_2Si_3O_{12} + KFe_3AlSi_3$-$O_{10}(OH)_2$. In their experiments, biotite was equilibrated with a reservoir of garnet of a known composition at temperatures ranging from 550 to 800°C. The equilibrium constant was calculated at each experimental temperature and the composition of the biotite was analyzed by electron microprobe. The results of this experiment yielded a geothermometer for rocks containing garnet and biotite, which appears to work well for low-Ca garnets in the greenschist and amphibolite facies (Winter, 2001).

1.2.7 Garnet-Biotite-Muscovite-Plagioclase Geobarometer

Equilibrium reactions, such as net transfer reactions that show strong pressure dependence of the equilibrium constant, are good barometers. Net transfer reactions cause the production and consumption of phases and therefore result in relatively large changes in volume, which makes the equilibrium constant sensitive to changes in pressure. Garnet bearing rocks that crystallized at low pressures and high temperature contain garnets with low grossular (Ca end-member) contents and anorthitic plagioclases (Ca end-member), whereas those that crystallized at high pressures and low temperatures

contain garnets with high grossular contents and plagioclase with low anorthite contents. The ratio of grossular to anorthite in the presence of quartz and micas defines the equilibrium constant.

An electron microprobe may be used to measure the compositions of coexisting garnet, plagioclase, and micas, which are used to infer the activity of each phase (Spear, 1993). However, caution must be taken when selecting which garnet compositions to pair with biotite, muscovite, and plagioclase compositions for temperature and pressure calculations: typical garnets are compositionally zoned, and retrograde net transfer reactions (ReNTRs) may increase zoning complexity. In a compositionally growth-zoned garnet, Mn decreases rim-ward while Fe and Mg increase rim-ward. During (ReNTRs), the garnet dissolves and Mn piles upon the garnet rim, yielding an increase in Mn along the rim (known as the 'Mn kick-up'), since garnet is one of the few phases that takes in Mn (Kohn and Spear, 2000). The trough (the inner rim), which retains the highest retrievable temperature conditions, and is associated most closely with peak metamorphic temperatures, can be resolved by looking at garnet X-ray maps. It is advisable to pair trough compositions with distal biotite compositions to ensure against local re-equilibration of biotite with garnet.

1.3 Methods of Analyses - Data Collection and Interpretation

Fifty-five samples of granite mylonites, schists, marbles, quartzites, and quartz veins were collected across a NW-SE transect from the Northern Scandinavian Caledonides in Norway and Sweden in the summer of 2010. Collection spanned the Narvik/Harstad area in northwestern Norway to the Kiruna region in northern Sweden. Polished oriented thin sections were then prepared perpendicular to foliation and parallel

to lineation for petrographic analysis. Mineral assemblages, microstructures, and deformation textures were characterized for each sample (see Appendix and Tables 1.1 and 1.3).

The samples were then organized into 11 groups (groups A through K) based on their collection location: A = SC10-26 to -31; B =SC10-17 to -25; C = SC10-01 to -16; D = SC10-39 and SC10-42; E = SC10-43 to -45; F = SC10-32 to -37, and SC10-40 to -41; G = SC10-46; H = SC10-47 to -48; J = SC10-51 to -54; I = SC10-49 to -50; and K = SC10-55. These collection groups were projected onto a NW-SE line that was drawn parallel to the transport direction of the nappes (Figure 1.1).

Most samples in a group recrystallized in the same manner, and transitions between dislocation creep regimes were drawn perpendicular to the main transport direction of the nappes (Figure 1.4). At least one sample from each group was selected for further analyses. A total of twenty-three samples that contained rutile and that contained representative microstructures were petrographically characterized and selected for further analyses. Two of the twenty-three samples also contained garnet, biotite, plagioclase, and muscovite.

1.3.1 Secondary Ion Mass Spectrometer Chemical Analysis

The twenty-three samples that were selected for further analyses were carbon coated and then imaged with a JEOL T300 scanning electron microscope (SEM)—using a mounted Gatan Mini-cathodoluminescence (CL) detector at Boise State University. Locations for secondary ion mass spectrometry (SIMS) analyses were targeted using CL textures and intensities within and between quartz grains because CL intensity correlates with trace element content. Carbon coats were then removed by polishing with 0.3 μm

alumina, and selected areas were drilled from the polished thin sections using a drill press and a 5 mm diamond studded drill bit, producing 5 mm diameter rounds.

The polished thin section rounds were then mounted in a one inch epoxy round along with a Herkimer "diamond", a low temperature quartz that formed at 150-200°C (Smith, 2006), so should contain Ti concentrations 3 ± 2.5 ppb (Kohn and Northrup, 2009), and a natural quartz crystal from a Himalayan migmatite (LT01-15), whose Ti contents were determined by electron and ion microprobes (33 ± 9 ppm Ti; Kohn and Northrup, 2009). The Herkimer "diamond" and natural quartz sample acted as a quartz "blank" and a standard, respectively, and were mounted and polished before being remounted with the samples. A total of 9 mounts were made with two to three sample rounds, one Herkimer quartz standard, and one natural quartz standard per mount (Figure 1.5). The rounds and standards were positioned within the inner 1.1 cm of the mount. For low Ti samples, Ti contamination during sample preparation can be a risk. So, we used Epofix resin to mount the samples since it has a low Ti concentration, a low viscosity, and it sets quickly with low volatility (Engwell and Hall, 2008). The mounts were then photographed in reflected light (Figure 1.6) and specific locations on each sample were selected for SIMS spot analyses. Selecting specific locations for analyses allowed for greater microstructural control, and analytical efficiency.

At Arizona State University, the nine mounts were gold coated for SIMS analyses and then inserted into a stainless steel sample holder. Ti concentrations in quartz were collected with a Cameca 6F ion microprobe at the School of Earth and Space Exploration at Arizona State University. Analyses were obtained as described by Behr et al. (2011) with the 1st field aperture set to 1800 microns and the 2nd contrast aperture set to 150

microns. Masses ^{48}Ti, ^{49}Ti, ^{30}Si, ^{40}Ca, and ^{27}Al were collected using an energy window of 250 eV and a mass resolving power of 2800. ^{49}Ti/^{30}Si ratios were consistent with the measured ^{48}Ti/^{30}Si ratios and relative abundance of ^{48}Ti and ^{49}Ti. ^{40}Ca and ^{27}Al were collected to monitor for contamination and microinclusions. Mass cycles that were contaminated with excess ^{40}Ca and ^{27}Al were removed during data processing.

One spot analysis of the Herkimer "diamond" and three to seven spot analyses of the natural quartz standard were obtained per mount. The Herkimer diamond was analyzed to monitor surface contamination and to determine analytical background levels. In most cases, upon analysis, the Ti/Si ratio of the Herkimer quartz drifted steadily downward throughout analysis, which suggested surface contamination. To eliminate surface contamination, we first rastered an area of 50x50 microns, at 17-20 nA, and then reanalyzed it, in its center, with a focused, 25x25 micron spot at 4-8 nA. Peak count times were 15 minutes during the initial raster and 20 minutes per spot analysis. We followed this procedure for all spot analyses.

Three to four spots on single or adjacent grains were analyzed per sample. Spots were chosen based on CL character, grain size, and textural and chemical complexities. The average ^{48}Ti/^{30}Si ratios in each natural quartz standard were calculated and used to normalize a known concentration (Mt 1 = .0017; Mt 2 = .0021; Mt 3 = .0016; Mt 4 = .0013; Mt 5 = .0013; Mt 6 = .0015; Mt 7 = .0016; Mt 8 = .0014; and Mt 9 = .011 ^{48}Ti/^{30}Si at 39 ppm; Kohn and Northrup, 2009) of Ti in the natural quartz. The resulting conversion factors (39 ppm/.0017 = 22900; 39 ppm/.0021 = 18500; 39 pm/.0016 = 24400; 39 ppm/.0013 = 29100; 39 ppm/ .00103 = 29300; 39 ppm/ .0015 = 26900; 39 ppm/.0016 = 24223; 39 ppm/.0014 = 27800; and 39 ppm/.0011 = 35400 ppm,

respectively) were then multiplied by the $^{48}Ti/^{30}Si$ concentrations measured in the sample to obtain Ti concentrations (Figure 1.7).

1.3.2 Electron Microprobe Chemical and Thermobarometric Analysis

Two samples, SC10-18 and SC10-30, were selected for thermobarometric analyses using standard petrographic criteria (e.g., Kohn, 2008). These samples contained mineral compositions that were appropriate for determining peak temperature and pressure estimates via thermodynamic equilibria.

Dr. Stacey Corrie acquired garnet X-ray maps and elemental compositions (Figures 1.8 and 1.9) using a Cameca SX100 electron microprobe housed in the Department of Earth and Environmental Sciences at Rensselaer Polytechnic Institute, Troy, New York. Analyses were obtained as described by Corrie (2010): X-ray compositional maps of the elements, Fe, Mg, Mn, Ca, and Al, were collected on garnet via stage-mapping. Operating conditions for the X-ray maps consisted of an accelerating voltage of 15 kV, a current of 200 nA, a pixel time of 30 msec, and a step size of 2-5 microns/pixel. These maps allowed us to target the location of the line scans. Natural and synthetic silicates and oxides were used for calibrations, and quantitative measurements were made using an accelerating voltage of 15 kV and a current of 20 nA. A minimum beam size was used on garnet at 10 µm intervals along the line. A 10 µm beam size was used on plagioclase and micas. Peak count times were 10 s (Na, Ca, Fe, Mn, Si, Al), and 20 s (Mg, Ti, K).

Peak temperatures and pressures were calculated via exchange reactions and thermodynamic equilibria using Ferry and Spear's (1978) garnet-biotite thermometer, Bermans's (1990) garnet solution model, and Hoisch's (1990) garnet-plagioclase-

muscovite-biotite barometer (Figures 1.10 and 1.11). The lowest Mn and Fe/(Fe+Mg) values, associated with a trough in garnet compositions from core to rim, were selected for temperature and pressure estimates. These near rim garnet compositions were least affected by garnet dissolution and retrograde reactions and most accurately approximate peak metamorphic conditions. These garnet compositions were combined with compositions of plagioclase, biotite, and muscovite near the garnet that appeared to be texturally equilibrated rather than retrograde products. Peak metamorphic temperatures were also estimated at the highest grades using petrogenetic grids (Spear and Cheney, 1989).

We estimated depths of the MBT by assuming that the MBT was dipping 10˚ to the NW during the main Caledonian orogeny, similar to the current dip magnitude of the main Himalayan thrust (MHT) in the Himalaya (Henry et al., 1996), which was measured at the surface exposure of the MHT. We then calculated pressures at each depth, knowing from thermobarometry that the pressure at the NW extent of our collections was 8 kbar (see section 1.4), and assuming a pressure of ~ 3 kbar (i.e., 10 km for the brittle-ductile transition) near the thrust front. We explored the effects of changing the assumed dip magnitude of the MBT from 5˚ to 12˚ NW, and found that calculated TitaniQ temperatures were not sensitive to changes in the dip angle. The MBT could not have dipped more steeply than 12˚ on average: relative to the western end of the transect, it would project to the surface west of the eastern end of the transect, well west of the present eroded thrust front.

We calculated temperatures using the Ti-in-Qtz thermobarometer ($RT\ln X_{qtz,TiOx} = -60952 + 1.520*T(K)-1741*P(kbar)+RT\ln_{aTiO2;}$ Thomas et al., 2010). Temperatures

associated with large analytical errors ($2\sigma \geq 50°C$) were discarded and temperatures that were statistically equivalent in a sample were averaged.

1.4 Results

Both samples analyzed for garnet-biotite Fe-Mg exchange thermometry (SC10-18 and -26) show similar or lower TitaniQ temperatures (Figure 1.12): $SC10\text{-}18_{Grt\text{-}Bt} = 525 \pm 20°C$ and $SC10\text{-}18_{TitaniQ} = 420 \pm 8$, and $325 \pm 8°C$; $SC10\text{-}26_{Grt\text{-}Bt} = 525 \pm 35$, and $SC10\text{-}26_{TitaniQ} = 494 \pm 18°C$. The occurrence of the assemblage Grt+Ky+Bt+Ms at the highest metamorphic grades (farther west) imply minimum temperatures of ~575°C (Spear and Cheney, 1989).

In all instances, cross-cutting quartz vein temperatures mimic TitaniQ temperatures of the host rocks, and the host rock groups (Figure 1.13): Quartz vein SC10-25, of group B, = 419 ± 11°C, and group B = ~380-452°C; quartz veins SC10-04 and -06, of group C, = 454 ± 8, and 418 ± 20°C, respectively, and group C = ~400-475°C; quartz vein SC10-34, of group F, = 371 ± 15°C, and group F = ~330-370°C; and quartz vein SC10-46, of group G = 344 ± 16°C, and group G = 345 ± 16°C. Directly comparing cross-cutting quartz veins to their host rocks, shows quartz vein SC10-04 = 454 ± 8°C, and host rock SC10-03 = 435 ± 16°C; and quartz vein SC10-34 = 371 ± 15°C, and host rock SC10-33 = 361 ± 11°C.

Metamorphic mineral assemblages that contain garnet + kyanite + biotite + staurolite in the structural basement of the Caledonides indicate that amphibolite facies conditions were attained (Northrup, 1996b). Ultramylonites with local psuedotachylite found near the thrust front indicate that conditions approached the brittle-ductile transition. TitaniQ temperatures range from <300°C at the thrust front to >400°C at the

deepest crustal levels. Higher TitaniQ temperatures are also preserved in some grains and more closely reflect peak metamorphic conditions inferred from metamorphic phase equilibria (see upper bound in Figure 1.14).

Lastly, TitaniQ temperatures are broadly consistent with temperatures expected from quartz microstructures (Figure 1.14). However, TitaniQ temperatures reveal grain boundary migration recrystallization (GBM) occurring at temperatures as low as 340°C, which is significantly lower than previously published temperatures for GBM (500-700°C; Hirth and Tullis, 1992; Stipp et al., 2002). We also observe quartz recrystallizing primarily by BLG at temperatures of ~450°C, which is higher than previously published temperatures for BLG (400°C; Hirth and Tullis, 1992; Stipp et al., 2002).

1.5 Discussion

Because mylonites texturally postdate the peak of metamorphism, quartz grains that recrystallized during mylonitization should record lower temperatures than either the metamorphic peak or igneous cooling. We take the lowest temperature recorded by recrystallized quartz as the temperature of final shearing, a cluster of temperatures near this minimum as the range of temperatures over which the shear zone moved (at a specific location) and anomalously high temperatures as possibly relict protolith or peak metamorphic grains or domains whose Ti content was incompletely erased by later deformation (Figure 1.14).

Minimum temperatures were regressed vs. distance using a linear least squares model to estimate the final temperatures of thrust movement and the average temperature gradient along the thrust during final movement. Minimum TitaniQ temperatures, estimated to range from 210 ± 48°C at the thrust front to 475 ± 25 °C at the deepest

crustal levels, reflect the best estimate of the final temperatures of deformation (Figure 1.14).

We conclude that Ti contents in quartz must be reset during deformation, since most TitaniQ deformation temperatures fall well below the metamorphic peak, and because TitaniQ temperatures in host rocks mimic TitaniQ temperatures in cross-cutting quartz veins (we assume that retrograde deformation post-dated peak metamorphism). If deformation pre-dated peak metamorphism, then the deformation textures in quartz would not be preserved, as they are in our samples. The higher temperatures that are preserved in each location more closely reflect expectations from metamorphic phase equilibria (see Upper Bound in Figure 1.14). Finally, TitaniQ temperatures are mostly consistent with temperatures expected from quartz microstructures, but on average, TitaniQ temperatures are lower (Figure 1.14).

In Figure 1.14, minimum temperatures for groups A through K plot on the line $y = 1.69x + 210$. This line is projected to intersect the secondary axis (thrust front) at 210 ± 48˚C, which is the presumed temperature of deformation currently exposed at the thrust front and brittle-ductile transition. Some samples cluster and record a small range of temperatures, which we interpret as the range of temperatures over which the shear zone moved (at a specific location), whereas others record a large range of temperatures.

We interpret the upper bound on these temperatures as the minimum temperature of peak metamorphism, due to loss of Ti during recrystallization, and the lower bound as the temperature at which quartz was equilibrating during the final stages of deformation. Resetting of Ti contents in quartz does not appear effective at temperatures below 275˚C, since SC10-55, of group K, does not plot on the lower bound. Similarly, SR does not

seem to be as effective as GBM at completely resetting Ti contents in quartz crystals during dynamic recrystallization, since samples SC10-51 (Figure 1.15) and -49, of groups I and J, respectively, which recrystallized by SR, record anomalously high temperatures. Sample SC10-45, of group E, plots on the upper bound, rather than the lower bound, perhaps because it too recrystallized by SR. CL images of Sample SC10-45 reveal very bright cores and dark rims, even on a subgrain scale, which suggests a very high concentration of Ti in the cores (i.e., relict compositions; Figure 1.16).

Anomalous temperatures in samples were interpreted based on microstructural controls and CL variability. Anomalously high temperatures in the cores of grains were interpreted as temperatures of a cooling pluton that were not completely reset, or as metamorphic temperatures. Anomalously high temperatures near rims or on grain boundaries might have resulted from minor rutile in the grain boundaries. Anomalously low temperatures, on the other hand, were interpreted as temperatures associated with late-stage, retrograde deformation. This interpretation is supported by overprinted deformation textures (undulose extinction, subgrains, and bulges) and cross-cutting chlorite. The deformation textures observed in each sample are associated with the last temperatures of deformation, which correspond to the lowest temperatures at which the quartz equilibrated.

The estimated temperature for the thrust front is 210 ± 48˚C, even though a TitaniQ temperature of 333 ± 22˚C is recorded for sample SC10-55 of group K. We hypothesize that SC10-55 may not plot on the line for several reasons: 1) Equilibration was incomplete due to ineffective SR at lower temperatures; 2) Sample SC10-55 is either an ultramylonite or alternatively a quartzite, in which case, the temperatures recorded in

this sample are taken out of context; and 3) The beam likely sputtered through grain boundaries since the average grain size in sample SC10-55 is <10 microns. Similarly, sample SC10-51, in group J, may simply be a quartzite (Figure 1.15), so the temperatures recorded in this sample are also suspect. The lowest temperature recorded in sample SC10-51 projects on the lower bound, but the other temperatures might be anomalously high for the reasons stated above. An anomalously high temperature was also recorded in sample SC10-49 of Group I. This sample is an ultramylonite with an unknown protolith. Therefore, in addition to the reasons stated above, this anomalously high temperature might be the temperature of a cooling pluton that was incompletely reset. This is most likely why sample SC10-03 of group F records an anomalously high temperature.

Hirth and Tullis (1992) identified different dislocation regimes in experimentally deformed quartz aggregates, operative over different temperature ranges. Stipp et al. (2002) similarly identified three regimes in naturally deformed quartz veins in the Eastern Tonale strike-slip shear zone, Italian Alps, which were characterized by these different dynamic recrystallization mechanisms. The microstructures and temperatures associated with the different dynamic recrystallization mechanisms in this 'natural laboratory', for a presumed strain rate, correlate with the dislocation creep regimes defined by Hirth and Tullis (1992): BLG dominates from 280 to 400°C, SR dominates from 400 to 500°C, and both SR and GBM dominate from 500 to 700°C. Grujic et al. (2011) also applied TitaniQ to mylonites from the Eastern Tonale fault zone and his findings agree well with the previous studies. Thus, their results contrast markedly from ours, where BLG, as the dominant recrystallization mechanism, is not observed at any temperature, SR is observed at temperatures well below 400°C, and GBM is observed at temperatures as low

as 350°C. Strain rate and temperature both contribute to the textures observed in quartz, and therefore it is inadvisable to determine temperatures of mylonites based solely on quartz microstructures. In the Caledonides, a much lower strain rate may stabilize SR and GBM at lower temperatures than anticipated elsewhere.

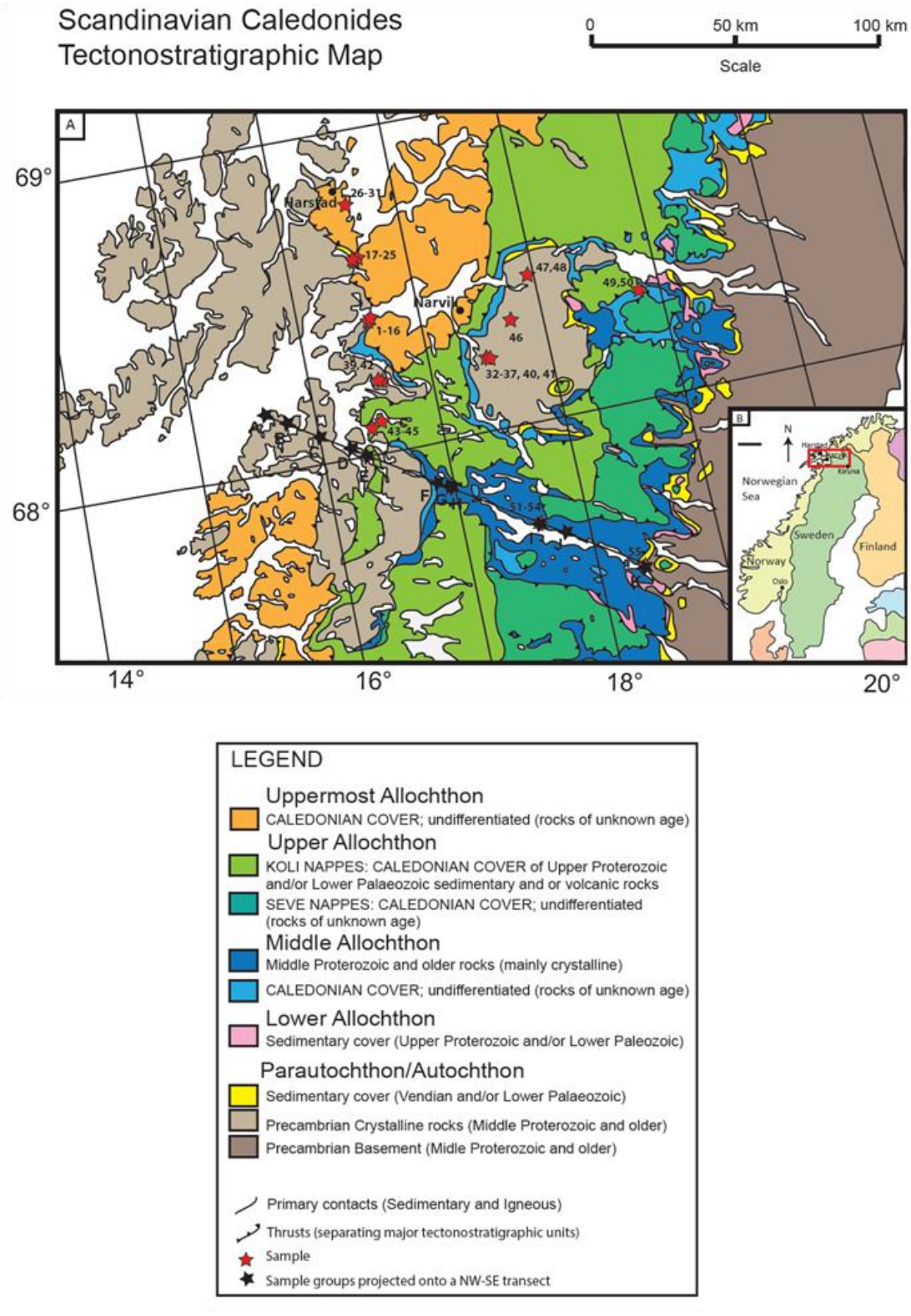

Figure 1.1: A) Tectonostratigraphic map of the northern Scandinavian Caledonides adapted from Gee (1975) with sample collection locations and sample collection groups. B) Map of Scandinavia showing field area in red rectangle.

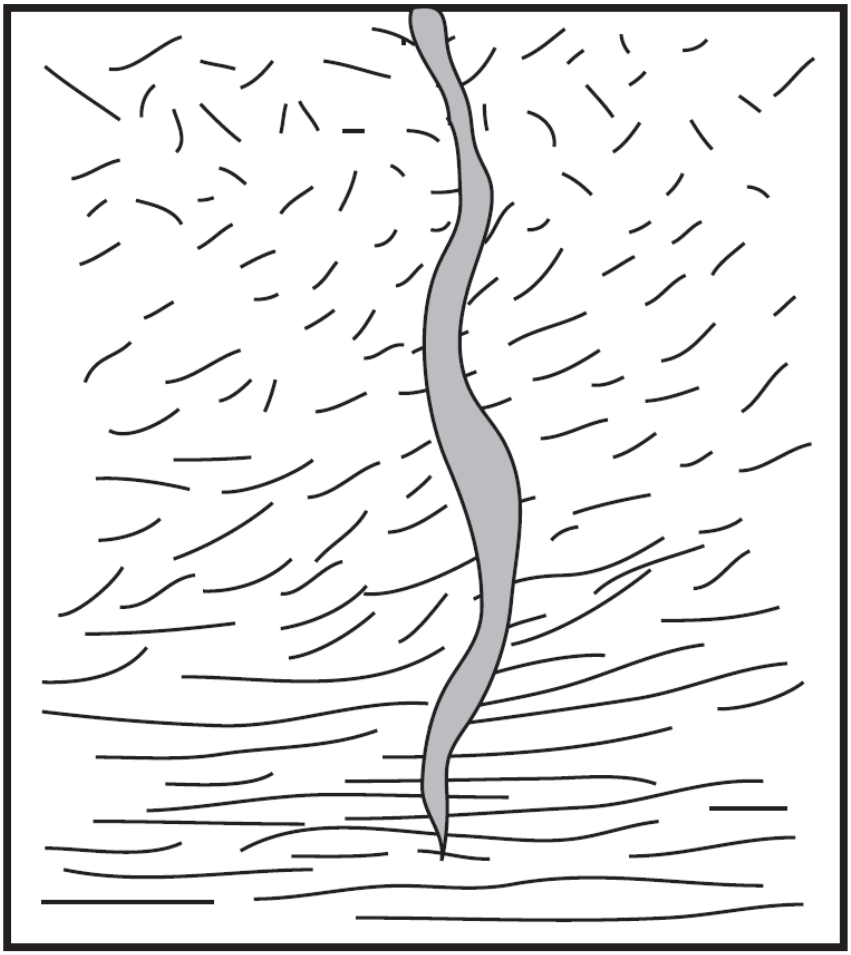

Figure 1.2: Example of a rock that shows the progression from undeformed granite to mylonitized granite (the foliation defines the degree of deformation). Neoblastic quartz vein (grey) cross-cuts the host rock, and provides a constraint on the minimum temperature of deformation. TitaniQ temperatures of quartz veins provide an independent check on accuracy of TitaniQ temperatures of host rocks.

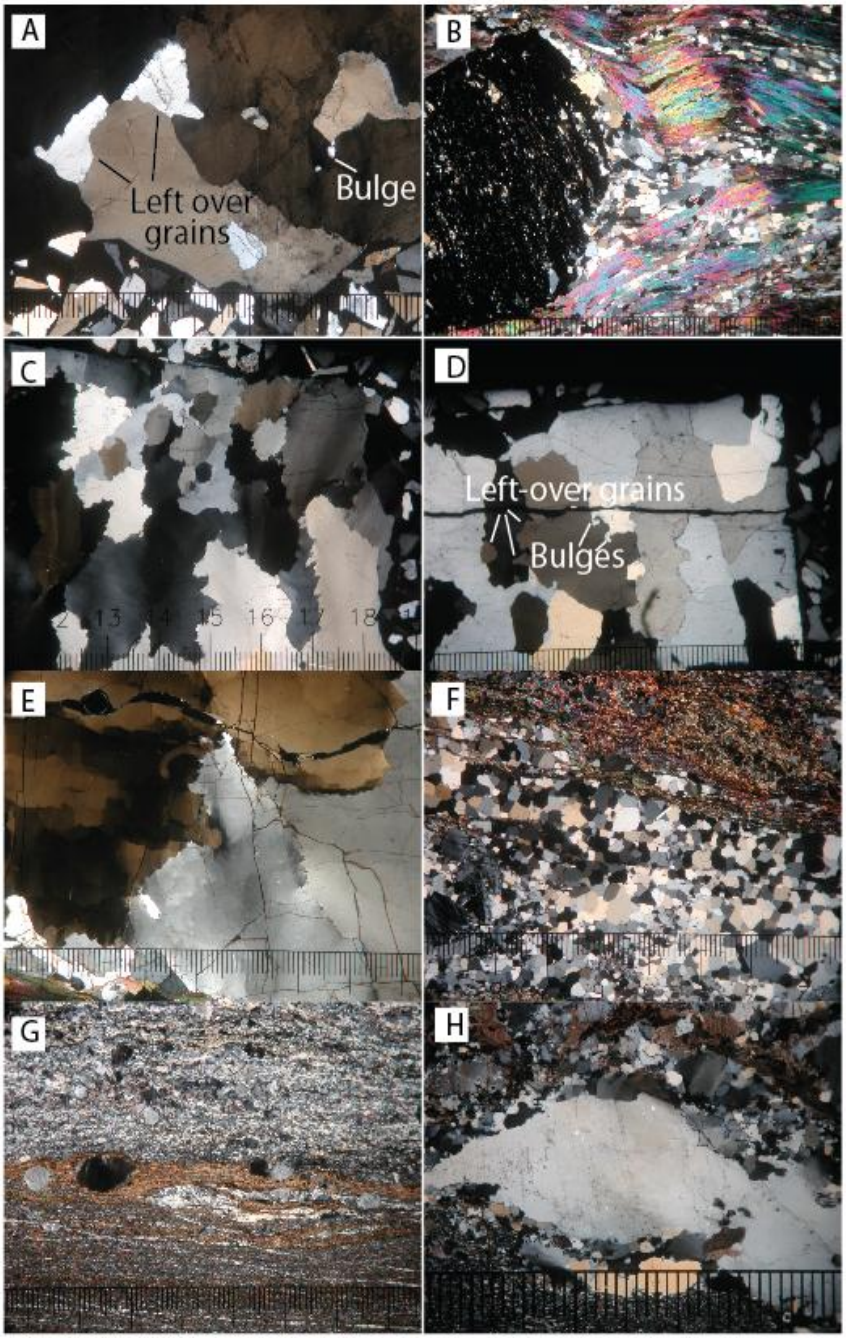

Figure 1.3: Images showing different deformation textures in samples. A) Left-over grains displayed in sample SC10-04; B) pressure shadow and inclusions indicate that the garnet grew pre-deformation; C) grain boundaries are highly irregular due to bulging in sample SC10-29; D) bulges and left-over grains present in sample SC10-34 indicate GBM; E) patchy extinction distinguishes subgrains in sample SC10-45; F) uniform extinction and uniform grain size and straight grain boundaries indicate that grains recrystallized by grain boundary migration; G) ultra mylonite containing K-spar porphyroclasts; H) Classic core and mantle structure indicating recrystallization by SR. Each small interval on ruler is 100 microns.

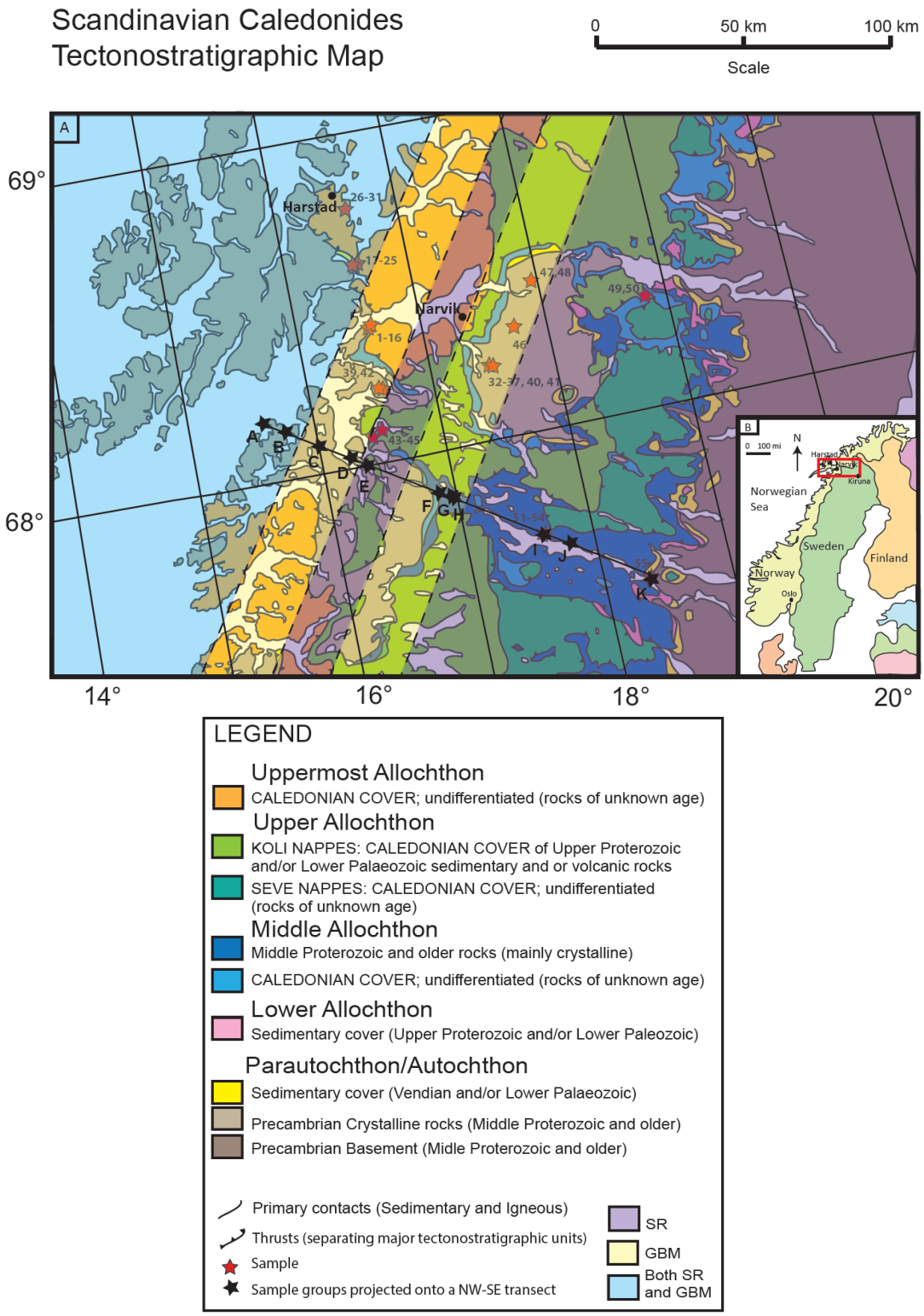

Figure 1.4: A) Tectonostratigraphic map of the northern Scandinavian Caledonides adapted from Gee and Sturt (1985) with sample collection locations, sample collection groups, and dynamic recrystallization mechanisms. B) Map of Scandinavia showing field area in red rectangle.

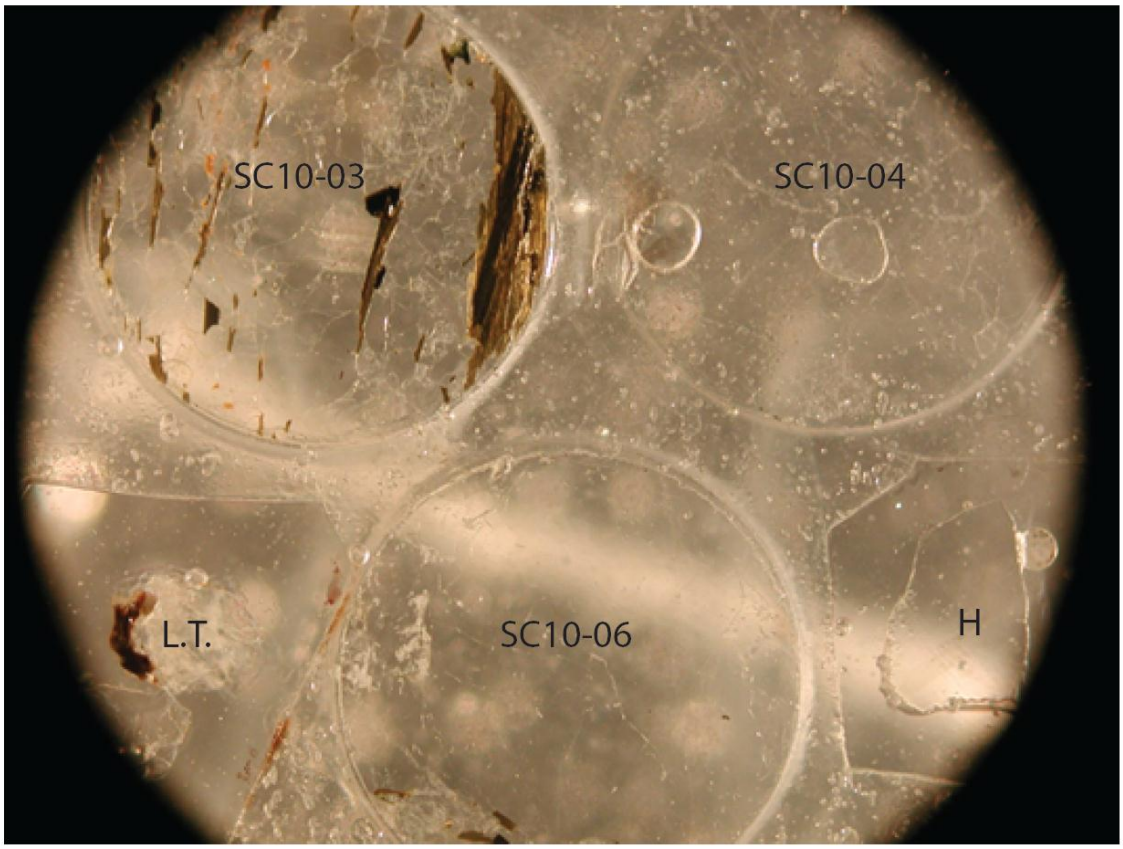

Figure 1.5: Example of a mount containing three samples, and two standards. Bottom left standard is the Lang tang natural quartz standard, and bottom right standard is the Herkimer quartz standard.

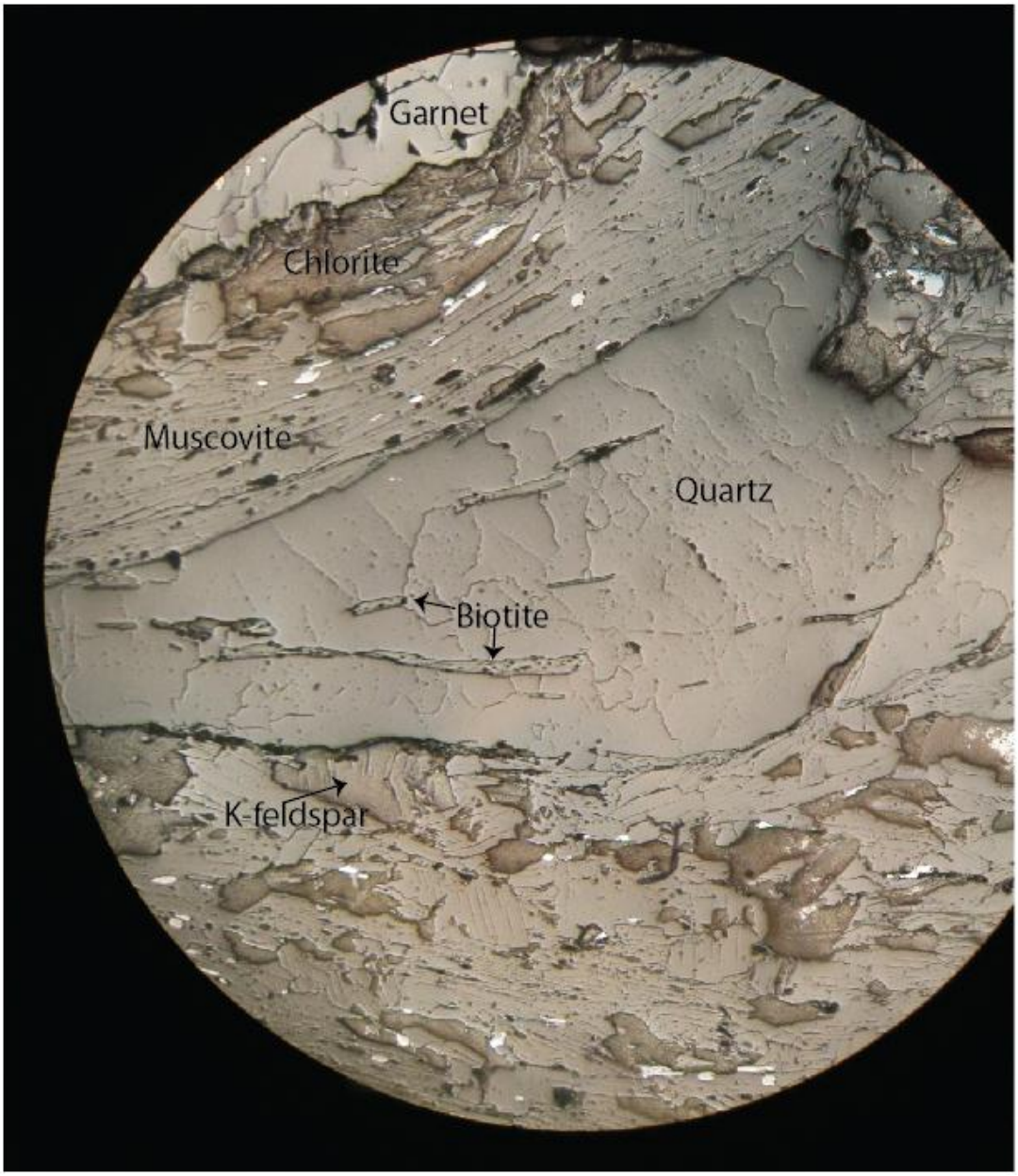

Figure 1.6: Example of a reflected light image of sample SC10-03.2

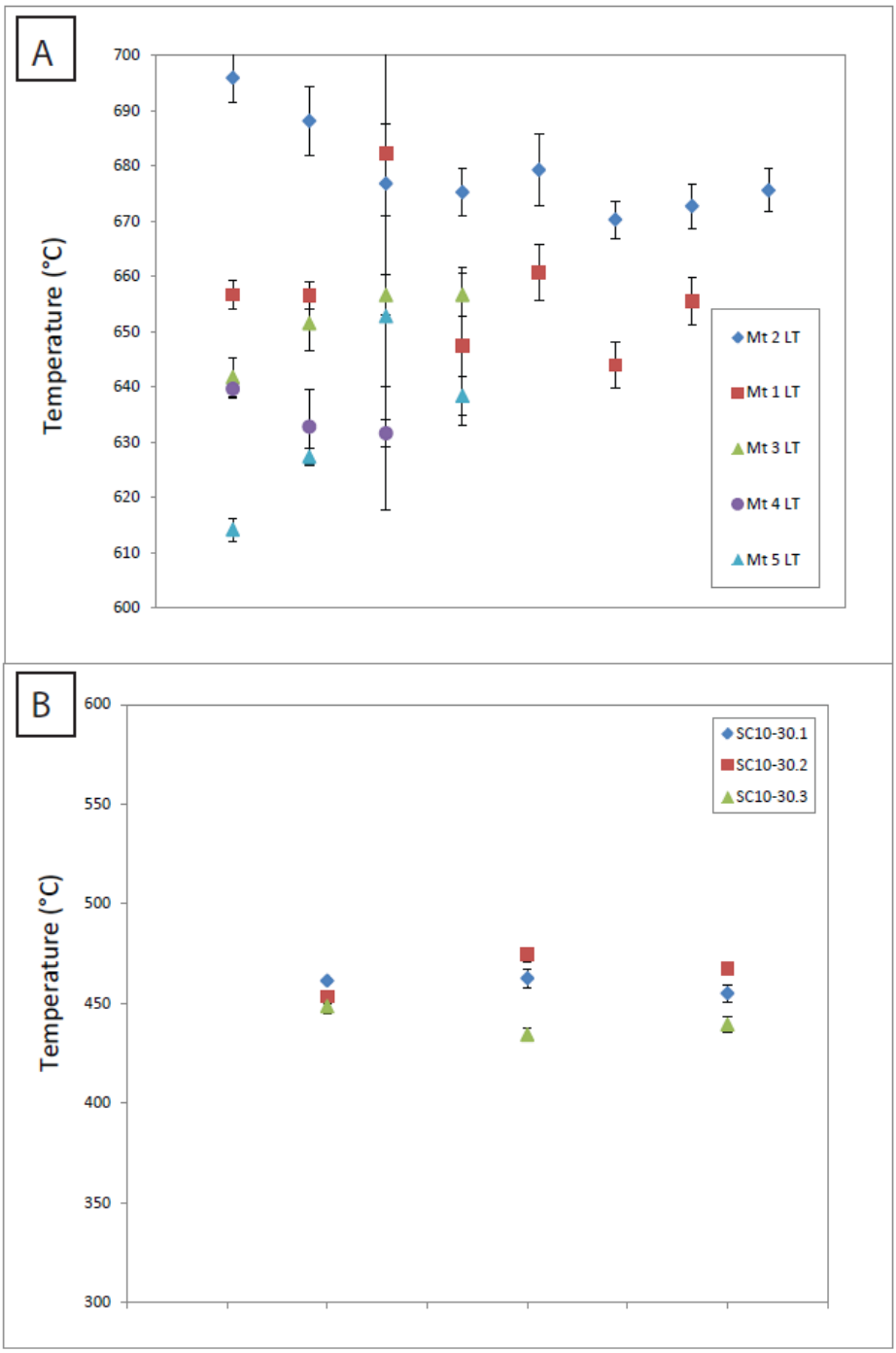

Figure 1.7: Two graphs that illustrate precision of TitaniQ using the SIMS. A) Ideally, the LT standard should give the same temperature each time it is analyzed. In fact, this is not true because the LT quartz is not perfectly homogenous and it is possible to get different ratios on the SIMS on different sample mounts due to the geometry of the polished disc in the stainless steel sample holder. B) Similarly all samples of SC10-30 should record the same temperature since they were deforming together.

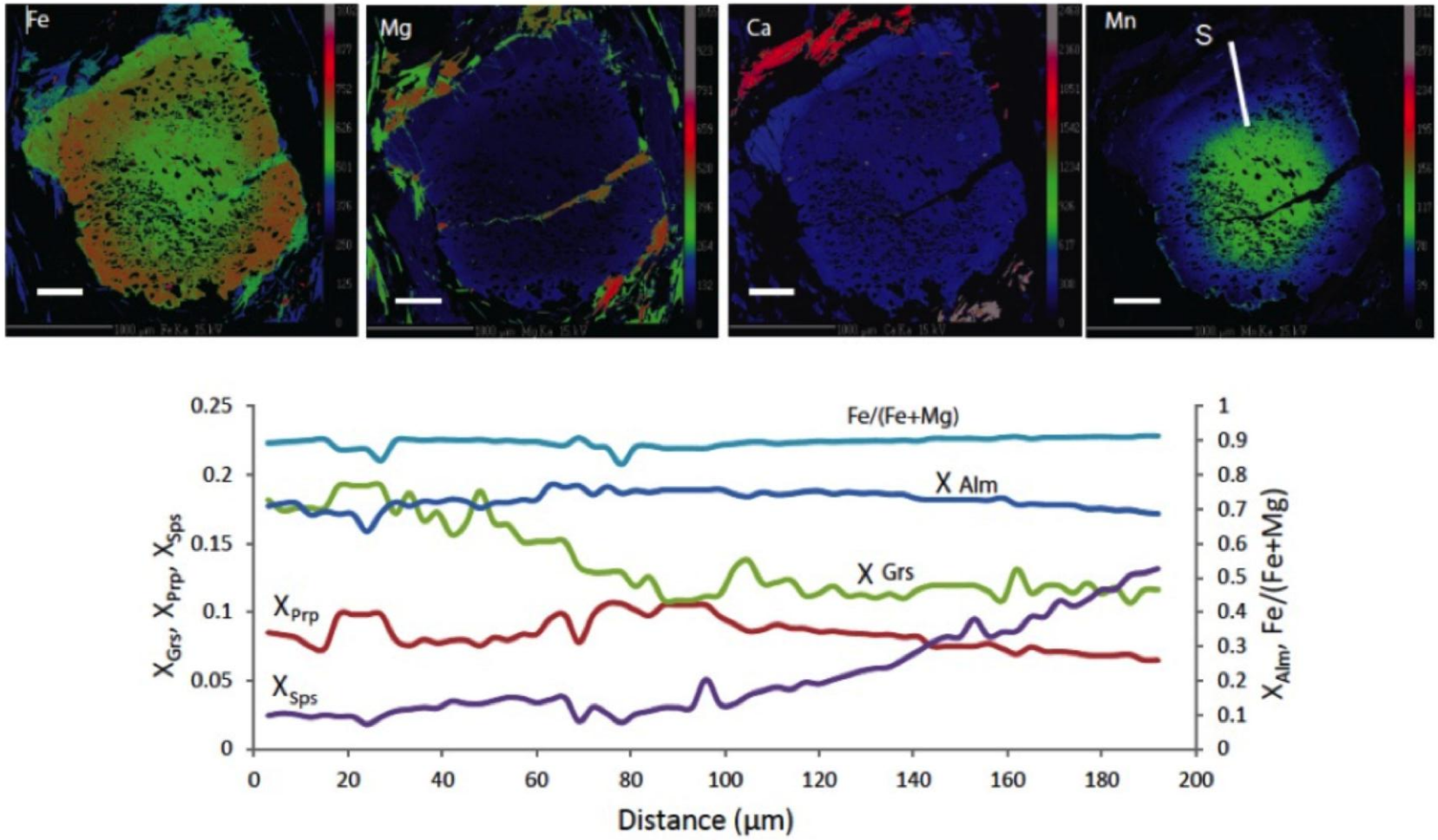

Figure 1.8: Scandinavian Caledonides SC10-18 garnet. White line is traverse across garnet from rim to core. Scale bars 100 microns.

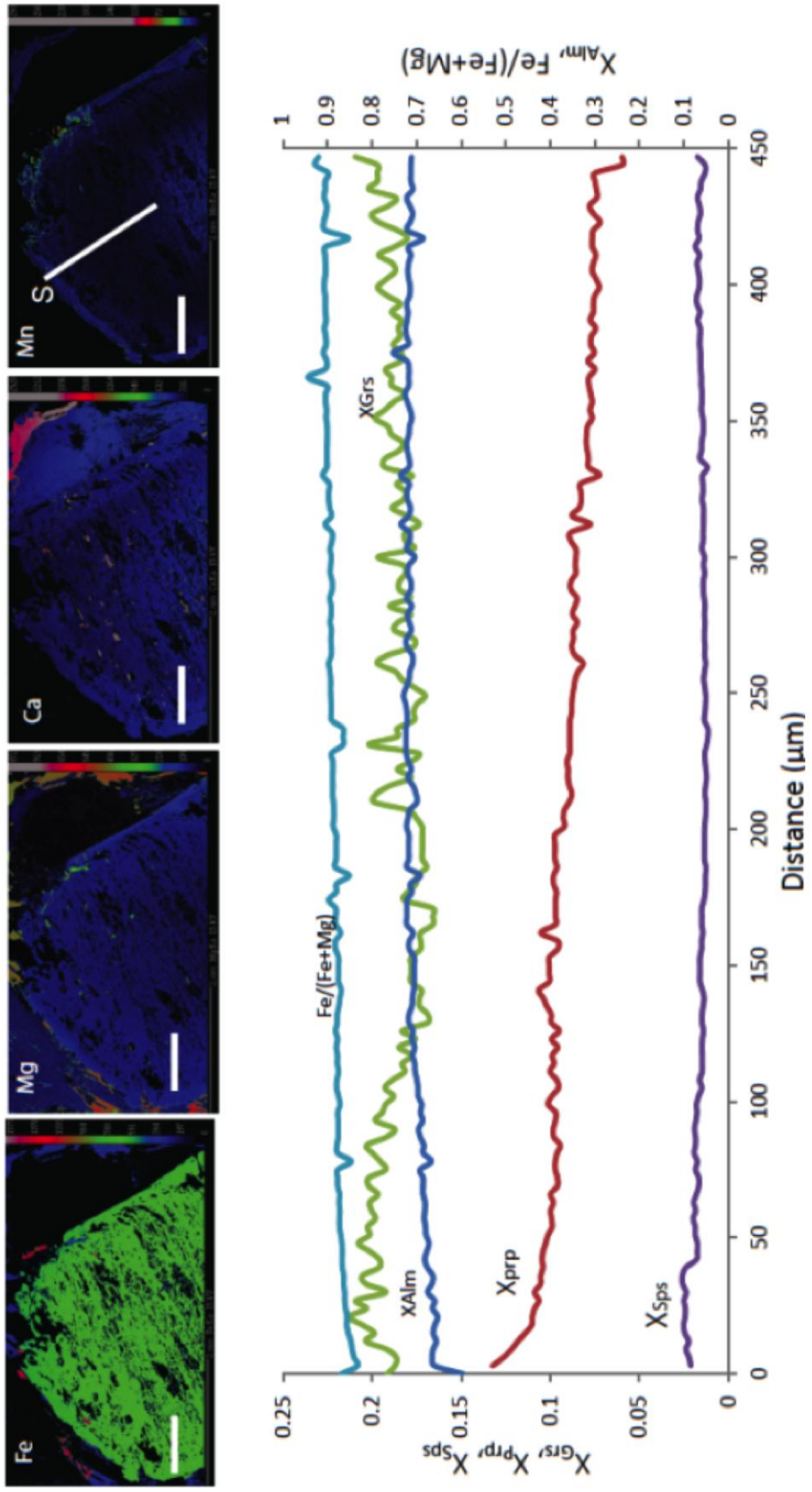

Figure 1.9: Scandinavian Caledonides SC10-26 garnet. White line is traverse across garnet from rim to core. Scale bars 200 microns.

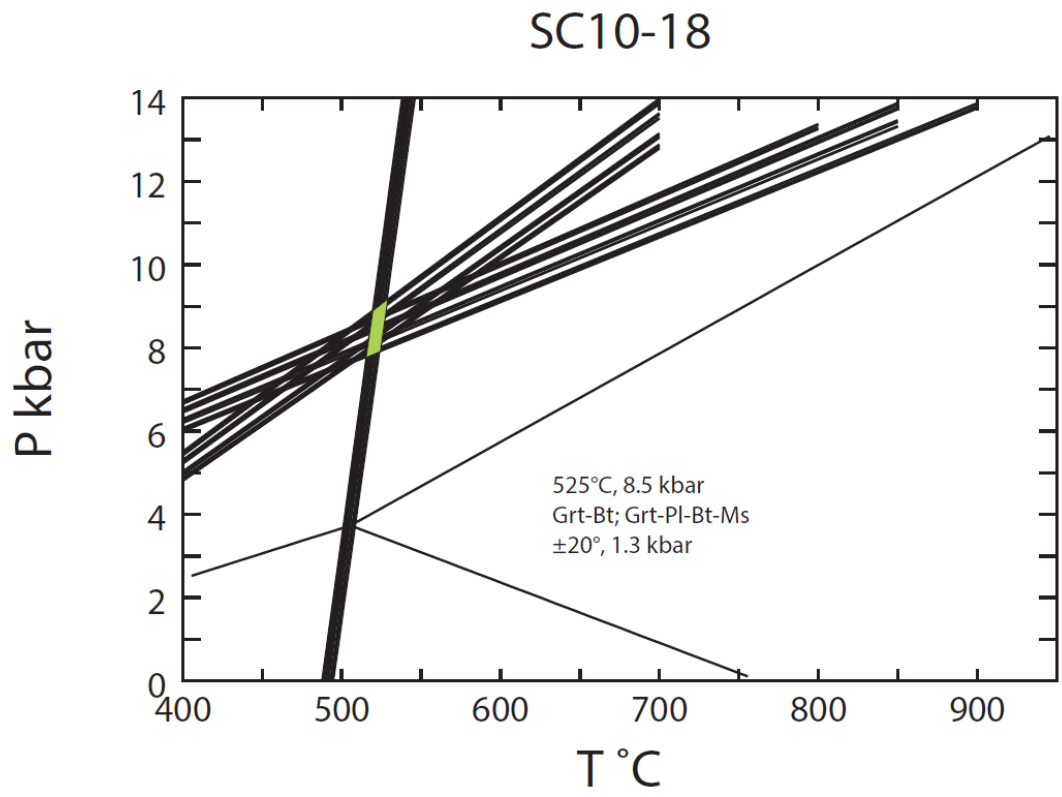

Figure 1.10: Pressure-temperature plots for sample SC10-18. Intersection of the garnet-biotite (Ferry and Spear, 1978) and the garnet-biotite-muscovite-plagioclase (Hoisch, 1990) equilibria indicates 525 ± 20°C and 8.5 ± 1.3 kbar.

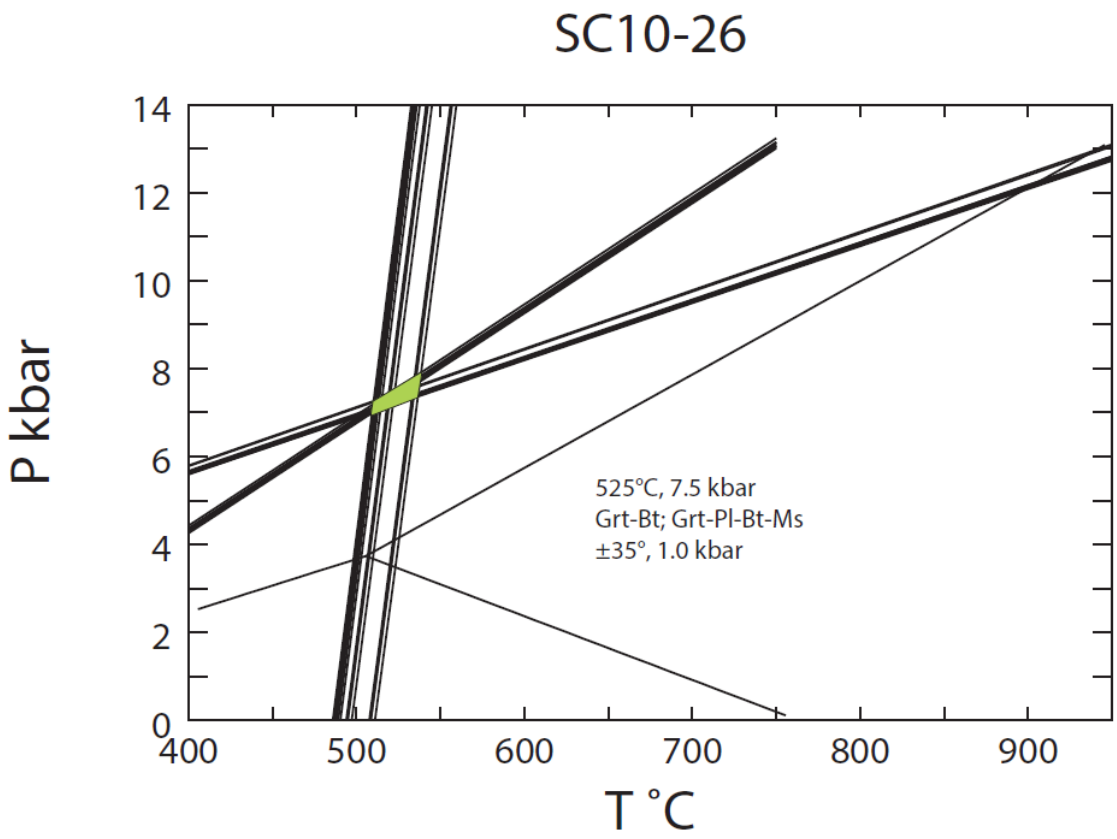

Figure 1.11: Pressure-temperature plots for sample SC10-26. Intersection of the garnet-biotite (Ferry and Spear, 1978) and the garnet-biotite-muscovite-plagioclase (Hoisch, 1990) equilibria indicates 525 ± 35°C and 7.5 ± 1.0 kbar.

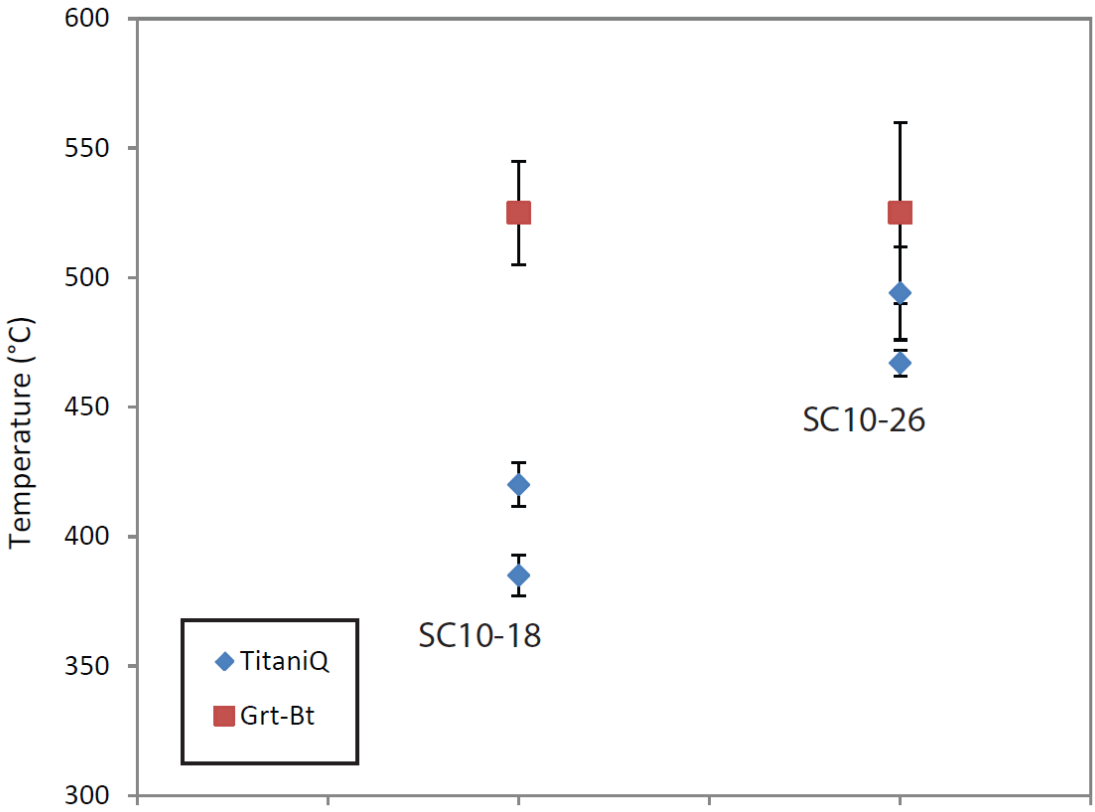

Figure 1.12: Temperatures obtained by garnet-biotite exchange equilibria and TitaniQ in sample SC10-26 were in agreement with each other. On the other hand, in sample SC10-18, the temperature obtained by garnet-biotite exchange equilibria was much higher than the temperatures obtained by TitaniQ.

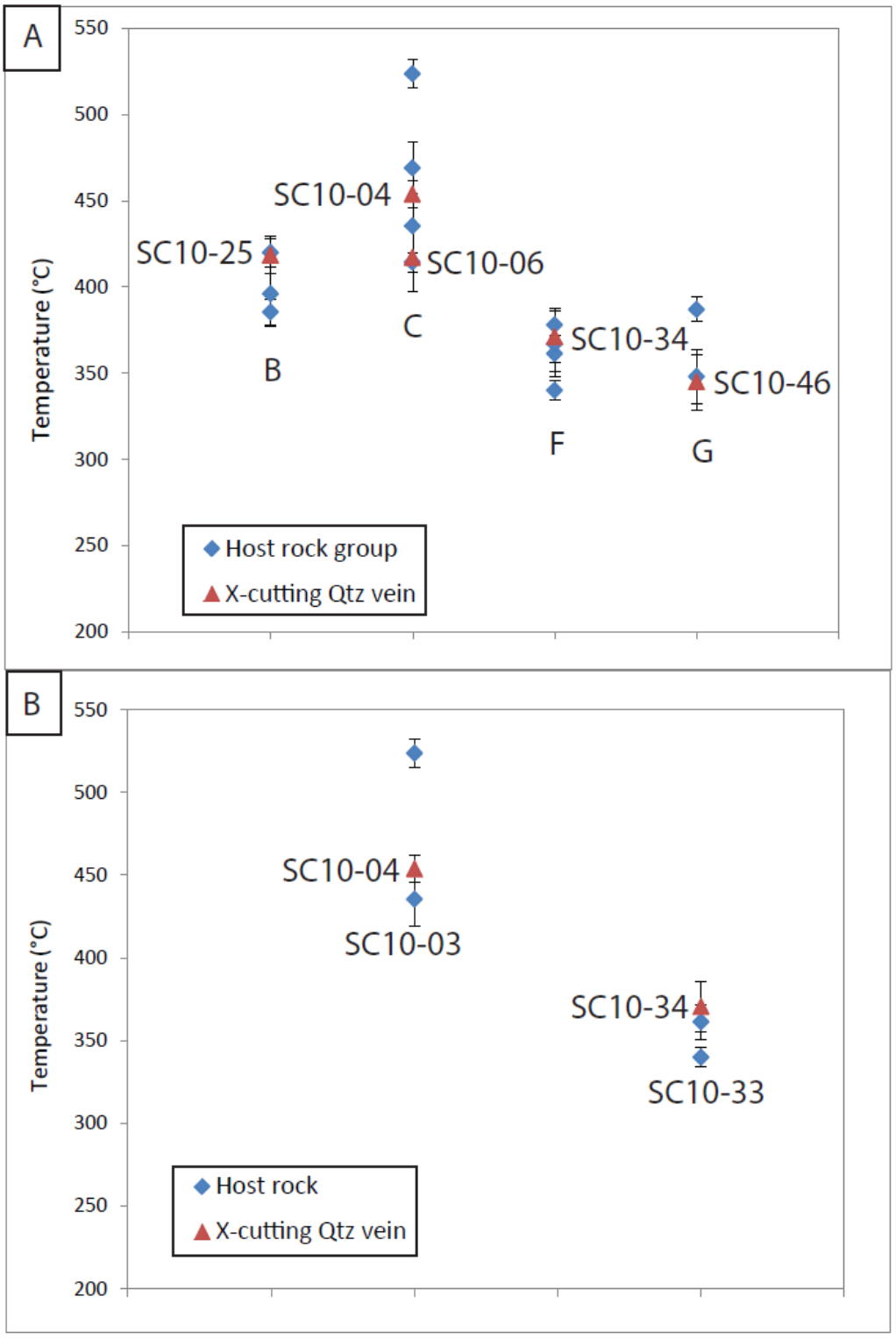

Figure 1.13: A) Cross-cutting quartz veins record the same temperatures as the rocks in the same sample locations (groups). B) Temperatures obtained from two cross-cutting quartz veins (SC10-04 and Sc10-34) mimic temperatures of their respective host rocks (SC10-33 and SC10-34, respectively).

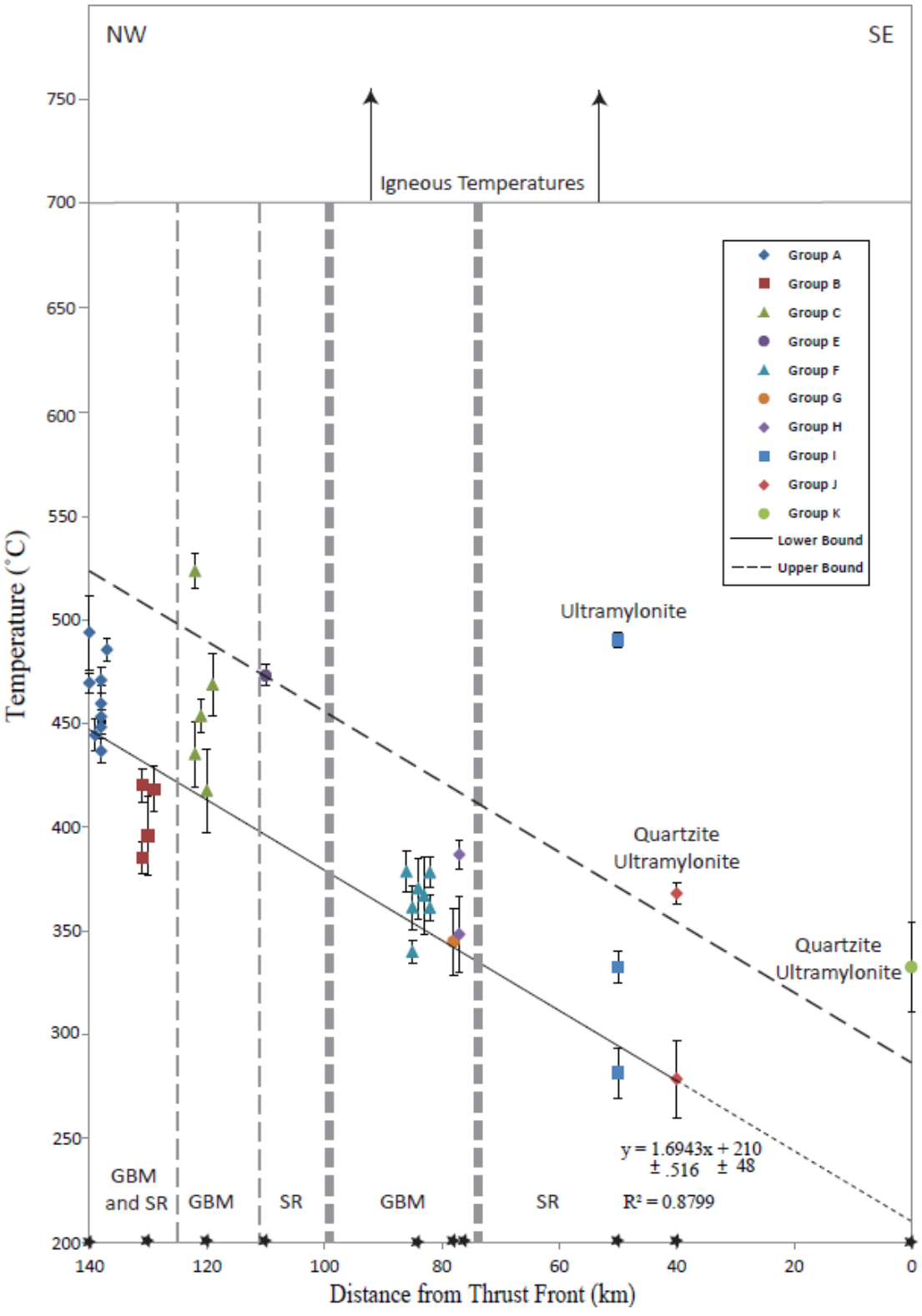
NW
SE
Igneous Temperatures
Group A
Group B
Group C
Group E
Group F
Group G
Group H
Group I
Group J
Group K
Lower Bound
Upper Bound
Ultramylonite
Quartzite Ultramylonite
Quartzite Ultramylonite
y = 1.6943x + 210
± .516 ± 48
R² = 0.8799
GBM and SR
GBM
SR
GBM
SR
Temperature (°C)
Distance from Thrust Front (km)
750
700
650
600
550
500
450
400
350
300
250
200
140
120
100
80
60
40
20
0

Figure 1.14: Groups A through K plot on the line y = 1.6943x + 210. This line is projected to intersect the secondary axis at ~ 210°C which is the presumed temperature of deformation at the thrust front. The lower bound is interpreted as the best representation of minimum temperatures of deformation. The lower bound was regressed through the lowest temperatures from each group. The upper bound is interpreted as the minimum temperature of peak metamorphism, due to loss of Ti during retrograde metamorphism. The upper bound was drawn parallel to the lower bound, passing through the point (140, 525), since we know, from garnet-biotite Fe-Mg thermometry, that sample SC10-26, of group A, equilibrated at 525°C. Re-equilibration does not seem to be effective at resetting Ti contents in quartz at temperatures below ~275°C, and SR does not seem to be as effective as GBM at completely resetting Ti contents in quartz crystals during dynamic recrystallization at lower temperatures. Black stars mark specific locations of each group along the shear zone. Thin, dashed vertical line indicates precise boundary location, and thick, dashed vertical lines indicate uncertainty in boundary location.

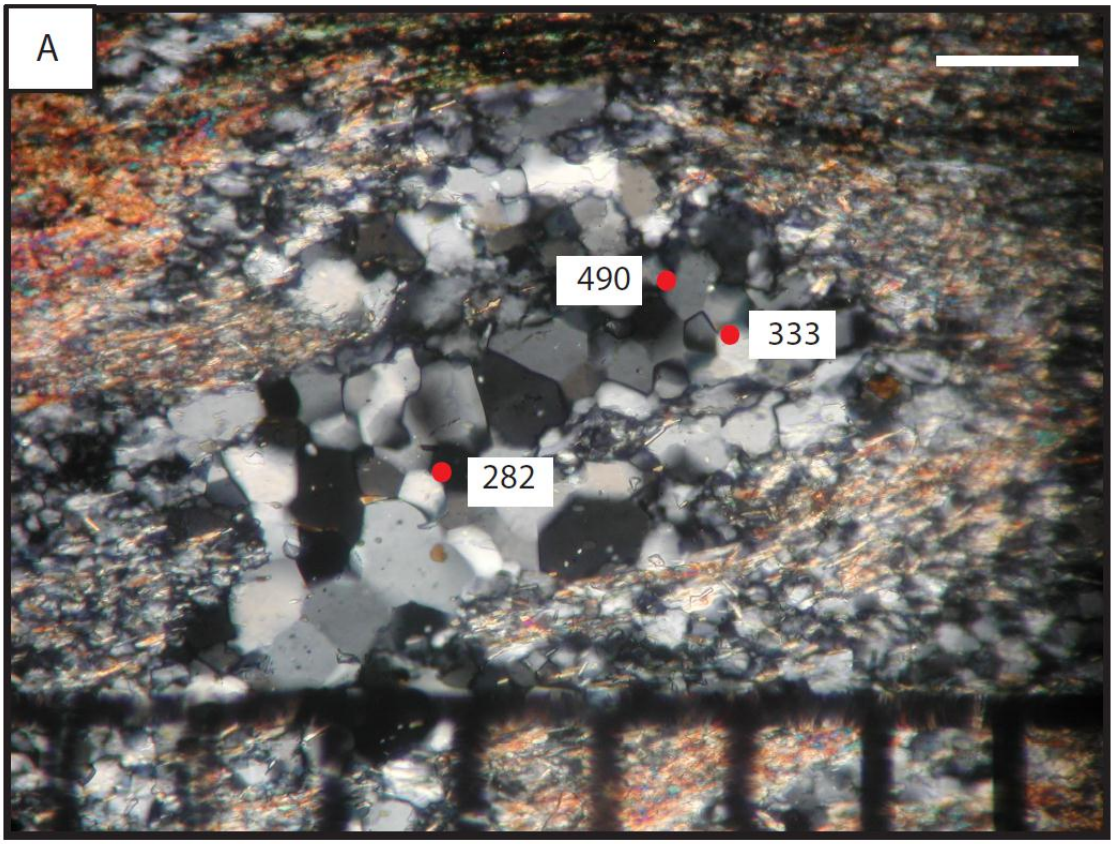

Figure 1.15: Photomicrograph of ultramylonite SC10-51. Temperatures are in degrees Celsius. Scale bar is 100 microns.

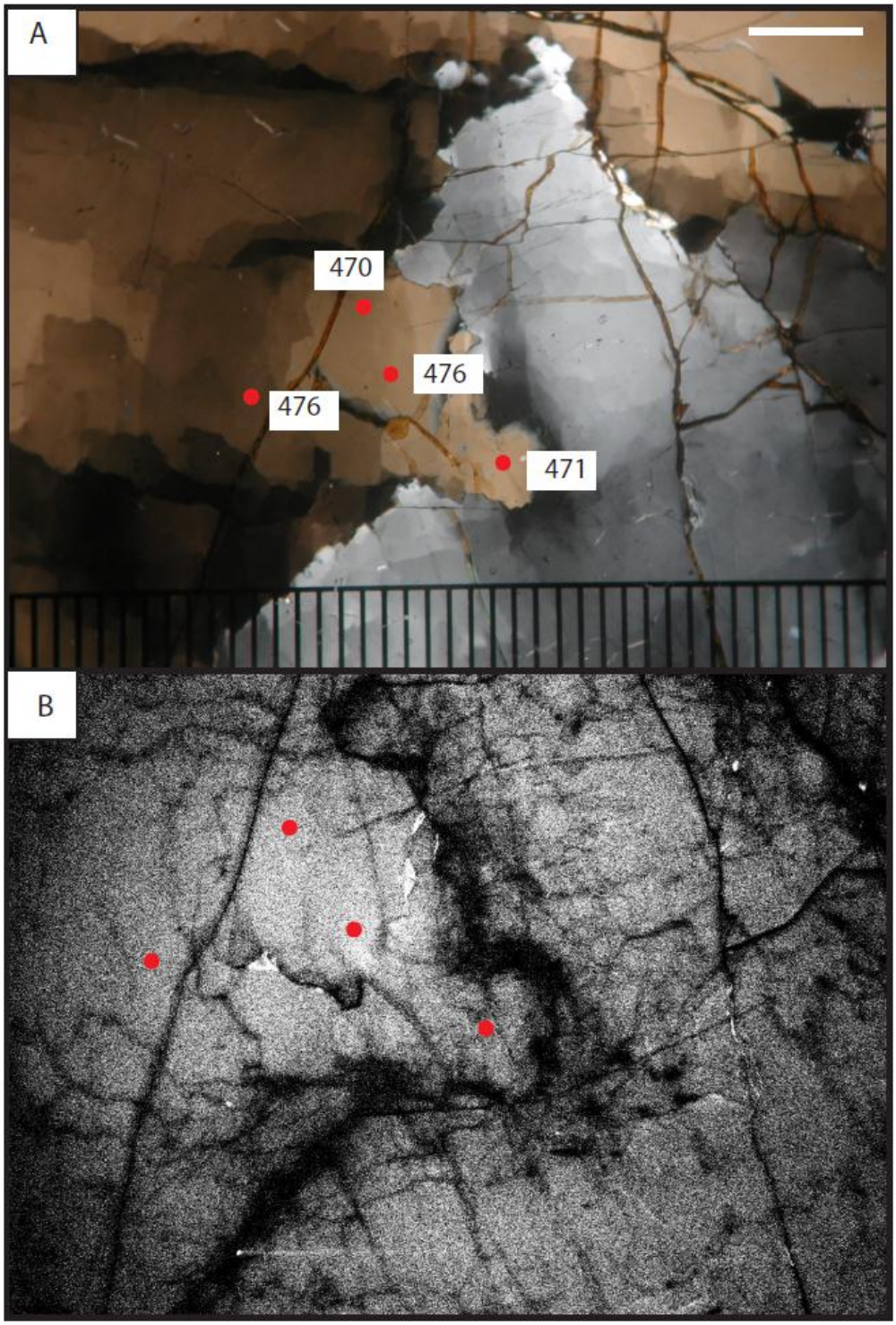

Figure 1.16: A) Photomicrograph and B) CL image of sample SC10-45. Temperatures are in degrees Celsius. Scale bar is 500 microns. The dominant dynamic recrystallization mechanism operative in quartz is SR. CL image reveals very bright cores and dark rims, even on a subgrain scale, which suggests a very high concentration of Ti in the cores.

Table 1.1: Mineral assemblages from rocks of the Scandinavian Caledonides in northern Norway and Sweden.

Sample	Group	Rock Type	Qtz	KSpr	Plag	Bt	Msc	Rut	Ti	Chl	Grt	Cal	Amp	Ep	Cpx	Dum	Opaq
SC10-26	A	schist	X		X	X	X	X		X	X						X
SC10-29	A	quartz vein	X														
SC10-30	A	schist	X			X	X	X		X	X						X
SC10-31	A	schist	X	X	X	X	X	X		X		X	X	X			
SC10-18	B	schist	X		X	X	X	X		X	X						X
SC10-21	B	quartzite	X	X		X		X		X							X
SC10-25	B	quartz vein	X			X	X	X									X
SC10-03	C	mylonite	X	X	X	X	X	X									
SC10-04	C	quartz vein	X														
SC10-06	C	quartz vein	X	X	X	X	X	X	X								
SC10-12	C	mylonite	X	X		X	X	X	X	X							X
SC10-42	D	Mylonite /quartzite	X		X	X		X	X					X	X		X
SC10-45	E	quartz vein	X					X									
SC10-32	F	mylonite	X	X		X	X	X					X	X			
SC10-33	F	mylonite	X	X		X		X					X				
SC10-34	F	quartz vein	X	X													
SC10-35bii	F	mylonite	X	X		X	X	X		X				X			X
SC10-38	F	schist	X			X		X		X				X	X		
SC10-46	G	quartz vein	X														
SC10-48	H	mylonite	X	X	X	X	X	X		X							
SC10-51	I	ultramylonite	X			X	X										
SC10-49	J	quartzite ultramylonite	X			X	X	X		X		X					
SC10-55	K	quartzite ultramylonite	X					X				X				X	

Table 1.2: Temperatures and geologic settings of rocks from the Scandinavian Caledonides in northern Norway and Sweden

Group	Sample	Rock Type	Geologic Setting	Depth of MBT (Km) if MBT is dipping 10° NW	Distance from thrust front (Km)	Pressure at MBT (Kbar)	Average TitaniQ Temps (°C)	± σ	Outliers (°C)	± σ
A	SC10-26	schist	Uppermost Allochthon: Calednoian Cover	34	140	8	494	18		
A	SC10-29	quartz vein	Uppermost Allochthon: Calednoian Cover	34	14	8	445	8		
A	SC10-30	schist	Uppermost Allochthon: Calednoian Cover	33	140	8	456	24		
A	SC10-31	schist	Uppermost Allochthon: Calednoian Cover	32	140	8	486	6		
B	SC10-18	schist	Caledonian Cover	32	130	8	420	8	385	8
B	SC10-21	quartzite	Caledonian Cover	32	130	7	396	19	429	7
B	SC10-25	quartz vein	Caledonian Cover	31	130	7	419	11		
C	SC10-03	mylonite	Parauatochthon/Autochthon: PreCambrian Crystalline rocks	30	120	7	435	16	524	8
C	SC10-04	quartz vein	Parauatochthon/Autochthon: PreCambrian Crystalline rocks	30	120	7	454	8		
C	SC10-06	quartz vein	Parauatochthon/Autochthon: PreCambrian Crystalline rocks	30	120	7	418	20		
C	SC10-12	mylonite	Parauatochthon/Autochthon: PreCambrian Crystalline rocks	28	120	7	469	15	414	6
D	SC10-42	mylonite/ quartzite	Parauatochthon/Autochthon: PreCambrian Crystalline rocks	24	110	6				

E	SC10-45	quartz vein	Upper Allochthon: Caledonian Cover	24	110	6	473	5		
F	SC10-32	mylonite	Parauatochthon/Autochthon: PreCambrian Crystalline rocks	24	85	6	379	10		
F	SC10-33	mylonite	Parauatochthon/Autochthon: PreCambrian Crystalline rocks	23	85	5	361	11	340	6
F	SC10-34	quartz vein	Parauatochthon/Autochthon: PreCambrian Crystalline rocks	23	85	5	371	15		
F	SC10-35bii	mylonite	Parauatochthon/Autochthon: PreCambrian Crystalline rocks	23	85	6	367	19		
F	SC10-38	schist	Parauatochthon/Autochthon: PreCambrian Crystalline rocks	22	85	6	378	8	361	7
G	SC10-46	quartz vein	Parauatochthon/Autochthon: PreCambrian Crystalline rocks	22	79	5	345	16		
H	SC10-48	mylonite	Parauatochthon/Autochthon: PreCambrian Crystalline rocks	18	78	4	348	16	387	7
I	SC10-51	ultramylonite	Middle Allochthon: Middle Proterozoic and older	18	50	4	282	12	333	8
									490	4
J	SC10-49	quartzite ultramylonite	Caledonian Cover	16	40	4	279	19	368	5
K	SC10-55	quartzite ultramylonite	Parautochthon/Autochthon	9	0	2	333	22		

Table 1.3: Thin section descriptions of rocks from the Scandinavian Caledonides in northern Norway and Sweden

Sample	Group	Rock Type	Thin Section Descriptions	Recrystallization Mechanism		
				GBM	SR	BLG
SC10-26	A	schist	Grain boundaries are straight and grains are approximately the same size (~200 µm). Extinction is uniform.	X		
SC10-29	A	quartz vein	The vein is composed of mostly large quartz crystals (~3mm) containting micro-cracks and fluid inclusion trails. The crystals have very irregular boundaries and there are many small bulges. Bulges and left-over microstructures are present. Some smaller crystals are ~500 µm. Patchy and sweeping undulose extinction.	X_D	X	
SC10-30	A	schist	Schistose texture and quartz ribbons. Some chlorite cross-cuts the fabric. There are a lot of quartz subgrains within larger grains. The larger grains are ~1mm and the subgrains and smaller grains are ~100 µm). Undulose Extinction		X	
SC10-31	A	schist	Spaced foliation defined by ribbons of mica. This sample displays a partially recrystallized fabric with a bimodal grain size distribution of quartz grains. Aggregates of small grains of approximately uniform size (100-300 µm) occur between large grains (5 mm). The larger grains contain subgrains of the same size as the small recrystallized grains. Undulose extinction	X_D	X	
SC10-18	B	schist	Spaced foliation that is defined by biotite ribbons. Grain boundaries are straight and grains are ~50-200 µm. Sweeping and Patchy undulose extinction.		X	
SC10-21	B	quartzite	Quartz crystals are ~ 100-150 µm. Pinning microstructures, window microstructures and dragging microstructures contribute to higly irregular quartz grain boundaries. Some bulges along grain boundaries and small quartz nucleations within larger crystals. Mostly uniform extinction.	X_D	X	
SC10-25	B	quartz vein	This sample displays spaced mylonitic foliation which is defined by ribbons of mica. This sample displays a partially recrystallized fabric with a bimodal grain size distribution of quartz grains. Aggregates of small grains of approximately uniform size (~50 µm) occur between large grains (~1 mm). Large grains contain subrains of the same size as the small grains. Undulose extinction.	X_D	X	

SC10-06	C	quartz vein	Mylonitic foliation. Quartz ribbons contain large quartz crystals (up to 10's of mm's). Pinning microstructures, window microstructures and dragging microstructures contribute to higly irregular quartz grain boundaries. Some bulges along grain boundaries and small quartz nucleations within larger crystals. Fluid inclusion trails are oriented normal to foliation. Mostly unifrom extinction but some patchy and sweeping undulose extinction.	X		
SC10-12	C	mylonite	Spaced mylonitic foliation that is defined by quartz ribbons and mica ribbons. Pinning microstructures, window microstructures, and dragging microstructures contribute to highly irregular quartz grain boundaries. Some bulges along grain boundaries and small quartz nucleations within larger quartz grains. Quartz crystals are 200-400 µm. Mostly uniform extinction but some patchy and sweeping undulose extinction.		X_D	X
SC10-42	D	mylonite/quartzite	Spaced foliation. Most of the grains have straight grain boundaries although draggin, pinning, and window microstructures are present. There are many small nucleations of quartz within larger grains. Quartz crystals are 100-300 µm. Mostly uniform extinction but few grains display patchy undulose extinction.	X_D	X	
SC10-45	E	quartz vein	Many subgrains present. Boundaries are highly irregular and there are many bulges. Rutile is almost completely concentrated in the grain boundaries or in the many microfractures. There are some fluid inclusion trails and left-over microstructures. The quartz crystals are 10's of mm's. Undulose extinction.	X_D	X	
SC10-32	F	mylonite	Mylonitic foliation which is defined by a shape preferred orientation, ribbons of mica and amphibole, and quartz ribbons which contain large quartz crystals (1-2 mm's). The boundaries are mostly straight but there are some irregularities as well as pinning microstructures, window microstructures, and dragging microstructures. Smaller quartz crystals are ~200 µm. Mostly unjiform extinction but some patchy and sweeping undulose extinction.	X_D	X	X_D
SC10-33	F	mylonite	Mylonitic foliation. Quartz ribbons contain large quartz crystals. Pinning microstructures, window microstructures and dragging microstructures contribute to higly irregular quartz grain boundaries. Some bulges along grain boundaries and small quartz nucleations (~100-200 µm within larger crystals (500 µm). Fluid inclusion trails are oriented normal to foliation. Mostly uniform buy some patchy and sweeping undulose extinction.	X_D	X	

SC10-34	F	quartz vein	The quartz grains have highly irregular grain boundaries. Many left-over grains and bulges, and nucleations of small quartz grains within the larger quartz grains (1 mm). ere are long trails of fluid inclusions and micro-fractures in the quartz grains. Mostly uniform but some patchy and sweeping undulose extinction.	X_D	X
SC10-35bii	F	mylonite	Spaced mylonitic foliation. Driagging microstructures, bulges, and left-over grains contribute to the highly irregular grain boundaries. Some larger grains (1 mm) contain subgrains that are the same size as small recrystallized grains (~100 µm). Mostly uniform extinction.	X	
SC10-38	F	schist	Spaced foliation. The grain boundaries are regular and the quartz crystals are ~100-300 µm. Mostly uniform extinction but some sweeping undulose extinction.	X	
SC10-46	G	quartz vein	Large quartz crystals (~3 mm) with straight grain boundaries. There are a few smaller quartz crystals (~500 µm). Mostly uniform extinction.	X	
SC10-48	H	mylonite	Mylonitic foliation defined by quartz ribbons. The quartz in the ribbons is ~200 µm, and has straight grain boundaries. Large feldspar porphyroclasts. Uniform extinction.		X
SC10-51	I	ultramylonite	Ultramylonite foliation: completely sheared, tiny grains (~10 µm). There are small quartz lenses that have slightly larger crystals (~200 µm). Undulose extinction.		X
SC10-49	J	quartzite ultramylonite	There is crenulation cleavage defined by the micas and the chlorite and quartz ribbons. Straight grain boundaries but there are window, dragging, and pinning microstructures. The quartz in the ribbons (~300 µm) is larger than the quartz in the matrix (~10-20 µm). Core and mantle texture in lenses. Uniform extinction.	X	X
SC10-55	K	quartzite ultramylonite	Ultramylonite foliation: completely sheared, tiny grains (~10 µm). Classic Core and mantle structure in lenses with cores that are ~3mm mantledy by crystals that are ~100-200 µm. There are many subgrains within the cores. Undulose extinction.	X	X

Table 1.4: $^{48}Ti/^{30}Si$ and $^{49}Ti/^{30}Si$ ratios of standards.

#	48Ti/Si	±σ	49Ti/Si	±σ
Mt 1 LT_01	0.00168	4	0.000125	9
Mt 1 LT_02	0.00168	4	0.000123	10
Mt 1 LT_03	0.00216	83	0.000153	58
Mt 1 LT_04	0.00153	22	0.000105	17
Mt 1 LT_05	0.00175	9	0.000123	28
Mt 1 LT_06	0.00148	6	0.000106	20
Mt 1 LT_07	0.00166	7	0.000125	22
Mt 2 LT-01	0.00245	10	0.000172	22
Mt 2 LT-02	0.00228	13	0.000161	35
Mt 2 LT-03	0.00205	12	0.000135	33
Mt 2 LT-04	0.00202	8	0.000136	27
Mt 2 LT-05	0.00210	13	0.000150	19
Mt 2 LT-06	0.00192	6	0.000138	16
Mt 2 LT-07	0.00197	8	0.000138	16
Mt 2 LT-08	0.00202	8	0.000139	18
Mt 3 LT-01	0.00144	5	0.0000989	13
Mt 3 LT-02	0.00159	8	0.000117	11
Mt 3 LT-03	0.00168	6	0.000121	10
Mt 3 LT-04	0.00168	6	0.000123	15
Mt 4 LT-01	0.00141	2	0.0000982	6
Mt 4 LT-02	0.00131	9	0.0000892	9
Mt 4 LT-03	0.00130	3	0.0000932	10
Mt 5 LT-01	0.00107	2	0.0000737	5
Mt 5 LT-02	0.00124	2	0.0000843	6
Mt 5 LT-03	0.00161	55	0.000114	41
Mt 5 LT-04	0.00139	5	0.000101	6
Mt 6 LT-01	0.00139	25	0.000100	15
Mt 6 LT-02	0.00155	8	0.000105	7
Mt 6 LT-03	0.00143	2	0.000101	8
Mt 6 LT-04	0.00144	4	0.000101	6
Mt 7 H-01	2.60E-06	0	0.000000	0
Mt 7 H-02	4.03E-06	0	1.05E-07	0.2
Mt 7 H-03	2.91E-06	0	0.000000	0
Mt 7 H-04	2.95E-06	0	1.29E-07	0.3

Mt 8 LT-01	0.00153	10	0.000108	10
Mt 8 LT-02	0.00141	4	0.0000994	9
Mt 8 LT-03	0.00128	7	0.0000932	7
Mt 9 LT-01	0.00107	2	0.0000773	4
Mt 9 LT-02	0.00119	5	0.0000849	9
Mt 9 LT-03	0.00105	1	0.0000739	3

*Ti concentration of LT natural quartz standard is 39 ppm.

Table 1.5: Titanium concentrations (ppm), and $^{48}T,/^{30}Ti$ and $^{49}Ti/^{30}Si$ ratios of samples.

#	$^{48}Ti/Si$	±σ	$^{49}Ti/Si$	±σ	ppm Ti
SC10-03-01	0.000179909	3	0.0000114	7	4.1
SC10-03-02	0.000635199	7	0.0000503	17	14.5
SC10-03-03	0.00013513	2	0.0000085	6	3.1
SC10-03-04	0.000166111	3	0.0000104	6	3.8
SC10-04-01	0.000225669	3	0.0000150	7	5.2
SC10-04-02	0.000216708	2	0.0000142	5	5.0
SC10-04-03	0.000568192	24	0.0000399	16	13.0
SC10-06-01	0.000103096	2	0.0000070	5	2.4
SC10-06-02	0.000145055	2	0.0000100	7	3.3
SC10-06-03	0.000121648	2	0.0000086	5	2.8
SC10-06-04	0.000109404	2	0.0000093	6	2.5
SC10-12-01	0.000370451	2	0.0000297	7	6.9
SC10-12-02	0.00030749	4	0.0000223	7	5.7
SC10-12-03	0.000140031	1	0.0000097	4	2.6
SC10-12-04	0.000406072	3	0.0000288	9	7.5
SC10-18-01	0.000136505	2	0.0000094	4	2.5
SC10-18-02	6.80E-05	1	0.0000051	3	1.3
SC10-18-03	0.000131746	2	0.0000081	4	2.4
SC10-21-01	7.73E-05	1	0.0000067	5	1.4
SC10-21-02	0.000104507	2	0.0000100	8	1.9
SC10-21-03	7.67E-05	2	0.0000040	4	1.4
SC10-21-04	0.000159876	2	0.0000131	6	3.0
SC10-25-01	0.000100707	1	0.0000069	4	2.5
SC10-25-02	9.46E-05	2	0.0000063	4	2.3
SC10-25-03	0.0001082	1	0.0000070	4	2.6
SC10-26-01	0.000215531	2	0.0000146	5	5.3
SC10-26-02	0.000361959	7	0.0000225	10	8.8
SC10-26-03	0.000276372	3	0.0000195	7	6.7
SC10-29-01	0.00014072	1	0.0000112	5	3.4
SC10-29-02	0.00013842	1	0.0000105	4	3.4
SC10-29-03	0.000143406	2	0.0000113	6	3.5
SC10-29-04	0.00014779	2	0.0000100	5	3.6

SC10-30.1-01	0.000161476	0	0.0000111	1	4.7
SC10-30.1-02	0.000164862	1	0.0000111	3	4.8
SC10-30.1-03	0.000144953	1	0.0000099	2	4.2
SC10-30.2-01	0.000141118	1	0.0000102	3	4.1
SC10-30.2-02	0.000200185	1	0.0000153	3	5.8
SC10-30.2-03	0.000178932	1	0.0000124	3	5.2
SC10-30.3-01	0.000129579	1	0.0000077	2	3.8
SC10-30.3-02	0.000100986	1	0.0000071	2	2.9
SC10-30.3-03	0.000110562	1	0.0000071	0	3.2
SC10-31-01	0.000242649	1	0.0000169	2	7.1
SC10-31-02	0.000235218	1	0.0000161	2	6.9
SC10-31-03	0.000218842	1	0.0000162	2	6.4
SC10-32-01	6.36E-05	2	0.0000044	1	1.9
SC10-32-02	6.12E-05	0	0.0000036	2	1.8
SC10-32-03	6.91E-05	1	0.0000050	2	2.0
SC10-32-04	7.96E-05	1	0.0000061	1	2.3
SC10-33-01	4.30E-05	0	0.0000030	1	1.3
SC10-33-02	5.48E-05	1	0.0000034	1	1.6
SC10-33-03	4.78E-05	1	0.0000030	1	1.4
SC10-33-04	3.02E-05	0	0.0000024	1	0.9
SC10-34-01	5.95E-05	1	0.0000041	1	1.6
SC10-34-02	6.84E-05	1	0.0000039	1	1.8
SC10-34-03	6.72E-05	2	0.0000049	2	1.8
SC10-35bii-01	7.67E-05	1	0.0000051	2	2.1
SC10-35bii-02	5.67E-05	1	0.0000048	2	1.5
SC10-35bii-03	4.99E-05	1	0.0000031	1	1.3
SC10-38-01	7.97E-05	1	0.0000054	1	2.1
SC10-38-02	7.23E-05	1	0.0000042	2	1.9
SC10-38-03	5.34E-05	1	0.0000036	1	1.4
SC10-45-01	0.000340352	2	0.0000226	3	8.2
SC10-45-02	0.000311168	1	0.0000216	3	7.5
SC10-45-03	0.000316495	1	0.0000226	3	7.7
SC10-45-04	0.000340091	1	0.0000226	3	8.2

SC10-46-01	4.48E-05	0	0.0000031	1	1.1
SC10-46-02	5.67E-05	1	0.0000040	1	1.4
SC10-46-03	3.57E-05	0	0.0000025	1	0.9
SC10-46-04	4.28E-05	1	0.0000030	1	1.0
SC10-48-01	9.38E-05	1	0.0000068	3	2.6
SC10-48-02	4.81E-05	2	0.0000032	3	1.3
SC10-48-03	3.70E-05	1	0.0000020	1	1.0
SC10-48-04	4.30E-05	1	0.0000023	2	1.2
SC10-49-01	1.12E-05	0	0.0000008	1	0.3
SC10-49-02	6.35E-05	3	0.0000047	3	1.8
SC10-49-03	1.71E-05	0	0.0000011	1	0.5
SC10-49-04	0.000108078	1	0.0000053	1	3.0
SC10-51-01	0.000576239	3	0.0000432	4	20.4
SC10-51-02	3.49E-05	1	0.0000014	2	1.2
SC10-51-03	1.01E-05	0	0.0000006	1	0.4
SC10-55-01	7.52E-05	2	0.0000051	2	2.7
SC10-55-02	6.46E-05	2	0.0000044	2	2.3
SC10-55-03	7.11E-05	1	0.0000053	2	2.5
SC10-55-04	7.69E-05	3	0.0000041	2	2.7

Table 1.6: Representative electron microprobe analyses of garnet, plagioclase, and other major silicate minerals

Garnet

Sample	SC10-18	SC10-18	SC10-18	SC10-18	SC10-26	SC10-26	SC10-26	SC10-26
Analysis	25	26	28	30	2	3	4	5
Na	0.007	0.003	0.002	0.002	0.003	0.002	0.005	0.003
Mg	0.305	0.331	0.319	0.329	0.409	0.386	0.371	0.359
Si	2.916	2.927	2.913	2.927	2.943	2.936	2.953	2.950
Al	2.029	2.009	2.017	2.010	2.009	2.045	2.022	2.035
Ca	0.402	0.320	0.373	0.340	0.579	0.569	0.585	0.618
Mn	0.095	0.080	0.080	0.095	0.065	0.067	0.073	0.068
Fe	2.314	2.391	2.369	2.365	2.039	2.031	2.021	1.994
K	-	-	0.001	0.001	0.001	0.001	0.004	0.000
Ti	0.002	0.004	0.003	-	0.003	0.003	0.004	0.003
Ba	-	0.001	0.001	0.001	0.001	-	-	-
Wt% Total	99.085	98.655	98.805	98.743	99.797	100.677	100.603	100.363
Alm	0.742	0.766	0.754	0.756	0.659	0.665	0.663	0.656
Grs	0.129	0.102	0.119	0.109	0.187	0.186	0.192	0.203
Prp	0.098	0.106	0.102	0.105	0.132	0.126	0.122	0.118
Sps	0.031	0.026	0.025	0.030	0.021	0.022	0.024	0.022
Fe/(Fe+Mg)	0.883	0.878	0.881	0.878	0.833	0.840	0.845	0.847

Cations are normalized to an anhydrous basis of 12 oxygens

Plagioclase

Sample	SC10-18	SC10-18	SC10-18	SC10-18	SC10-26	SC10-26
Analysis	2	3	4	5	37	39
Xan(%)	0.161	0.164	0.164	0.162	0.391	0.393
Wt% total	100.777	99.038	99.595	99.033	99.136	100.013

Muscovite and Biotite

Sample	SC10-18	SC10-18	SC10-18	SC10-18	SC10-26	SC10-26	SC10-26	SC10-26	SC10-26
Mineral	Bt	Bt	Bt	Ms	Bt	Bt	Bt	Bt	Ms
Analysis	27.000	28.000	29.000	22.000	47.000	48.000	56.000	58.000	46.000
Na	0.017	0.019	0.025	0.093	0.032	0.033	0.024	0.030	0.088
Mg	1.302	1.311	1.302	0.149	1.552	1.539	1.536	1.544	0.155
Si	2.758	2.751	2.759	3.103	2.743	2.750	2.755	2.745	3.109
Al	1.575	1.573	1.561	2.635	1.604	1.611	1.611	1.585	2.668
Ca	0.003	0.001	0.002	0.003		0.001			
Mn	0.013	0.012	0.011	0.001	0.007	0.007	0.008	0.008	
Fe	1.120	1.127	1.126	0.088	0.889	0.881	0.877	0.893	0.070
K	0.931	0.933	0.934	0.971	0.903	0.896	0.902	0.897	0.882
Ti	0.104	0.106	0.108	0.032	0.094	0.094	0.094	0.110	0.032
Ba	0.001		0.001	0.004	0.004	0.004	0.003	0.004	0.007
Wt%tot	93.590	94.117	93.665	94.124	94.181	94.203	94.979	94.687	93.721
Fe/(Fe+Mg)	0.463	0.462	0.464	0.372	0.364	0.364	0.363	0.366	0.310

Cations normalized to an anyhydrous 11 oxygens

* Biotite composition corrected for ReNTR's

References

Behr, W.M., Thomas, J.B., and Hervig, R.L., 2011, Calibrating Ti concentrations in quartz for SIMS determinations using NIST silicate glasses and application to the TitaniQ geothermobarometer: American Mineralogist, v. 96, No. 7, p. 1100 1106.

Berman, R.G., 1990, Mixing properties of Ca-Mg-Fe-Mn garnets: American Mineralogist, v. 75, p. 328-244.

Cherniak, D.J., Watson, E.B., and Wark, D.A., 2006, Ti diffusion in quartz: Chemical Geology, v. 236 p. 65-74.

Cherniak, D.J and Watson, E.B., 2007, Ti diffusion in zircon: Chemical Geology, issues 3-4, p. 470-483.

Corrie, S.L., 2010, Geochemical and geochronological constraints on the tectonothermal history of the Central and Eastern Nepal Himalaya: BSU dissertation.

Engwell, S., and Hall, M., 2008, Epoxy resins: Natural Environment Research Council.

Ferry, J.M., and Spear, F.S., 1978,Experimental calibration of partitioning of Fe and Mg between biotite and garnet: Contributions to Mineralogy and Petrology, v. 107, p. 487-500.

Fitzgerald, J.D., Etheridge, M.A., and Vernon, R.H., 1983, Dynamic recrystallization in a naturally deformed albite: Textures and Microstructures, v. 5, no. 4, p. 219-237.

Gee, D.G., 1975, A tectonic model for the central part of the Scandinavian Caledonides: Journal of American Science, v. 275A, p. 468-515.

Gee, D.G., and Sturt, B.A., 1985, Scandinavian Caledonides Tectonostratigraphic Map: John Wiley and Sons Ltd.

Gee, D.G., Juhlin, C, Pascal, C, and Robinson, P., 2010, Collisional Orogeny in the Scandinavian Caledonides (COSC): GFF, v. 132, p. 29-44.

Ghent, E.D., and Stout, M.Z., 1981, Geobarometry and geothermometry of plagioclase-biotite-garnet-muscovite assemblages: Contributions to Mineralogy and Petrolology, v. 76, p. 92-97.

Griffin, W.L., and Brueckner, H.K., 1980, Caledonian Sm-Nd ages and a crustal origin for Norwegian eclogites, Nature, v. 285, p. 319-321.

Grujic, D., Stipp M., and Wooden, J.L., 2011, Thermometry of quartz mylonites: Importance of dynamic recrystallization on Ti-in-quartz reequilibration: Geochemistry Geophysics Geosystems, v. 12,no. 6, doi: 10.1029/2010GC003368.

Henry, P., Le Pichon, X., and Goffe, B., 1996, Kinematic, thermal and petrological model of the Himalayas: constraints related to metamorphism within the underthrust Indian crust and topographic elevation: Tectonophysics, v. 273, p. 31-56.

Hirth, G., and Tullis, J., 1992, Dislocation creep regimes in quartz aggregates: Journal of Structural Geology, v. 14, issue 2, p. 145-159.

Hoisch, T.D., 1990, Empirical calibration of six geobarometers for the mineral assemblage quartz+muscovite+biotite+plagioclase+garnet: Contributions to Mineralogy and Petrology, v. 104, p. 225-234.

Kohn, M.J., and Spear, F.S., 2000, Retrograde Net Transfer Reaction (ReNTR) insurance for P-T estimates: Geology, v. 28, p. 1127-1130.

Kohn, M.J., 2008, P-T-t data from central Nepal support critical taper and repudiate large scale channel flow of the Greater Himalayan Sequence: GSA Bulletin, v. 120, p. 259-273.

Kohn M.J., and Northrup C.J., 2009, Taking mylonites' temperature: Geology, v. 37, no. 1, p. 47-50, doi: 10.1130/G25081A.1.

Levien, L., Prewitt, C.T., and Weidner, D.J., 1980, Structure and elastic properties of quartz at pressure: American Mineralogist, v. 65, p. 920-930.

Northrup, C.J., 1996a, Structural expressions and tectonic implications of general noncoaxial flow in the midcrust of a collisional orogeny: the northern Scandinavian Caledonides: tectonics, v. 15, no. 2, p. 490-505.

Northrup, C.J., 1996b, Tectonic evolution of the Caledonian collisional system, Ofoten-Efjorden, north Norway: Massachusetts Institute of Technology: Dissertation.

Passchier, C.W., and Trouw, R.A.J., 1998, Microtectonics: Springer; New York.

Roberts, D., and Gee, D.G., 1985, An introduction to the structure of the Scandinavian Caledonides, in the Caledonide Orogen –Scandinavia and related areas: p. 55-68.

Rusk, B.G., Lowers, H.A., and Reed, M.H., 2008, Trace elements in hydrothermal quartz: Relationships to cathodoluminescent textures and insights into vein formation: Geology, v. 36, no. 7, p. 547-550.

Smith, L.B., Jr., 2006, Origin and reservoir characteristics of Upper Ordovician Trenton–Black River hydrothermal dolomite reservoirs in New York: American Association of Petroleum Geologists (AAPG) Bulletin, v. 90, p. 1691–1718, doi: 10.1306/04260605078.

Spear, F.S., 1993, Metamorphic phase equilibria and pressure-temperature-time paths: Mineralogical Society of America Monograph, Washington, D.C.,

Spear, F.S., and Cheney, J.T., 1989, A petrogenic grid for pelitic schists in the system SiO_2-Al_2-FeO-MgO-K_2O-H_2O: Contributions to Mineralogy and Petrology, v. 101, no. 2, p. 149-164, doi: 10.1007/BF00375302.

Spear, F.S., and Wark, D.A., 2009, Cathodoluminescence imaging and titanium thermometry in metamorphic quartz: Journal of Metamorphic Geology, v. 27, p. 187-205.

Stipp, M., Stunitz, H., Heilbronner, R., and Schmid, S.M., 2002, The eastern Tonale fault zone: a 'natural laboratory' for crystal plastic deformation of quartz over a temperature range from 250-700°C: Journal of Structural Geology, v. 24, issue 12, p. 1861-1884.

Thomas, J.B., Watson, E.B., Spear, F.S., Shemella, P.T., Nayak, S.K., and Lanzirotti, A., 2010, TitaniQ under pressure: the effect of pressure and temperature on the solubility of Ti in quartz: Contributions to Mineralogy and Petrology.

Wark, D.A., and Watson, E.B., 2006, TitaniQ: a titanium-in-quartz geothermometer: Contributions to Mineralogy and Petrology, v. 152, p. 743-754.

White, J.C., and Mawer, C.K., 1988, Dynamic recrystallization and associated exsolution in perthites: Evidence of deep crustal thinning: Journal of Geophysical Research, v. 93, no. B1, p. 325-337, doi: 10.1029/JB093iB01p00325.

Winter, J.D., 2001, An introduction to igneous and metamorphic petrology: Prentice Hall, New Jersey.

CHAPTER TWO: IMPLICATIONS OF TITANIQ TEMPERATURES FOR THE THERMAL AND KINEMATIC EVOLUTION OF THE SCANDINAVIAN CALEDONIDES AND MODERN COLLISIONAL OROGENS

Abstract

Two competing end-member models for the steady state thermal and kinematic evolution of orogens exist: The critical wedge model and the channel flow-extrusion model. Due to the unusual and consistent exposure of thrust surfaces for ~140 km across the orogen, the Caledonides provide insights into the down-dip behavior of thrusts not determinable in other collisional orogens. Using TitaniQ, in combination with other thermometers and barometers, to obtain precise and accurate pressure-temperature estimates of quartz recrystallization in the Northern Scandinavian Caledonides, we resolve a consistent down-dip thermal gradient along the basal thrust shear zone of 1.43 ± 2°C/km. This low thermal gradient supports the critical wedge model for the evolution of the Caledonides. We suggest that the Caledonides formed from critical wedge mechanics together with general non-coaxial flow and gravitational spreading of the nappes. In addition to resolving a down-dip thermal gradient across the Caledonides basal shear zone, we calculated strain rates for quartz deformation ranging from $1.00E^{-22}$ to $1.00E^{-13}$ s^{-1}.

2.1 Introduction

Upper crustal geologic processes can be studied in active orogens (e.g., the Himalaya, the Andes). However, deeper crustal processes are not determinable in active orogens, so we must look to ancient orogens to understand geologic processes occurring in the middle and lower crust (Andresen et al., 2007). Due to the unusual and consistent exposure of thrust surfaces for ~140 km across the orogen, the deeply eroded remains of the late Silurian-early Devonian Scandinavian Caledonides (Gee and Sturt, 1985) provide a natural laboratory to test competing models of the thermal and kinematic evolution of orogens.

Two such competing models for the thermal and kinematic evolution of orogens are 1) the channel flow-ductile extrusion model and 2) the critical wedge model. The channel flow-extrusion model treats the middle and lower crust as mechanically weak layers that dominate the metamorphic and structural development of the orogen when coupled with focused denudation (Zeitler et al., 2001; Beaumont et al., 2001, 2004; Jamieson et al., 2002, 2004). The critical wedge model is the classic model of wedge evolution in which the wedge is accreted by forward propagating thrust faults (Royden, 1993; Henry et al., 1997; Harrison et al., 1998; Huerta et al., 1998; Bollinger et al., 2006). The critical wedge model suggests that weak portions of the crust might exist at depth but they do not induce flow or otherwise control overall thermal and mechanical behavior (Kohn, 2008). Fortunately, both models predict different systematic trends in P-T conditions and P-T-t histories for rocks exposed at the surface, so we can compare our observations to discriminate among models.

We have resolved the thermal gradient in the transport direction along the main basal thrust zone (MBT) via Titanium-in-Quartz (TitaniQ) thermometry from the Scandinavian Caledonides to discriminate among models. The evolution of the Caledonides involved some amount of general non-coaxial flow (Northrup, 1996) and possibly evolved by gravitational spreading of the nappes (Ramberg, 1977, 1981; Sanderson, 1982). Both the channel flow-extrusion model and the critical wedge model have been advocated for the Indo-Tibetan Himalaya.

In addition, we have calculated strain rates for mylonites that deformed during the main Caledonian event using temperatures calculated via TitaniQ thermometry and recrystallized quartz grain paleopiezometry. Flow laws and strain rates are critical to understanding deformation conditions in the earth and may allow us to better understand crustal viscosities (Kohn and Northrup, 2009), and constrain the strength of the crust (Kohlstedt and Weathers, 1980; Ord and Christie, 1984).

2.2 Background

2.2.1 Tectonic Setting

The Scandinavian Caledonides (Figure 2.1) formed during the late Cambrian to early Devonian periods, in response to contractional tectonic events known as the Caledonian orogeny. These events culminated in extensive syn-to-post metamorphic, southeastward thrusting of diverse rock complexes onto autochthonous, foreland sedimentary successions (Roberts, 2003). The first such event, the Finnmarkian, occurred during the late Cambrian/earliest Ordovician (520-500 Ma). This event was marked by the subduction of the Baltoscandian margin of Baltica beneath a magmatic arc that was

positioned in the Aegir Sea, which separated Baltica from Siberia. The second event, the Trondheim event, took place during the early Ordovician (480-475 Ma). This event was marked by the seaward subduction of a microcontinent that had earlier rifted off of Baltica. At this time, Baltica had already started to rotate counter-clockwise away from Siberia so that it now faced Laurentia across a gradually contracting Iapetus Ocean. The Trondheim event was followed by the Taconian event, which occurred during the mid-to-late Ordovician. This event was marked by the seaward subduction of the continental margin of Laurentia beneath a diverse arc complex, which was positioned in the Iapetus Ocean. Finally, these contractional events culminated in the late Silurian/early Devonian periods (circa 430-400 Ma) during the Scandian event. The Scandian event is considered the main orogenic event in this region, and it was marked by the oblique, southeastward directed collision of Laurentia into Baltica (Roberts, 2003).

During the Scandian event, the western margin of Baltica was subducted westward to deep levels, and a crustal-scale composite allochthon was thrust eastward onto the Baltic craton (Griffin and Brueckner, 1980; Hodges et al., 1982; Stephens and Gee, 1989). This large composite allochthon, or orogenic wedge, was separated from the Precambrian basement (Baltica) by a weak decollement zone (Fossen, 1992, 2000), which has been inferred to dip at low angles (c. 1-2°) westwards, and then steepen beneath the hinterland of the orogen towards the Norwegian coast (Gee et al., 2010).

The thrust sheets making up the orogenic wedge were derived from the rifted margin of Baltica, the Iapetus Ocean basin, and rocks of Laurentian affinity (Roberts and Gee, 1985). The thrust sheets can be categorized as the Lower Allochthon, the Middle Allochthon, the Upper Allochthon, or the Uppermost Allochthon. The lower and middle

Allochthons are of Baltican affinity and consist mainly of gneisses and metamorphosed sedimentary cover rocks. The Upper Allochthon can be subdivided into the Särv, the Seve, and the Köli Nappes. The Särv and the Seve Nappes are derived from the outer margin of the continent Baltica (Gee et al., 2010) and the Köli Nappes, which consist of metabasalts and metamorphosed deep marine sediments, are derived from the Iapetus Ocean basin. Lastly, the Uppermost Allochthon is of Laurentian affinity and also consists of metamorphosed shallow marine sediments and accretionary prisms (Gee, 1975; Northrup, 1997; Gee et al., 2010). The metamorphic grade in the Lower and Middle allochthons increases upwards into the Seve Nappes and then decreases abruptly in the overlying Köli Nappes. The decrease in metamorphic grade occurs across extensional faults (Gee et al., 2010).

At least four ultrahigh pressure (UHP) events affected the Scandinavian Caledonides within a 100 m.y time span (Brueckner and van Roermund, 2004). These events are evidenced by the concentration of UHP coesite- and diamond-bearing eclogites and garnet peridotites (Hacker, 2007). Eclogites have been found in the Baltican basement rocks, in the sedimentary cover rocks, the Middle Allochthon rocks, the Middle Allochthon's sedimentary cover rocks, and the Upper Allochthon rocks (Hacker, 2007). The best known exposure of eclogites in the Scandinavian Caledonides, and perhaps the world, is in the Western Gneiss Region, Norway. These eclogites are hosted in migmatitic gneisses that record polyphase metamorphism, significant melting, and intense shearing (Tucker et al., 1990; Andersen et al., 1991; Hacker et al., 2003, 2010; Terry and Robinson., 2003, 2004; Brueckner and Van Roermund, 2004; Engvik et al., 2007; Fossen., 2010). These UHP and HP rocks along the western coast of Norway

have been interpreted to record underthrusting of Baltica underneath Laurentia, followed by orogenic extension and the formation of Devonian sedimentary basins.

Caledonian deformation is inferred to have involved the entire crust in westernmost Norway, in the hinterland of the orogen. On the other hand, deformation is inferred to be concentrated only in the upper crust in Eastern Norway and Sweden (Gee et al., 2010). The amount of Caledonian contraction in the lower crust is difficult to estimate because geophysical data yield different interpretations, and direct evidence from the lower crust is lacking.

In response to extreme crustal thickening, the Caledonides underwent post-collisional extension during the Devonian period (Norton, 1986; Fossen, 1992; Northrup, 1997; Roberts, 2003; Braathen et al., 2000). This extension involved the reactivation of the MBT as a west/northwest directed normal fault (displacement > ~30 km; Fossen and Rykkelid, 1992), along with the development of smaller west/northwest directed normal faults within the nappe stack (Fossen, 1992).

Extension in the upper crustal levels is also believed to have occurred during the Caledonian orogeny, while thrusting was occurring at deeper crustal levels (Andersen et al., 1991; Gee et al., 1994). This syn-collisional extension is reported in NE Greenland (Andresen et al., 2007), the Ofoten-Efjorden region of the Scandinavian Caledonides (Northrup, 1996), and the central Caledonides (Gee et al., 1994). Unroofing of high-pressure rocks in the Western Gneiss Region of southern Norway occurred while thrusting continued in the foreland (Andersen et al., 1991) and further supports syn-collisional extension in the Scandinavian Caledonides.

Extension, along with erosion, forced the exhumation and exposure of rocks from all major structural levels in the orogen. Today, the Caledonides consist of a thin but regionally extensive remnant of the original nappe stack lying structurally above autochthonous or parautochthonous rocks of the Baltic craton and its pre-Caledonian sedimentary cover (Roberts and Gee, 1985).

2.2.2 The Channel Flow Model

The channel flow extrusion model (Beaumont et al., 2001, 2004; Jamieson et al., 2004; Figure 2.2) links overall wedge geometry with profoundly weak middle and lower crustal levels that behave ductilely, advecting and transporting heat and partially molten rock up to ~150 km in tens of m.y to the thrust front (Kohn, 2008) when coupled with an erosional front. As the migmatitic rocks move upward and toward the foreland, they advect "extra heat" yielding high temperatures at low pressures (Kohn, 2008). The extra heat essentially contact metamorphoses surrounding rocks and decreases their viscosities by "melt weakening," or in-situ partial melting (Jamieson et al., 2004). Beaumont et al. (2001) used coupled thermal-mechanical numerical models to show that channel flow and ductile extrusion may be dynamically linked through the effects of surface denudation focused at the edge of a plateau that is underlain by low-viscosity material.

CFM predicts that heat and mass are transported horizontally in a channel-like conduit with coeval thrust- and normal-sense distributed shear across the lower and upper parts of the channel. The presumed channel retains its geometry, persists over geologic time periods, and dominates the structural and metamorphic development of the orogen (Zeitler et al., 2001; Beaumont et al., 2001, 2004; Jamieson et al., 2002, 2004). Thus, the model predicts a large-scale effect of the channel.

Flow in the channel requires an inclined thrust surface and focused denudation at the thrust front (the high-relief transition between plateau and foreland) as deformation focuses into the channel (Beaumont et al., 2001, 2004; Kohn, 2008). The channel, and its susceptibility to large-scale horizontal flow, is initiated by a reduction in viscosity, due to the increase in melt-fraction of the thickened crust, and the difference in horizontal pressure between the internal, thick orogenic crust and external, thin crust (Beaumont et al., 2004). The channel flow model predicts an inverted metamorphic sequence: peak P-T conditions in the sillimanite stability field (Corrie, 2010; Kohn, 2008); peak metamorphic pressures that decreases structurally downward; and retrograde isothermal exhumation until rocks begin cooling relatively close to the surface (Kohn, 2008; Corrie, 2010). It also predicts a high thermal gradient along the thrust surface (tens of °C/km).

2.2.3 The Critical Wedge (Taper) Model

The Critical Wedge model is the classic model of wedge evolution (Royden, 1993; Henry et al., 1997; Harrison et al., 1998; Huerta et al., 1998, 1999; Bollinger et al., 2006; Figure 2.3). The wedge is made up of allochthonous sheets that are thrust upon each other during convergence. The model does not preclude weak portions of the crust and partial melts at depth, but suggests that the partial melts never approach the thrust front. In other words, the effect of a presumed channel is small and does not induce flow: the partial melts at depth are not transported to the orogenic front and a flow channel has only a minor influence on the overall thermal and mechanical behavior of the orogen (Kohn, 2008). Critical wedge theory is based on mechanical models that assume a wedge of deforming rock is everywhere at a condition of critical failure (Dahlen, 1990), and is accommodated by in-sequence thrusting. However, normal faulting may occur if the

wedge becomes super-critical (the combination of internal strength of the wedge and the shear stress across its base are insufficient to support the topographic gradient; Platt, 1986). In general, a wedge may grow by accretion of new material, or a wedge may maintain its size if erosion is coupled by underplating of new material to the base. Metamorphic field gradients are strongly influenced by details regarding erosion and underplating rates (Henry et al., 1996).

Critical wedge advects much less heat than channel flow, and thus produces relatively low temperatures at high pressures (Henry et al., 1996; Kohn, 2008). The critical wedge model predicts P-T conditions well within the kyanite stability field; initial retrograde isobaric cooling; "hairpin" P-T paths; and relatively slow cooling rates (Kohn, 2008). It also predicts a low thermal gradient (a few °C/km) along the thrust surface.

2.2.4 Gravitational Spreading of Nappes

The Gravitational Spreading of Nappes (GSN; Ramberg, 1977, 1981; Sanderson, 1982) is a model for the emplacement of thrust nappes that have undergone transport-parallel elongation during thrusting (Northrup, 1996). GSN assumes general non-coaxial flow in the middle and lower crust. It is driven by critical wedge kinematics, but it incorporates flow dynamics. Deformation within the nappes results from a dynamic interaction between plate tectonic convergence and the force of gravity acting on the nappe stack (Northrup, 1996). In this model, rocks in the middle and lower crust are weakened due to increased radioactive heat production of the thickened crust. The strong upper crust then compresses the soft, partially molten rocks in the middle and lower crust, which induces flow in all directions. Thus, general non-coaxial flow has the effect of attenuating the wedge and may be evidenced by a multi-directional stretching lineation in

the fabric of mylonites. Unlike CFM, general non-coaxial flow does not maintain a channel-like conduit and does not persist over geologic time. Unlike CFM, both thrust and normal movement may occur individually or simultaneously in the upper crust during GSN.

Flow may represent an important kinematic link between contemporaneous normal faulting at shallow crustal levels and thrusting at deep crustal levels. General non-coaxial flow can produce simultaneous foreland directed structural transport, penetrative thinning, and transport-parallel elongation at deep levels of the nappe stack (Northrup, 1996).

2.2.5 Tectonic Setting and Kinematic Model of the Himalaya

The Himalayan-Tibetan Orogen is a large orogen that serves as the type example of continent-continent collisions. The main phase of thrusting began 20-25 Ma (Henry et al., 1996) and continues today with the whole Indian crust underthrusting below the crustal wedge of the High Himalaya at a rate of about 15-20 mm/yr (Bilham et al., 2003). Today, the average elevation in the High Himalaya exceeds 5000 m and the Tibetan plateau is roughly 4000-5000 m (Henry et al., 1996). Since 20 Ma, shortening across the range has been primarily taken up by slip along a single thrust fault, the main Himalayan thrust (MHT; Bollinger et al., 2006), which dips approximately 10° (Brown et al., 2006). All major thrust faults sole into the MHT, along which, the Indian crust is buried beneath the southern edge of Tibet. The Main central thrust (MCT) separates the High Himalayan Crystallines (HHC) from the Lesser Himalayan Sequence (LHS) and is thought to be the major thrust fault that has contributed to the formation of the Himalaya (Bollinger et al., 2006). The MCT was activated in the early Miocene. The Greater Himalayan sequence

(GHS) is comprised of high grade metamorphic rocks between coeval thrust- and normal-sense shear zones corresponding to the South Tibetan Detachment (STD) and the MCT.

The present average erosional rate over the whole Himalayan belt is ~1 mm/yr (for the last 25-30 Myr; Henry et al., 1996); however, local denudation rates have been episodically higher (1.1 to 8 mm/yr; Copeland and Harrison, 1990; Pecher, 1989; Kohn, 2004), which may be related to tectonic events, expressed as extensional movement along the STD and North Himalayan Fault systems. Denudation rates are also geographically variable.

Beaumont et al. (2001, 2004) have called upon channel flow coupled with ductile extrusion in the middle to lower crust to explain the outward growth of the Tibetan plateau and the exhumation of the migmatitic rocks of the GHS. According to these geoscientists, channel flow coupled with focused denudation at the thrust front provides an internally consistent explanation for the tectonic exposure of the Greater Himalayan Sequence (GHS) and its relationship to its bounding shear zones, the South Tibetan Detachment (STD) system, and the Main Central Thrust (MCT) system. Bollinger et al. (2006) have documented an inverse thermal metamorphic gradient throughout the Lesser Himalayan Sequence (LHS).

On the other hand, Kohn (2008) repudiates large-scale channel flow of the GHS and supports CTM for the Himalaya based on P-T-t data from central Nepal. Metamorphic and chronologic patterns are matched well by expectations of critical wedge models and contrast significantly with published channel flow models.

2.3 Methods

We determined temperatures of deformation using TitaniQ thermometry on 23 samples from the Scandinavian Caledonides in Norway and Sweden. We used these temperatures, together with the measured lateral distance from the thrust front, to resolve a thermal gradient. In principal, a high thermal gradient (tens of °C/km) would support CFM, whereas a low thermal gradient (a few °C/km) would support CTM or GSN.

We optically determined recrystallized grain sizes and identified the transitions between dislocation creep regimes (Hirth and Tullis, 1992; Stipp et al., 2010) for flow stress calculations. Flow stress (σ), or the yield strength, is defined as the instantaneous value of stress required to keep the material deforming. Flow stress was calculated using the recrystallized grain size piezometer for quartz:

$$\sigma^{1.26\pm0.13} = D^{-1} * 10^{3.56\pm0.27} \quad \text{Eq. 1}$$

Where D is the diameter of the recrystallized quartz grain (Stipp and Tullis, 2003), which corresponds to dislocation creep regimes 2 and 3 (Hirth et al., 2001). Error propagation was calculated using numerical error analysis (Roddick, 1987). Strain rate was calculated by the formula:

$$\dot{\varepsilon} = A f_{H_2O}^{m} \sigma^{n} \exp(-\frac{Q}{RT}) \quad \text{Eq. 2}$$

Where A is a material parameter, and $\log(A) = -11.2 \pm 0.6\ MPa^{-(n+m)}$, f_{H_2O} is water fugacity at each pressure and temperature (Burnham et al., 1969), m is the water fugacity exponent (= 1), σ is the flow stress or differential stress, n is the stress exponent (= 4), Q = 135 kJ/mol, R is the ideal gas constant ($8.31 \frac{\text{J}}{\text{molK}}$), and T is the absolute temperature (Hirth et al., 2001), which we calculated via TitaniQ. Hirth et al. (2001) determined material constants for the strain rate equation by combining natural and experimental

constraints, and they determined external variables by thermochronological, structural, and microstructural observations from the Ruby gap duplex, central Australia. They evaluated the applicability of different quartzite flow laws at natural conditions after establishing that the same deformation processes operate at geological and experimental conditions. Error arises because dislocations in regime three move with a higher velocity than in regime 2 (Hirth et al., 2001), and therefore may experience different activation energies in nature.

Example calculation: Flow stress (σ) and strain rate ($\dot{\varepsilon}$) for sample SC10-26:

$$\sigma^{1.26\pm0.13}(\mathrm{MPa}) = 200(\mu\mathrm{m})^{-1} * 10^{3.56\pm0.27}$$

$$\sigma = 9.98\ \mathrm{MPa}$$

$$\dot{\varepsilon} = (6.31 * 10^{-12})(406.3\ \mathrm{MPa})^{1}(9.98\ \mathrm{MPa})^{4}\exp\left(\frac{-135\ \frac{\mathrm{kJ}}{\mathrm{mol}}}{\left(8.31\ \frac{\mathrm{J}}{\mathrm{molK}}\right)(767^{\circ}\mathrm{K})}\right)$$

$$\dot{\varepsilon} = 1.62 * 10^{-14}\mathrm{s}^{-1}$$

2.4 Results

In Chapter 1, I calculated TitaniQ temperatures for samples that recrystallized along a ductile shear zone. I plotted Temperature v. Distance from the Thrust Front and observed that deformation temperatures ranged from ~210°C at the thrust front to 475°C at the deepest structural levels. I fit a line through the minimum temperatures at each location to resolve a thermal gradient of 1.7 ± 0.5°C/km along the shear zone (Figure 1.14). Using these minimum temperatures, I calculated strain rates ranging from $1*10^{-22}$ to $1*10^{-12}$ s^{-1}. I resolved a weak trend to lower strain rates farther from the thrust front and deeper in the crust (Figure 2.4, C and D). My data also show that strain rate is higher at lower temperatures (Figure 2.4, A) and in smaller grains (Figure 2.5, C).

I constrained the transition between dislocation creep regimes 2 and 3 at flow stresses between 20 and 105 MPa (Figure 2.5, B), consistent with the transition estimated by Hirth et al. (~65-100 MPa; 2001).

2.5 Discussion

A critical wedge model for the thermal and kinematic evolution of the Caledonides is supported by 1) a low thermal gradient of 1.7 ˚C/km; 2) the absence of high temperatures near the thrust front; and 3) strain rates typical of crustal settings, all of which repudiate the effect of a large scale channel. Due to melt weakening, strain rates at the base of a crust deforming by CFM will typically be higher than strain rates at the base of a crust deforming by CTM.

Critical wedge geometry, linked with general non-coaxial flow in the mid-crust would account for foreland-directed transport, subvertical thinning, and transport-parallel elongation of the rock mass at depth (Northrup, 1996), and could explain coeval upper crustal extension and contractional thrusting at deeper crustal levels. In the Caledonides, general non-coaxial flow occurred during the Scandian orogeny, prior to, and during the main Caledonian orogeny (Northrup, 1996), and is evidenced by spreading lineation in all directions. Therefore, we suggest that the Caledonides formed by critical wedge kinematics accompanied by Gravitational Spreading of the Nappes.

One argument for a channel flow model of the Caledonides would be the presence of partial melt migmatites at the thrust front. However, migmatites cannot be observed at the thrust front, even if they existed there before, because the upper crust of the Caledonian orogen has been removed. And although migmatites are present in NE Greenland and in the Western Gneiss Region of Norway, they are thought to have

resulted from magmatic activity due to basaltic underplating (Andresen et al., 2007), and not from channel flow. Granulitic migmatites in the Seve Nappe complex are also thought to have originated from the Baltoscandian margin before emplacement eastward onto Baltica (Gee et al., 2008), and not from channel flow.

2.5.1 Comparison with the Himalayan Orogen

There are broad similarities in deformation patterns between the Scandinavian Caledonides, and the Indo-Tibetan Himalaya. We propose that the tectonic model supported in this study may be analogous to the tectonic evolution of the Himalaya. At high structural levels of the Himalaya, normal faulting along the South Tibetan Detachment System (STDS) occurred contemporaneously with continued movement along the Main Central Thrust (MCT) at the base of the allochthon, similar to the coeval thrusting and extension that occurred in Scandinavia at different crustal levels during the main Caledonian event (Northrup, 1996).

2.5.2 Strain Rate Implications

The strain rates we calculated are typical of crustal settings deforming in a ductile shear zone. Strain rates in a ductile shear zone range from $1*10^{-6}$ s^{-1} at the brittle-ductile transition, where deformation transitions from microcracking to dominantly dislocation motion (Tullis and Yund, 1977), to infinitely low strain rates at crustal depths. While formatting our strain rate axes in Figures 2.4, A, C, and D, and 2.5, A, and C, I pinned the upper bound at $1*10^{-6}$ s^{-1} and our lower bound at $1*10^{-25}$ s^{-1}, which I considered a reasonable minimum strain rate at the base of a deforming crust (the rate at which the base of the crust deformed).

Finally, I observed dislocation creep regimes 2 and 3 occurring at temperatures much lower than previously estimated (see Chapter 1; Hirth and Tullis, 1992), which might explain why Hirth et al.'s (2001) transition falls within the upper end of our range (Figure 2.5, B).

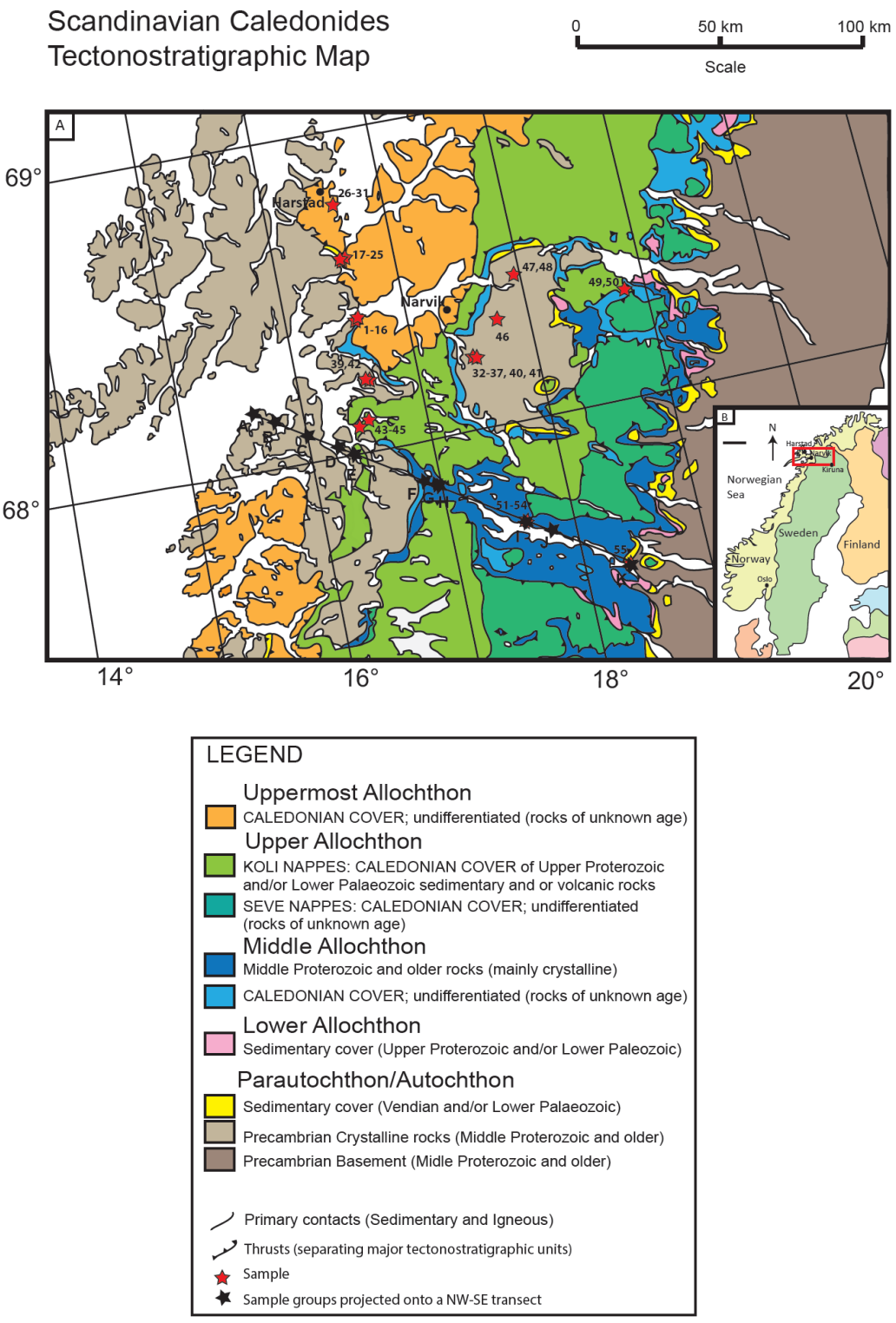

Figure 2.1: A) Tectonostratigraphic map of the northern Scandinavian Caledonides adapted from (Gee and Sturt, 1985) with sample collection locations, and sample collection groups. B) Map of Scandinavia showing field area in red rectangle.

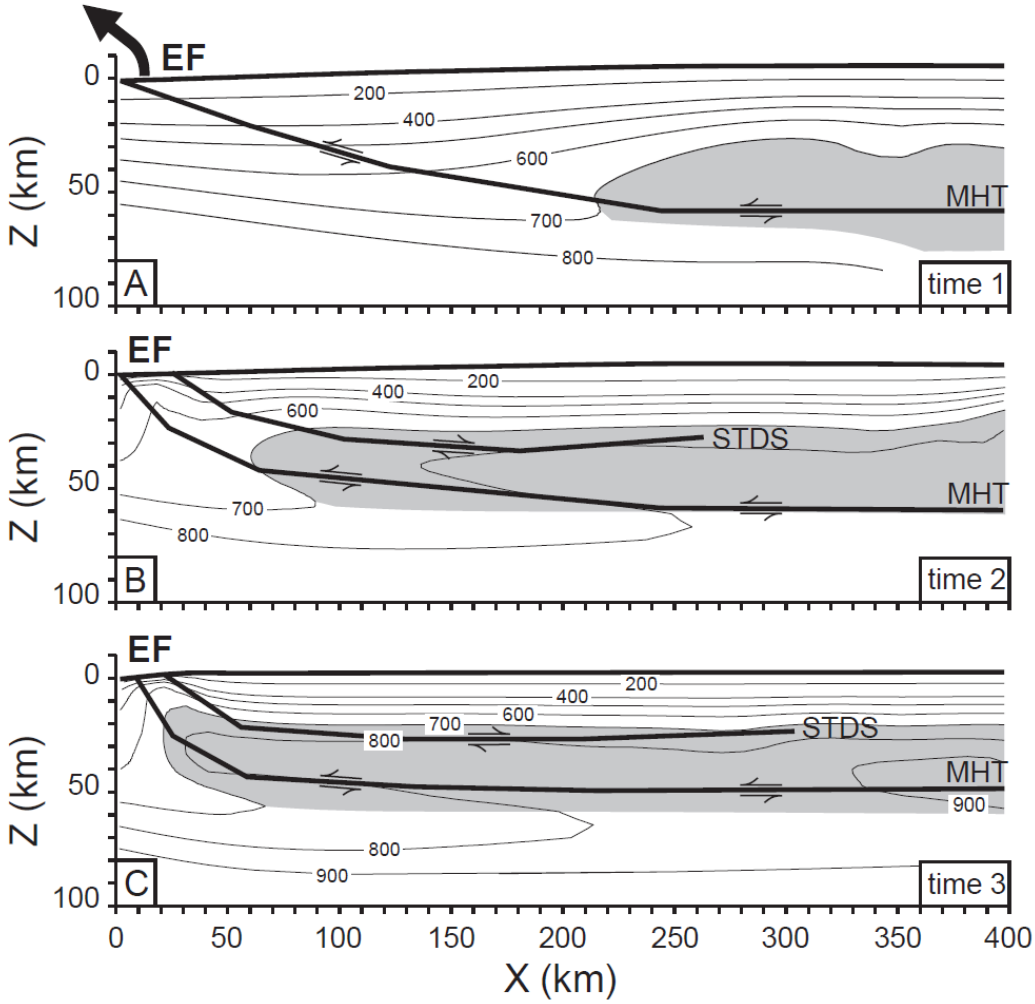

Figure 2.2: Channel Flow model of Himalayan development (from Kohn, 2008; based on Beaumont et al., 2004 and Jamieson et al., 2004). Partial melt channel (gray zone, ≥700°C) couples with an erosional front (EF) and propagates forward over time until hot, partially molten rocks are brought close to the surface before cooling begins.

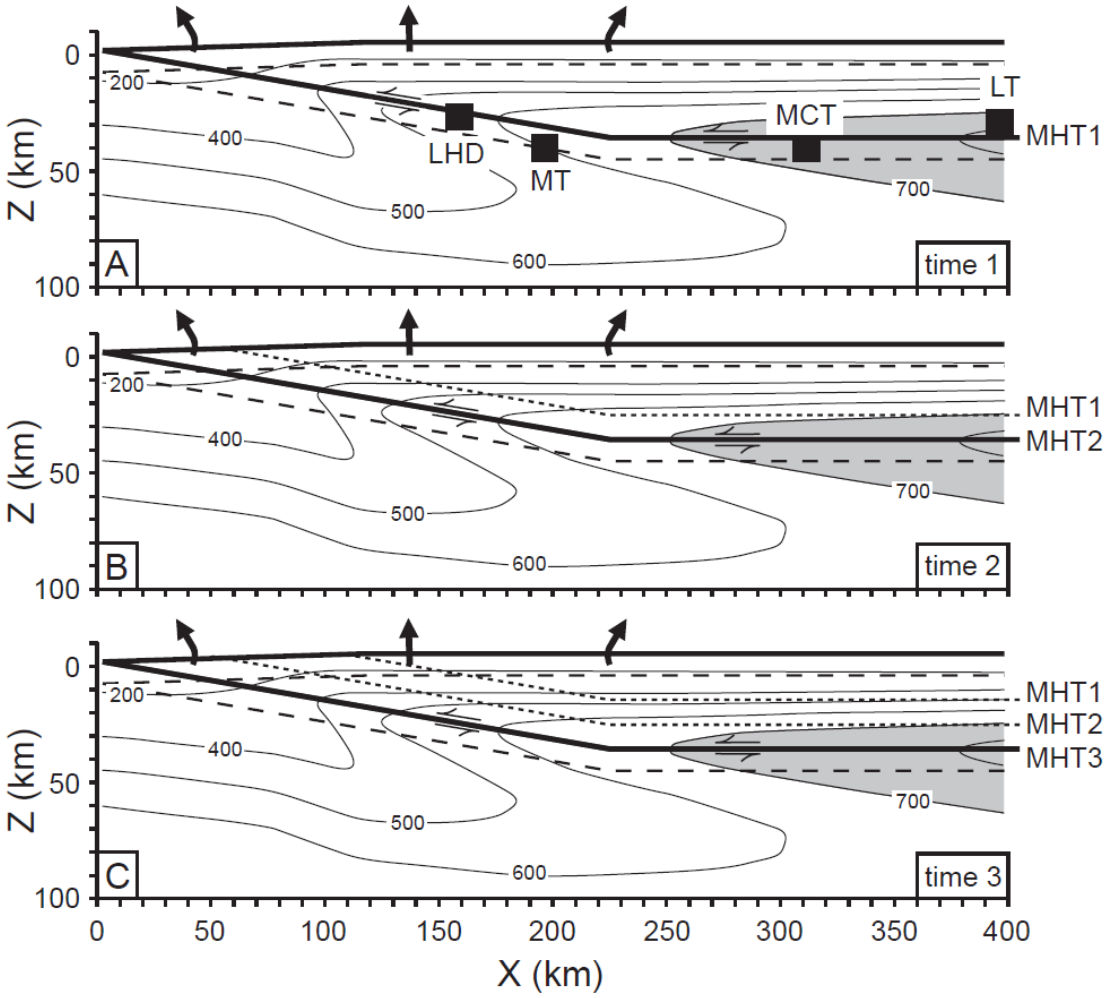

Figure 2.3: Figure 2.3. Critical wedge model of Himalayan development (from Kohn, 2008; based on Henry et al., 1997 and Bollinger et al., 2006). As erosion uniformly removes material from on top of the section, thrusts progressively underplate, creating a series of in-sequence thrusts over time. A partial melt zone exists, but remains far from the orogenic front.

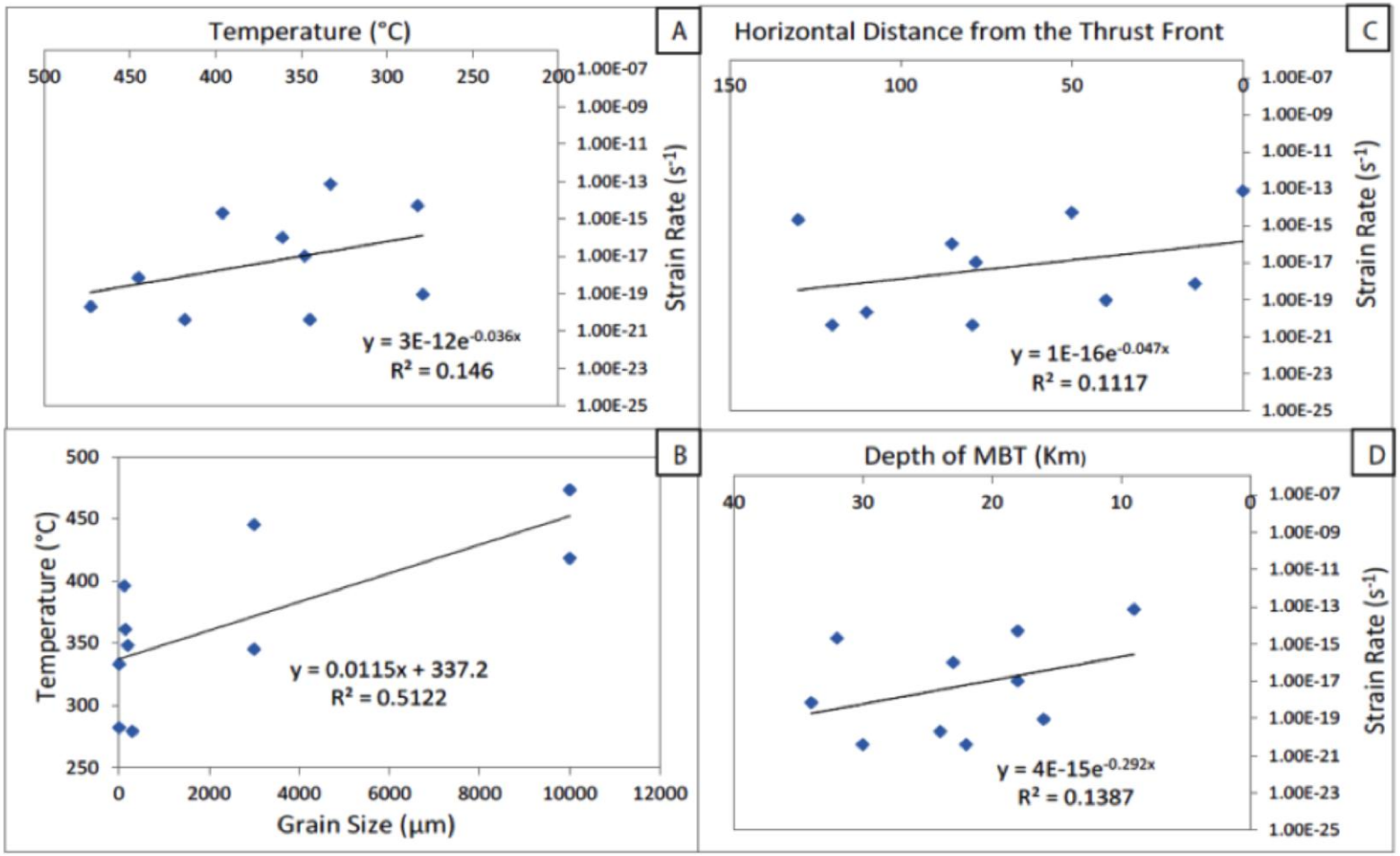

Figure 2.4: (A) Weak trend to higher strain rates at lower temperatures; (B) Weak trend to higher temperature in larger grains; (C) Weak trend to higher strain rates closer to the thrust front, and shallower in the crust (D).

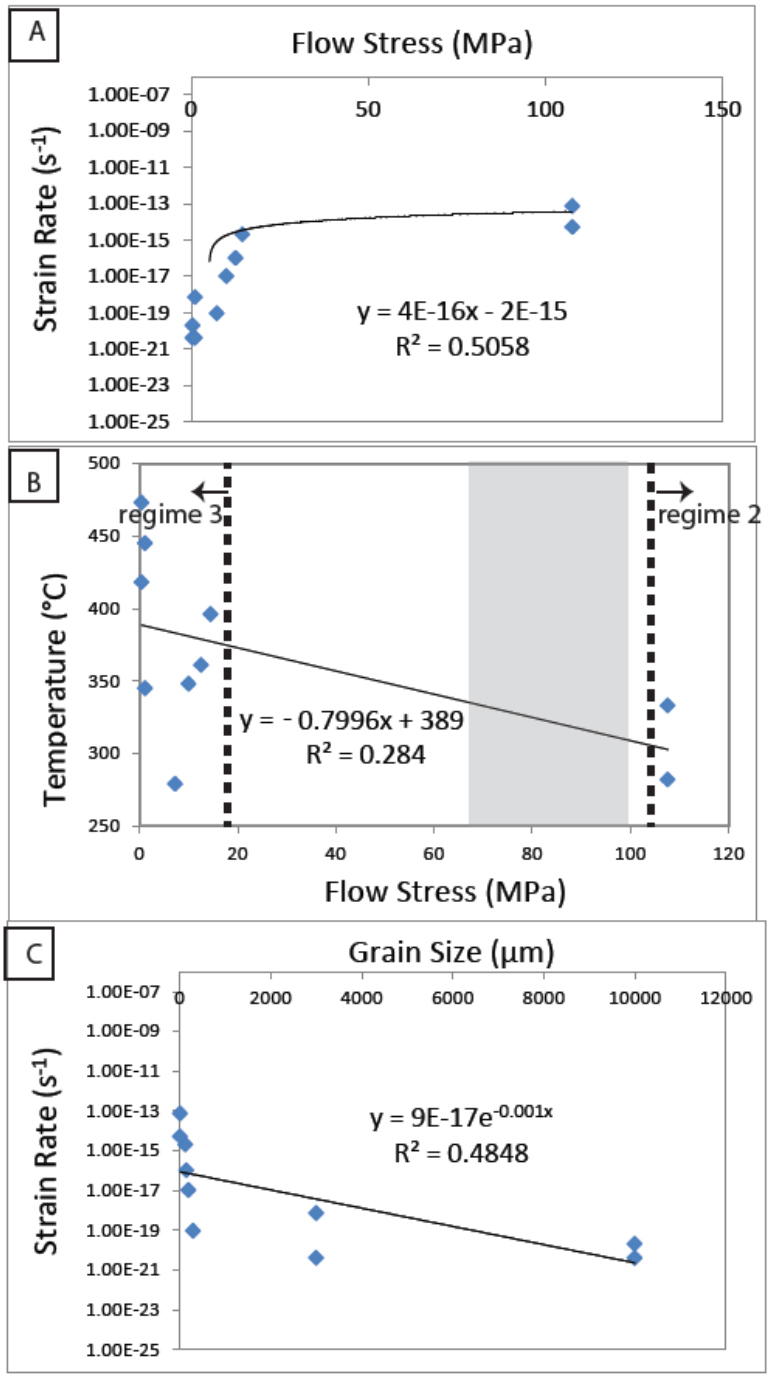

Figure 2.5: A) Increasing strain rate as a function of increasing flow stress; B) quartz grains record lower temperatures at higher flow stresses. Black dashed lines mark our best constraint on the transition between dislocation creep regimes 2 and 3. Gray zone is transition between dislocation creep regimes 2 and 3 as defined by Hirth et al. (2001), and it falls within the upper end of our constraints; and C) shows trend to higher strain rates in smaller grains.

Table 2.1: Flow stress and strain rate of rocks from the Scandinavian Caledonides in northern Norway and Sweden

Sample	Recrystallized Grain Size (μm)	σ (MPa) ± 1σ	T (°C)	Strain Rate (s^{-1})	± 2σ
SC10-26	200	10 ± .01	494	1.47E-15	1.57027E-16
SC10-29	3000	1 ± .10	445	6.41E-20	5.00041E-19
SC10-30	100	17 ± .01	456	4.41E-15	2.37067E-16
SC10-31	200	10 ± .01	486		
SC10-18	50	30 ± .01	420	1.25E-14	2.2008E-16
	200	10 ± .01	420	1.54E-16	9.66351E-18
SC10-21	125	14 ± .01	396	2.95E-16	1.14754E-17
SC10-25	50	30 ± .01	419	1.21E-14	2.12753E-16
	1000	3 ± .04	419	8.97E-19	5.9235E-19
SC10-03	200	10 ± .01	435	2.52E-16	1.77892E-17
	800	3 ± .03	435	3.09E-18	1.56911E-18
SC10-04	1000	3 ± .04	454	2.78E-18	2.05416E-18
	10000	0 ± .34	454	1.86E-21	1.29341E-19
SC10-06	10000	0 ± .34	418	5.80E-22	4.03972E-20
SC10-12	300	7 ± .01	469	1.99E-16	2.28791E-17
SC10-42	200	10 ± .01			
SC10-45	10000	0 ± .34	473	3.28E-21	2.23102E-19
SC10-32	1500	2 ± .05	379	5.87E-20	3.01918E-20
	200	10 ±.01	379	3.52E-17	8.52249E-19
SC10-33	150	13 ± .01	361	4.32E-17	7.74018E-19
	500	5 ± .02	361	9.46E-19	7.7266E-20
SC10-34	1000	3 ± .04	371		
SC10-35bii	100	17 ± .01	367	1.99E-16	2.43198E-18
SC10-38	200	10 ± .01	378	3.39E-17	8.20261E-19
SC10-46	3000	1 ± .10	345	1.65E-21	2.49043E-21
	500	5 ± .02	345	4.88E-19	3.39029E-20
SC10-48	200	10 ± .01	348	1.01E-17	1.44623E-19
SC10-51	10	108 ± .01	282	6.11E-15	3.66079E-18
SC10-49	300	7 ± .01	279	1.07E-19	1.35399E-21
	15	78 ± .01	279	1.44E-15	1.19007E-18
SC10-55	10	108 ± .01	333	7.17E-14	2.92054E-17
	150	13 ± .01	333	1.32E-17	5.18766E-20

Table 2.2: Geologic setting of rocks from the Scandinavian Caledonides in northern Norway and Sweden

Sample	Group	Rock Type	Geologic Setting	Depth of MBT (km)
SC10-26	A	schist	Uppermost Allochthon: Calednoian Cover	34
SC10-29	A	quartz vein	Uppermost Allochthon: Calednoian Cover	34
SC10-30	A	schist	Uppermost Allochthon: Calednoian Cover	33
SC10-31	A	schist	Uppermost Allochthon: Calednoian Cover	32
SC10-18	B	schist	Caledonian Cover	32
SC10-21	B	quartzite	Caledonian Cover	32
SC10-25	B	quartz vein	Caledonian Cover	31
SC10-03	C	mylonite	Parauatochthon/Autochthon: PreCambrian Crystalline rocks	30
SC10-04	C	quartz vein	Parauatochthon/Autochthon: PreCambrian Crystalline rocks	30
SC10-06	C	quartz vein	Parauatochthon/Autochthon: PreCambrian Crystalline rocks	30
SC10-12	C	mylonite	Parauatochthon/Autochthon: PreCambrian Crystalline rocks	28
SC10-42	D	mylonite/ quartzite	Parauatochthon/Autochthon: PreCambrian Crystalline rocks	24
SC10-45	E	quartz vein	Upper Allochthon: Caledonian Cover	24
SC10-32	F	mylonite	Parauatochthon/Autochthon: PreCambrian Crystalline rocks	24
SC10-33	F	mylonite	Parauatochthon/Autochthon: PreCambrian Crystalline rocks	23
SC10-34	F	quartz vein	Parauatochthon/Autochthon: PreCambrian Crystalline rocks	23
SC10-35bii	F	mylonite	Parauatochthon/Autochthon: PreCambrian Crystalline rocks	23
SC10-38	F	schist	Parauatochthon/Autochthon: PreCambrian Crystalline rocks	22
SC10-46	G	quartz vein	Parauatochthon/Autochthon: PreCambrian Crystalline rocks	22

SC10-48	H	mylonite	Parauatochthon/Autochthon: PreCambrian Crystalline rocks	18
SC10-51	I	ultramylonite	Middle Allochthon: Middle Proterozoic and older	18
SC10-49	J	quartzite ultramylonite	Caledonian Cover	16
SC10-55	K	quartzite ultramylonite	Parautochthon/Autochthon	9

References

Andersen, T.B., Jamtveit, B., Dewey, J.F., and Swenson, E., 1991, Subduction and eduction o continental crust: Major mechanisms during continent-continent collision and orogenic extensional collapse, a model based on the southern Norwegian Caledonides: Terra Nova, v. 3, p. 303-310.

Andresen, A., Rehnstrom, E.F., and Holte, M., 2007, Evidence for simultaneous contraction and extension at different crustal levels during the Caledonian orogeny in NE Greenland: Journal of the Geological Society, v. 164, p. 869-880.

Beaumont, C., Jamieson, R.A., Nguyen, M.H., and Lee, B., 2001, Himalayan tectonics explained by extrusion of a low-viscosity crustal channel coupled to focused surface denudations: Nature, v. 414, p. 738-742, doi: 10.1038/414738a.

Beaumont, C., Jamieson, R.A., Nguyen, M.H., and Medvedev, S., 2004, Crustal channel flows: 1. Numerical models with applications to the tectonics of the Himalayan Tibetan Orogen: Journal of Geophysical Research, v. 109, B06406, doi: 10.1029/2003JB002809.

Bilham, R., Bendick, R., Wallace, K., 2003, Flexure of the Indian plate and intraplate earthquakes, Journal of Earth System Science, v. 112, no. 3, p. 315-329.

Bollinger, L., Henry, P., and Avouac, J.P., 2006, Mountain building in the Nepal Himalaya: Thermal and kinematic model: Earth and Planetary Science Letters, v. 244, p. 58-71, doi: 10.1016/j.epsl.2006.01.045.

Braathen, A., Nordgulen, O., Osmundsen, P., Andersen, T., Solli, A., and Roberts, D., 2000, Devonian, orogen-parallel, opposed extension in Central Norwegian Caledonides: Geology, v. 28, no. 7, p. 615-618.

Brown, L.D., Zhao, W., Anonymous, 2006, INDEPTH; probing the basement on the roof of the world; Geological Society of America, v. 38, no. 7, p. 272.

Brueckner, H.K., and van Roermund, H.L.M., 2004, Dunk Tectonics: A multiple subduction/eduction model for the evolution of the Scandinavian Caledonides: Tectonics, doi: 10.1029/2003TC001502.

Burnham, C.W., Holloway, J. R., and Davis, N. F., 1969, Special Paper, Geological Society of America, v. 132, no. 7.

Copeland, P., and Harrison, T.M., 1990, Episodic rapid uplift in the Himalaya revealed by 40Ar/39Ar, analysis of detrital K-feldspar and muscovite, Bengal fan: Geology, v. 18, p. 354-357.

Corrie, S.L., 2010, Geochemical and geochronological constraints on the tectonothermal history of the Central and Eastern Nepal Himalaya: BSU dissertation.

Dahlen, F.A., 1990, Critical taper model of fold-and-thrust belts and accretionary wedges: annual Review of Earth and Planetary Sciences, v. 18, p. 55-99, doi: 10.1146/annurev.ea.18.050190.000415.

Engvik, A.K., Tveten, E., Bingen, B., Viola, G., and Erambert, M, 2007, P-T-t evolution and textural evidence for decompression of Pan-African high-pressure granulites, Lurio Belt, north-eastern Mozambique: Journal of Metamorphic Geology, v. 25, no. 9, p. 935-952.

Fossen, H., 1992 The role of extensional tectonics in the Caledonides of South Norway: Journal of Structural Geology, v. 14 (in press).

Fossen, H., and Rykkelid, E., 1992, Postcollisional extension of the Caledonide orogeny in Scandinavia: Structural expressions and tectonic significance: Geology, v. 20, p. 737-740.

Fossen, H., 2000, Extensional tectonics in the Caledonides: Synorogenic or postorogenic?: Tectonics, v. 19, no. 2, p.213-224.

Fossen, H., 2010, Extensional tectonics in the North Atlantic Caledonides: A regional view: Geological Society Special Publication, v. 335, p. 767-793.

Gee, D.G., 1975, A tectonic model for the central part of the Scandinavian Caledonides: Journal of American Science, v. 275A, p. 468-515.

Gee, D.G., and Sturt, B.A., 1985, The Caledonide orogen –Scandinavia and related areas. Wiley, Chichester.

Gee, D.G., Lobkowicz, M., and Singh, S., 1994, Late Caledonian extension in the Scandinavian Caledonides—the Roragen Detachment revisited: Tectonophysics, v. 231, p. 139-155.

Gee, D.G., Fossen, H., Henriksen, N. and Higgins, A., 2008, From the early Paleozoic platforms of Baltica and Laurentia to the Caledonide Orogen of Scandinavia and Greenland. Episodes 31, 44-51.

Gee, D.G., Juhlin, C, Pascal, C, and Robinson, P., 2010, Collisional Orogeny in the Scandinavian Caledonides (COSC): GFF, v. 132, p. 29-44.

Griffin, W.L., and Brueckner, H.K., 1980, Caledonian Sm-Nd ages and a crustal origin for Norwegian eclogites, Nature, v. 285, p. 319-321.

Hacker, B.R., 2007, Ascent of the ultrahigh-pressure Western Gneiss Region, Norway: Geological Society of America Special Paper, v. 419, p. 171-184, doi: 10.1130/2006.2419(09).

Hacker, B.R., Andersen, T.B., Root, D.B., Mehl, L., Mattinson, J.M., and Wooden, J.L., 2003, Exhumation of high-pressure rocks beneath the Solund Basin, Western Gneiss Region of Norway: Journal of Metamorphic Geology, v. 21, p. 613-621, doi: 10.1046/j.1525-1314.2003.00468.x.

Hacker, B.R., Andersen, T.B., Johnston, S., Kylander-Clark, A.R.C., and Peterman, E.M., 2010, High-temperature deformation during continental-margin subduction and exhumation: The ultrahigh-pressure Western Gneiss Region of Norway: Tectonophysics, v. 480, no. 1-4, p. 149-171.

Harrison, T.M., Grove, M., Lovera, O.M., and Catlos, E.J., 1998, A model for the origin of Himalayan anatexis and inverted metamorphism: Journal of Geophysical Research, v. 103, p.27, 017-27,032, doi: 10.1029/98JB02468.

Henry, P., Le Pichon, X., and Goffe, B., 1996, Kinematic, thermal and petrological model of the Himalayas: constraints related to metamorphism within the underthrust Indian crust and topographic elevation: Tectonophysics, v. 273, p. 31-56.

Henry, P., Le Pichon, X., and Goffe, B., 1997, Kinematic, thermal and petrological model of the Himalayas: Constraints related to metamorphism within the underthrust Indian crust and topographic evolution: Tectonophysics, v. 273, p. 31-56, doi: 10.1016/S00401951(96)00287-9.

Hirth, G., and Tullis, J., 1992, Dislocation creep regimes in quartz aggregates: Journal of Structural Geology, v. 14, issue 2, p. 145-159.

Hirth, G., Teyssier, C., and Dunlap, J., 2001, An evaluation of quartzite flow laws based on comparisons between experimentally and naturally deformed rocks: International Journal of Earth Sciences, v. 90, p. 77-87, doi: 10.1007/s005310000152.

Hodges, K.V., Bartley, J.M., and Burchfiel, B.C., 1982, Structural evolution of an A-type subduction zone, Lofoten, Tectonics, I, p. 441-462.

Huerta, A.D., Royden, L.H., and Hodges, K.V., 1998, The thermal structure of collisional orogens as a response to accretion, erosion, and radiogenic heating: Journal of Geophysical Research, v. 103, p. 15,287-15,302, doi: 10.1029/98JB00593.

Huerta, A.D., Royden, L.H., and Hodges, K.V., 1999, The effects of accretion, erosion, and radiogenic heat on the metamorphic evolution of collisional orogens: Journal of Metamorphic Geology, v. 17, p. 349-366.

Jamieson, R.A., Beaumont, C., Nguyen, M.H., and Lee, B., 2002, Interaction of metamorphism, deformation and exhumation in large convergent orogens: Journal of Metamorphic Geology, v. 20, p. 9-24, doi: 10.1046/j.0263-4929.2001.00357.x.

Jamieson, R.A., Beaumont, C., Medvedev, S., and Nguyen, M.H., 2004, Crustal channel flows: 2. Numerical models with implications for metamorphism in the Himalayan-Tibetan orogen: Journal of Geophysical Research, v. 109, B06406, doi: 10.1029/2003JB002811.

Kohlstedt, D.L., and Weathers M.S., 1980, Deformation-induced microstructures, paleopiezometers, and differential stresses in deeply eroded fault zones: Journal of Geophysical Research, v. 85, no. B11, p. 6269-6285, doi: 10.1029/JB085iB11p06269.

Kohn, M.J., 2004, Oscillatory- and sector-zoned garnets record cyclic (?) rapid thrusting in central Nepal: Geochemistry Geophysics Geosystems, v. 5, Q12014, doi: 10.1029/2004GC000737.

Kohn, M.J., 2008, P-T-t data from central Nepal support critical taper and repudiate large-scale channel flow of the Greater Himalayan Sequence: GSA Bulletin, v. 120, no. 3/4, p. 259-273, doi: 10.1130/B26252.1.

Kohn M.J., and Northrup C.J., 2009, Taking mylonites' temperature: Geology, v. 37, no. 1, p. 47-50, doi: 10.1130/G25081A.1.

Northrup, C.J., 1996, Structural expressions and tectonic implications of general noncoaxial flow in the midcrust of a collisional orogeny: the northern Scandinavian Caledonides: tectonics, v. 15, no. 2, p. 490-505.

Northrup, C.J., 1997, Timing structural assembly, metamorphism, and cooling of Caledonian nappes in the Ofoten-Efjorden area, North Norway: Tectonic insights from U-Pb and 40Ar/39Ar Geochronology: Chicago Journals, v. 105, no. 5, p. 565-582.

Norton, M.G., 1986, Late Caledonide extension in Western Norway: A response to extreme crustal thickening: Tectonics, v. 5, no. 2, p. 195-204.

Ord, A., and Christie, J. M., 1984, Flow stresses from microstructures in mylonitic quartzites of the Moine thrust zone, Assynt area, Scotland: Journal of Structural Geology, v. 6,no. 6, p. 639-654.

Pecher, A., 1989, The metamorphism in the central Himalay: Journal of Metamorphic Geology, v. 7, p. 31-41.

Platt, J.P., 1986, Dynamics of orogenic wedges and the uplift of high-pressure metamorphic rocks: geological Society of America Bulletin, v. 97, p. 1037-1053.

Ramberg, H., 1977, Some remarks on the mechanism of nappe movement: Geol. Foren, Stockholm Forh, v. 99, p. 110-117.

Ramberg, H., 1981, The role of gravity in orogenic belts, in thrust and Nappe Tectonics: Special Publication Geological Society, London, v. 9, p. 125-140.

Roberts, D., and Gee, D.G., 1985, An introduction to the structure of the Scandinavian Caledonides, in the Caledonide Orogen –Scandinavia and related areas: p. 55-68.

Roberts, D., 2003, The Scandinavian Caledonides: Event chronology, palaeogeographic settings and likely modern analogues: Tectonophysics, v. 365, p. 283-299, doi: 10.1016/S0040-1951(03)00026-X.

Roddick, J.C., 1987, Generalized numerical error analysis with applications to geochronology and thermodynamics: Geochimica et cosmochimica, Acta, v. 51, p. 2129-2135.

Royden, L.H., 1993, The steady-state thermal structure of eroding orogenic belts and accretionary prisms: Journal of Geophysical Research, B, Solid Earth and Planets, v. 98, p. 4487-4507.

Sanderson, D. J., 1982, Models of strain variation in nappes and thrust sheets; a review: Tectonophysics, v. 88, no. 3-4, p. 201-233.

Stephens, M.B., and Gee, D.B., 1989, Terranes and polyphase accretionary history in the Scandinavian Caledonides: in Terranes in the Circum-Atlantic Paleozoic Orogens, GSA, v. 230 p. 17-30.

Stipp, M., and Tullis J., 2003, The recrystallized grain size piezometer for quartz: Geophysical Research Letters, v. 30, p. 2088, doi: 10.1029/2003GL018444.

Stipp, M., Tullis, J., Scherwath, M., and Behrmann J.H., 2010, A new perspective on paleopiezometry: Dynamically recrystallized grain size distributions indicate mechanism changes: Geology, v. 38, no. 8, p. 759-762d doi: 10.1130/F31162.1.

Terry, M.P., and Robinson, P., 2003, Evolution of amphibolite-facies structural features and boundary conditions for deformation during exhumation of high-and ultra high-pressure rocks, Nordoyane, Western Gneiss Region, Norway: Tectonics, v. 22, p. 1036, doi: 10.1029/2001TC001349.

Terry, M.P., and Robinson, P., 2004, Geometry of eclogite-facies structural features: Implications for production and exhumation of ultrahigh-pressure and high pressure rocks, Western Gneiss Region, Norway: Tectonics, v. 23, TC2001, doi: 10.1029/2002TC001401.

Tucker, R.D., Krogh, T.E., and Råheim, A., 1990, Proterozoic evolution and age-province boundaries in the central part of the Western Gneiss Region, Norway: Results of U-Pb dating of accessory minerals from Trondheimsfjord to Geiranger: Geological Association of Canada Special Paper, v. 38, p. 149-173.

Tullis, J., and Yund, R.A., 1977, Experimental deformation of dry westerly granite: Journal of Geophysical Research, AGU.

Zeitler, P.K., Meltzer, A.S., Koons, P.O., Craw, D., Hallet, B., Chamberlain, C.P., Kidd, W.S.F., Park, S.K., Seeber, L., Bishop, M., and Shroder, J., 2001 Erosion, Himalayan geodynamics, and the geomorphology of metamorphism: GSA Today, v. 11, no. 1, p.4-9, doi: 10.1130/10525173(2001)011<0004:EHG-ATG>2.0.CO;2.

APPENDIX

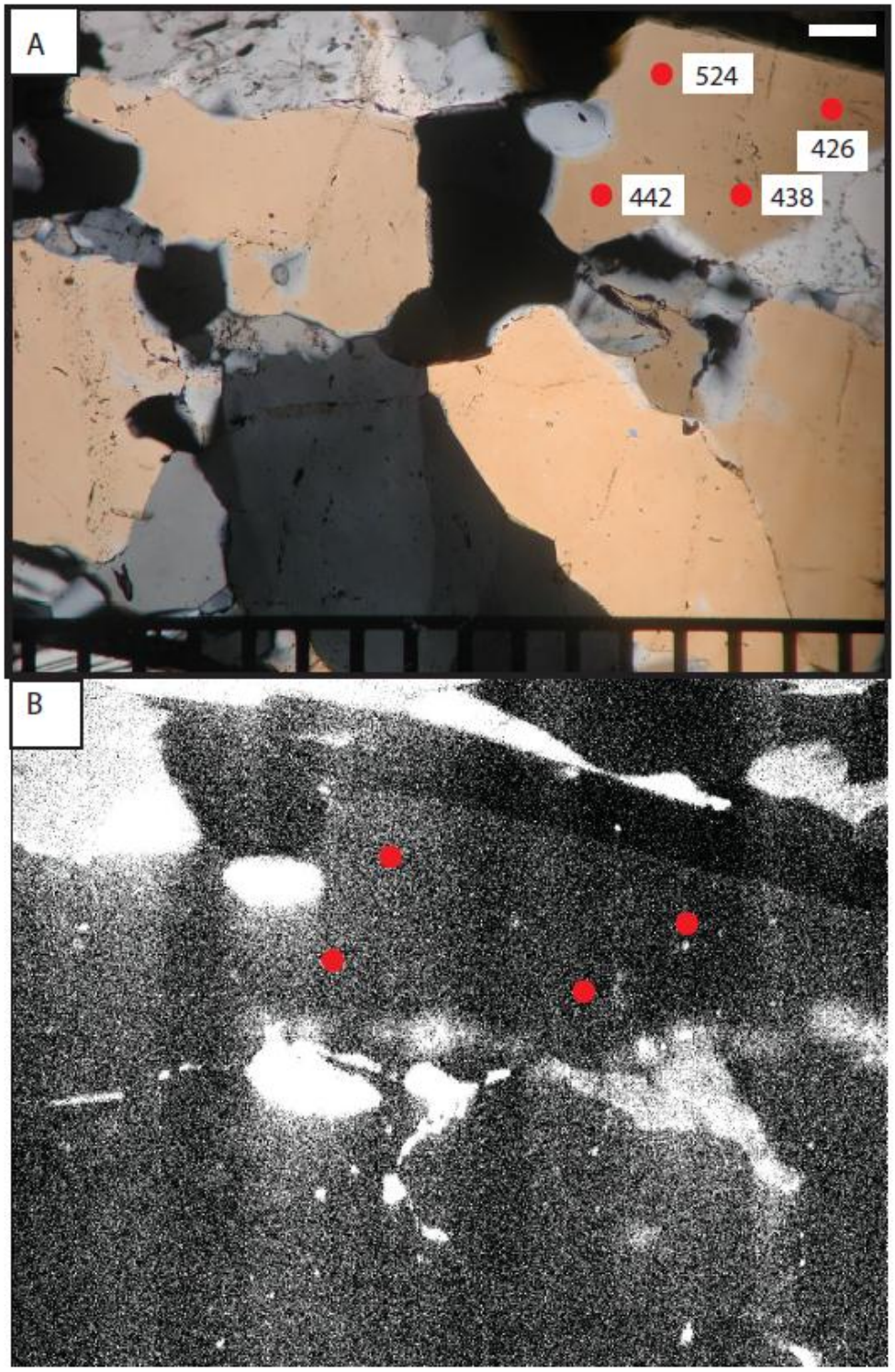

Figure A.1: A) Photomicrograph and B) CL image of sample SC10- 03. Temperatures are in degrees Celsius. Scale bar is 100 microns. Dominant dynamic recrystallization mechanism operative in quartz is GBM.

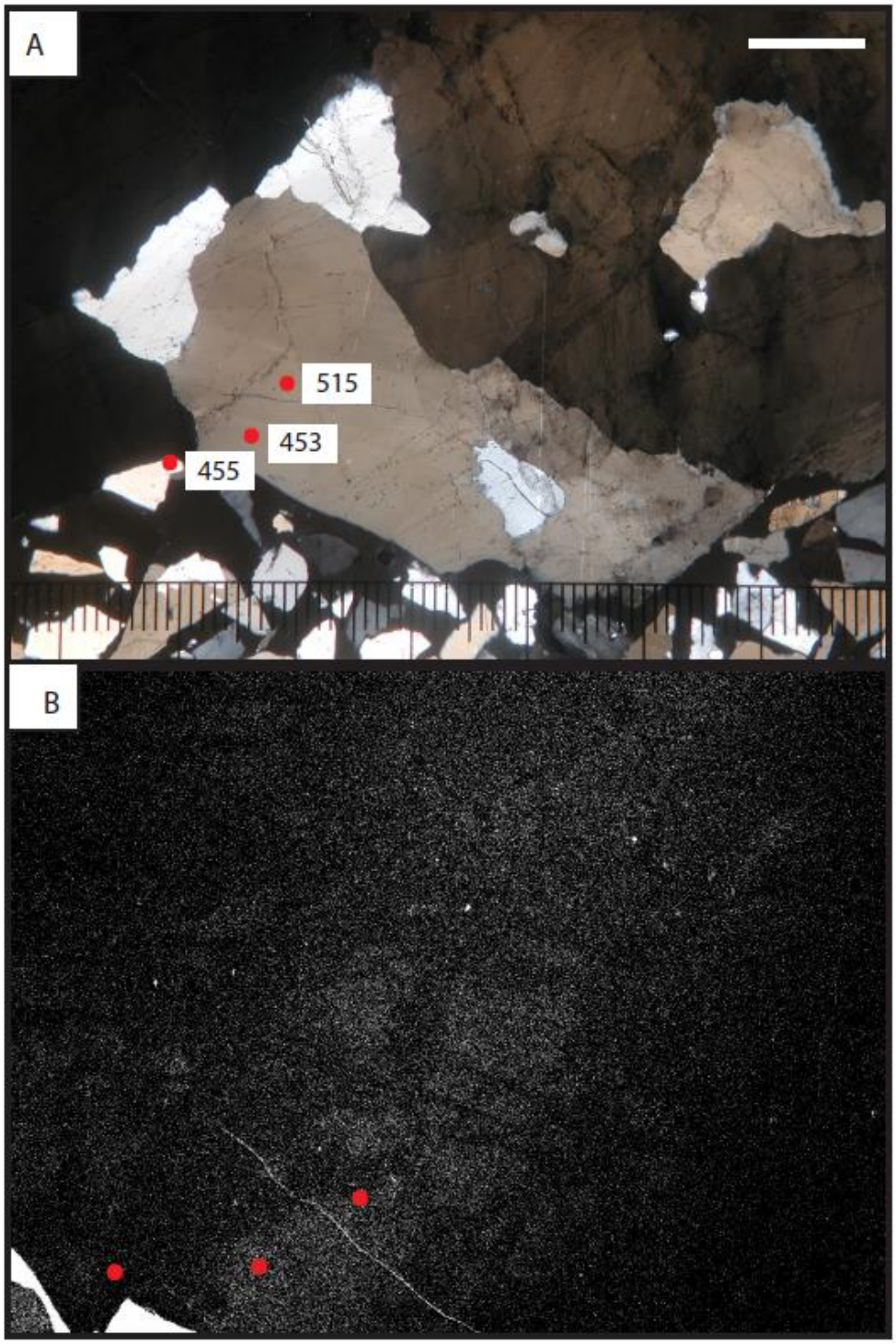

Figure A.2: A) Photomicrograph and B) CL image of sample SC10-04. Temperatures are in degrees Celsius. Scale bar is 1mm. Dominant dynamic recrystallization mechanism operative in quartz is GBM.

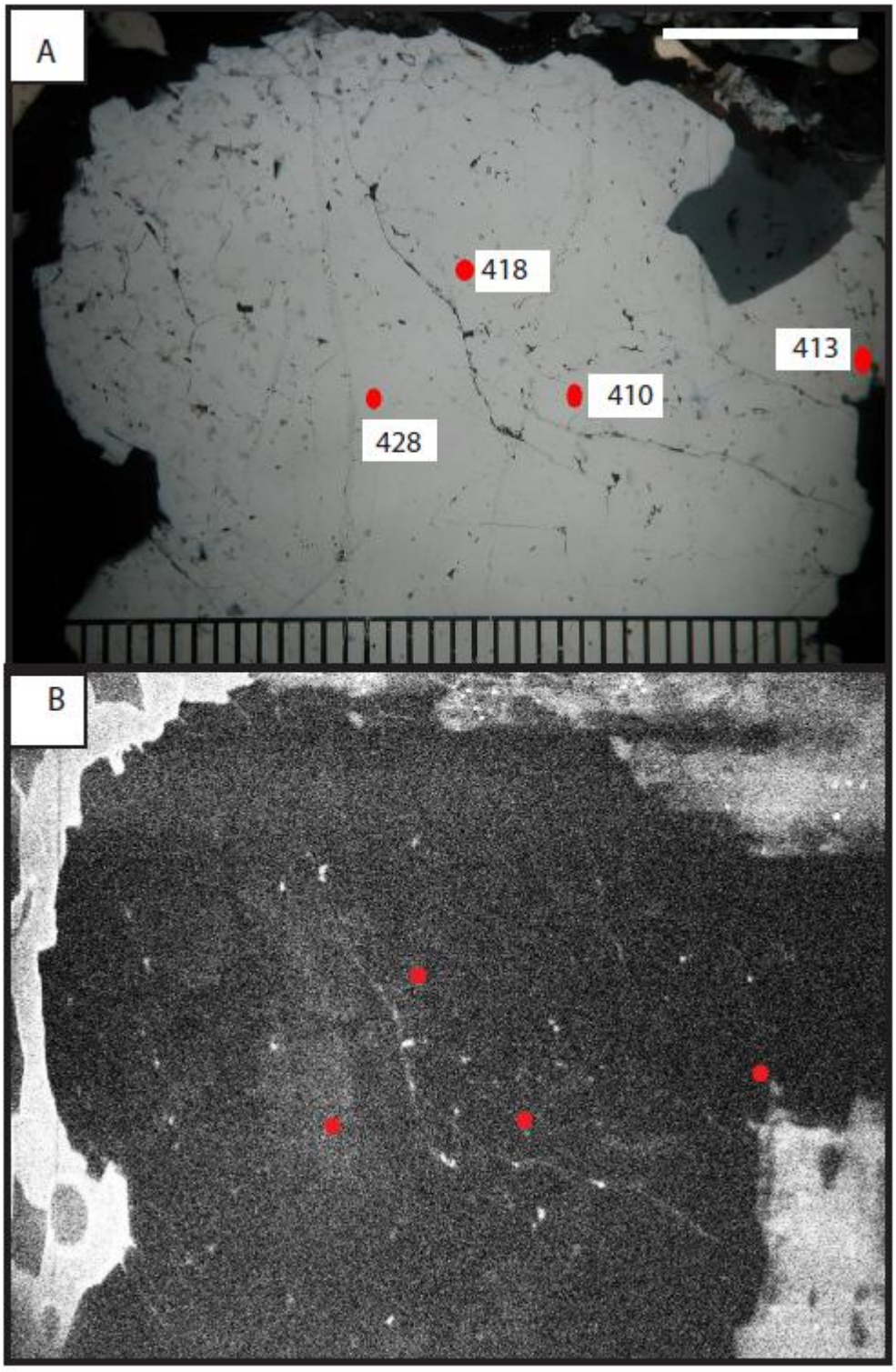

Figure A.3: A) Photomicrograph and B) CL image of sample SC10-06. Temperatures are in degrees Celsius. Scale bar is 1mm. Dominant dynamic recrystallization mechanism operative in quartz is GBM.

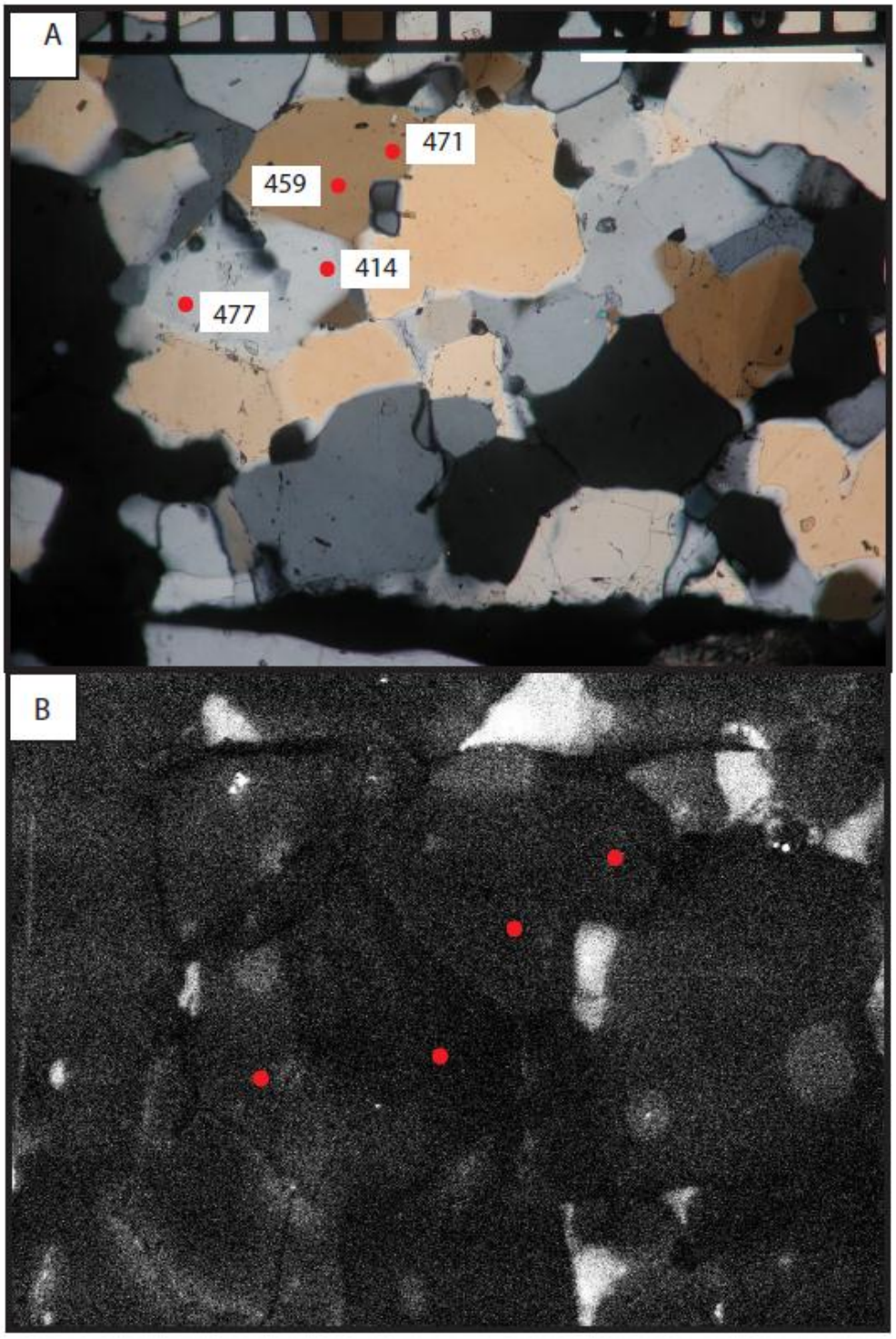

Figure A.4: A) Photomicrograph and B) CL image of sample SC10-12. Temperatures are in degrees Celsius. Scale bar is 500 microns. Dominant dynamic recrystallization mechanism operative in quartz is GBM.

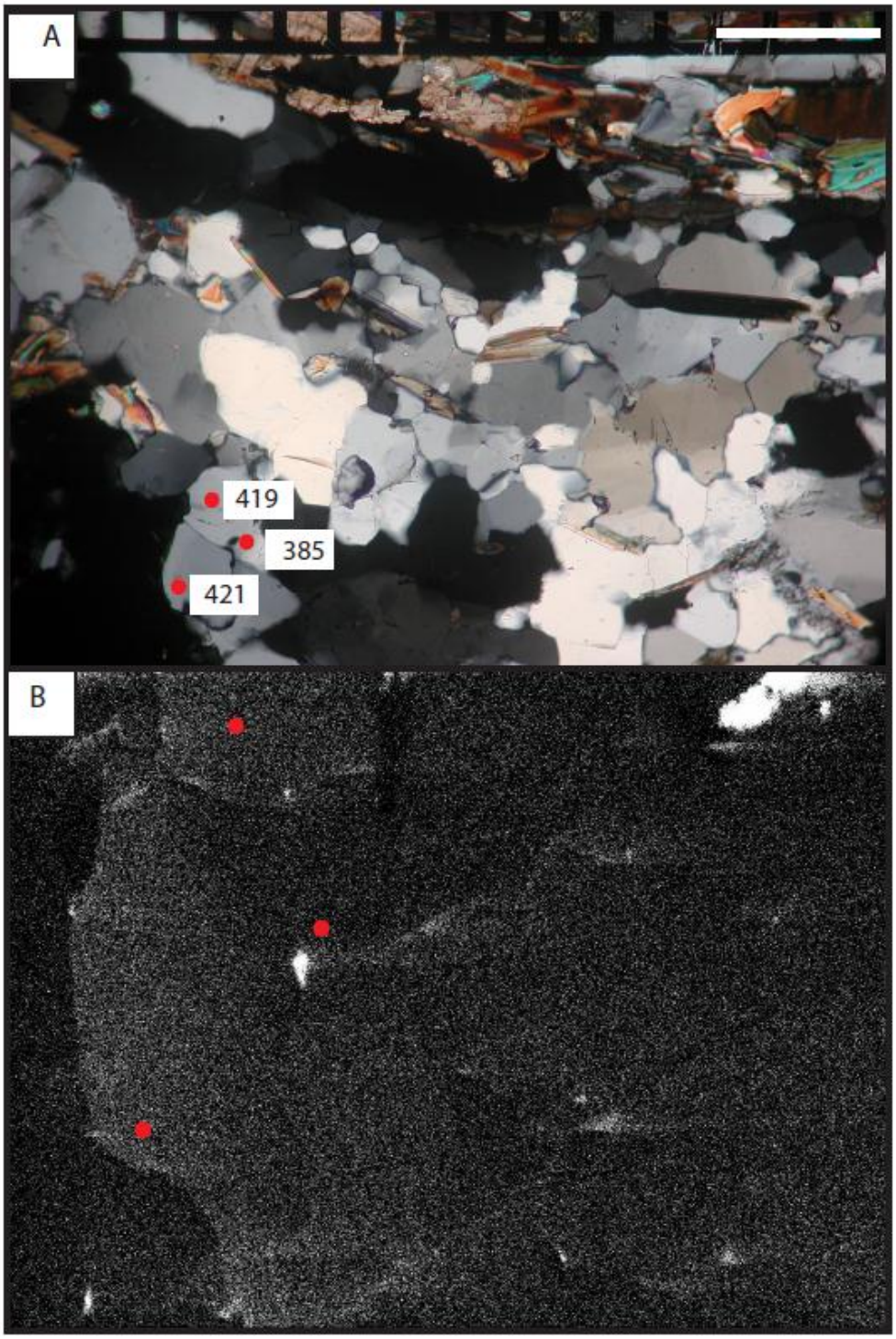

Figure A.5: A) Photomicrograph and B) CL image of sample SC10-18. Temperatures are in degrees Celsius. Scale bar is 300 microns. Dominant dynamic recrystallization mechanism operative in quartz is SR.

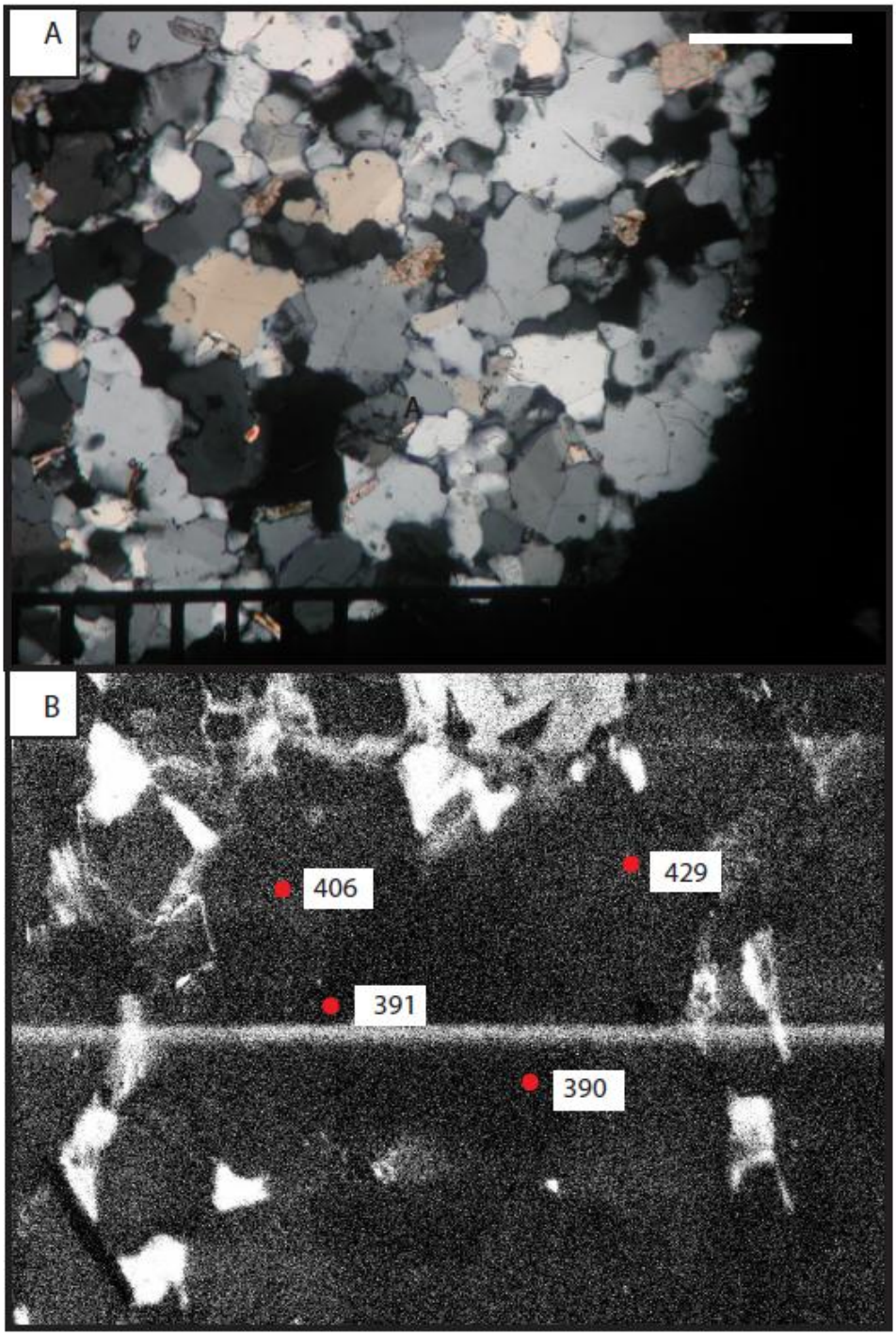

Figure A.6: A) Photomicrograph and B) CL image of sample SC10-21. Temperatures are in degrees Celsius. Scale bar is 300 microns. Dominant dynamic recrystallization mechanism operative in quartz is SR.

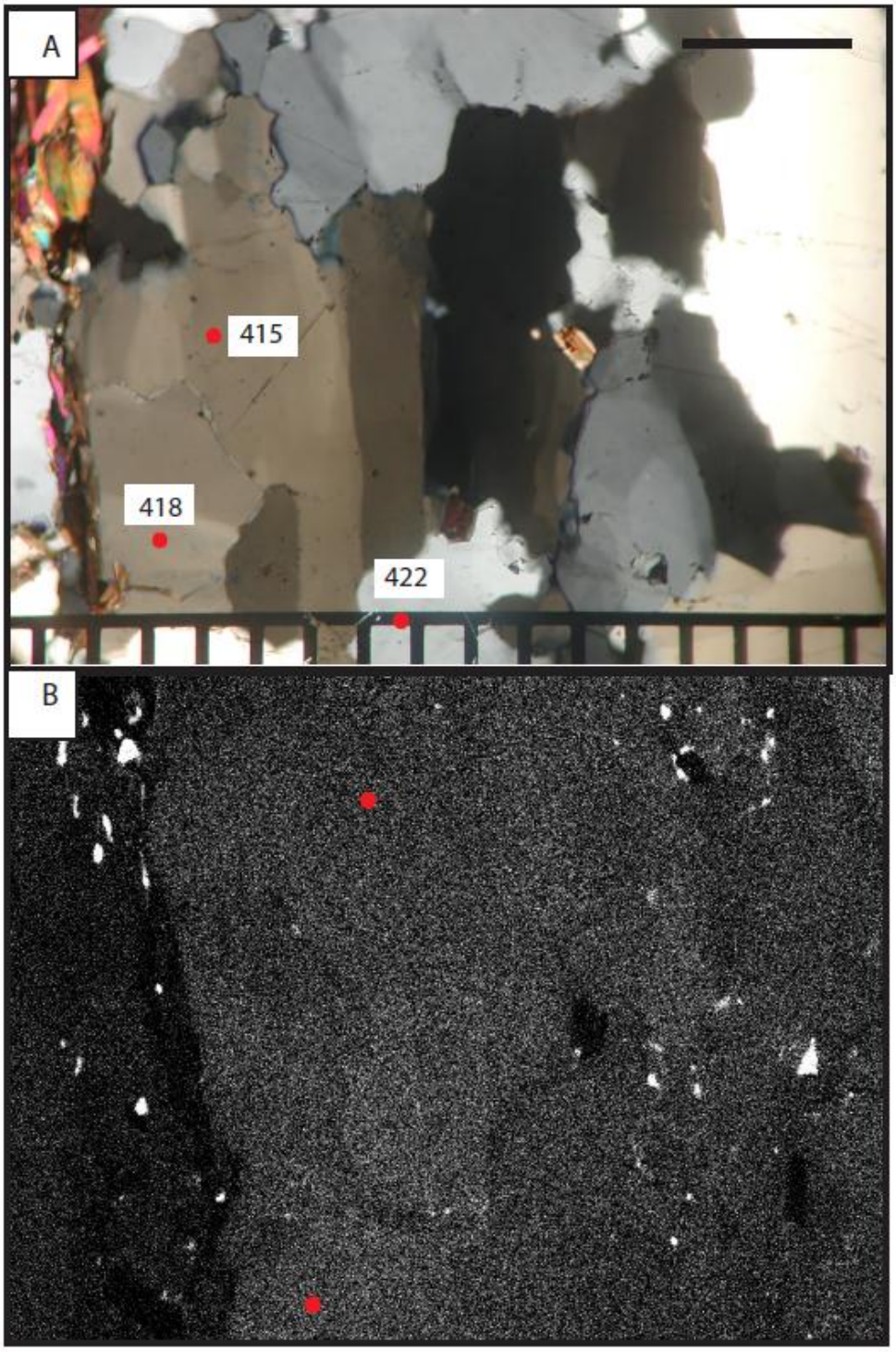

Figure A.7: A) Photomicrograph and B) CL image of sample SC10-25. Temperatures are in degrees Celsius. Scale bar is 300 microns. Dominant dynamic recrystallization mechanism operative in quartz is SR.

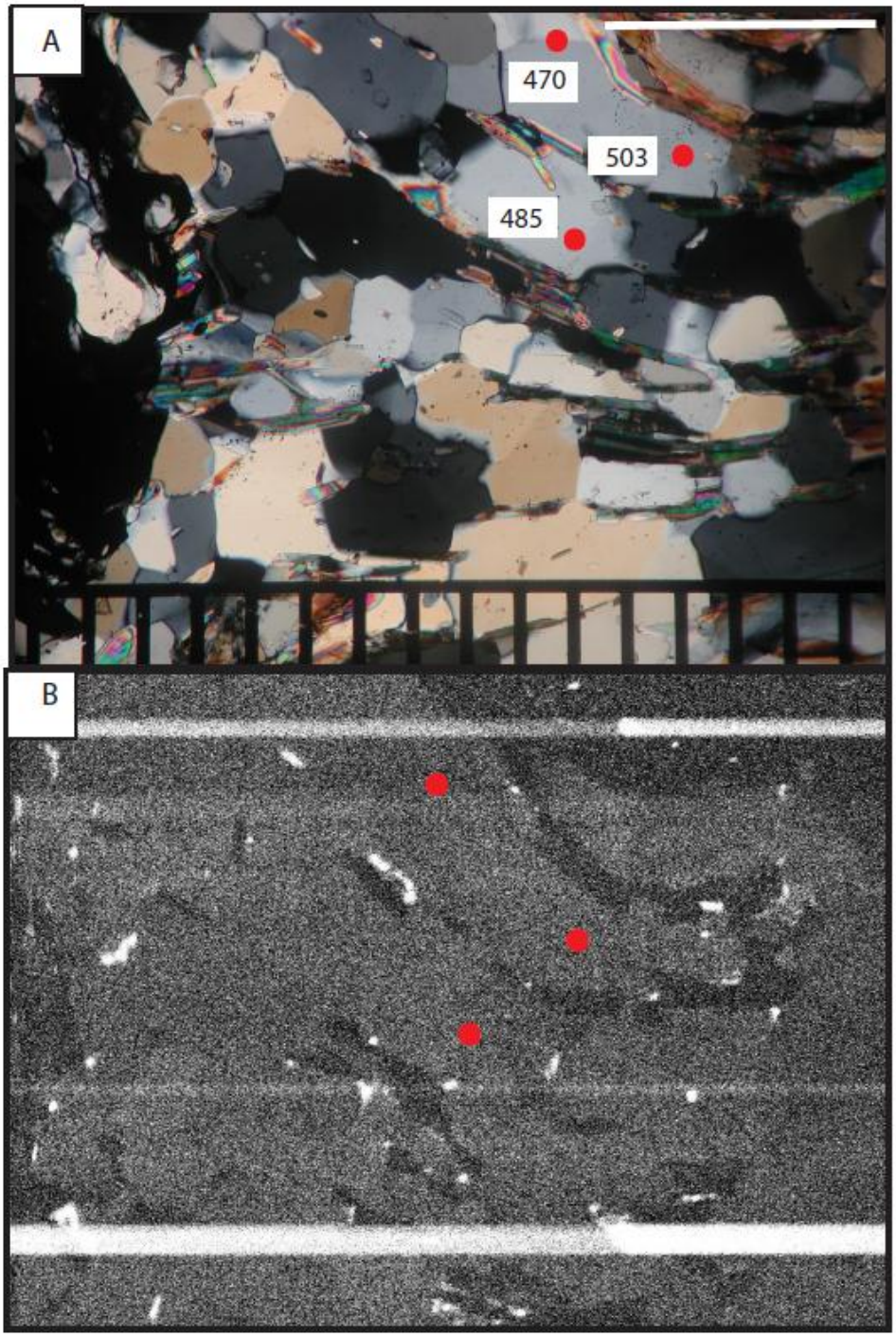

Figure A.8: A) Photomicrograph and B) CL image of sample SC10-26. Temperatures are in degrees Celsius. Scale bar is 500 microns. Dominant dynamic recrystallization mechanism operative in quartz is GBM.

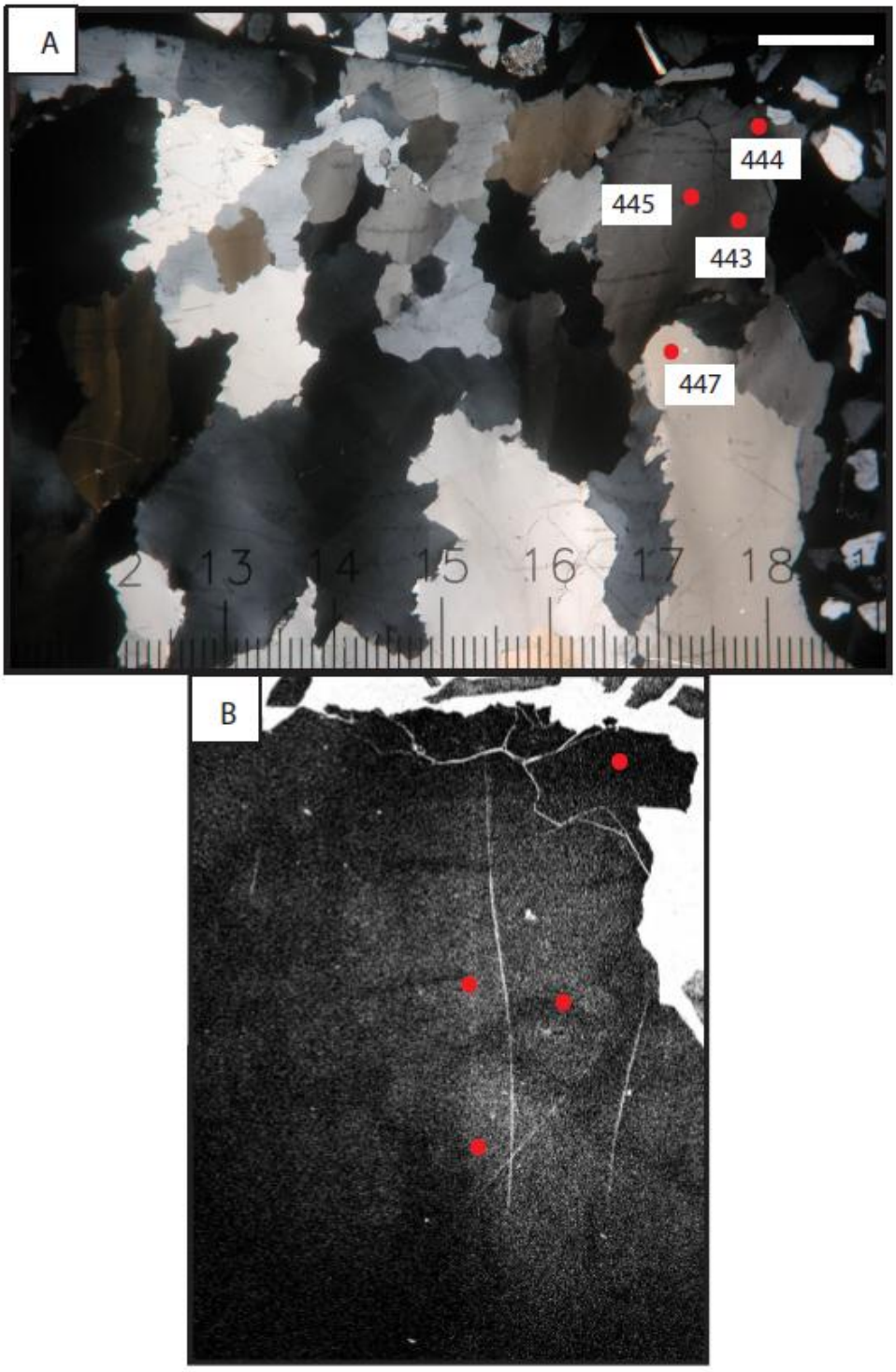

Figure A.9: A) Photomicrograph and B) CL image of sample SC10-29. Temperatures are in degrees Celsius. Scale bar is 1 mm. Dominant dynamic recrystallization mechanism operative in quartz is SR.

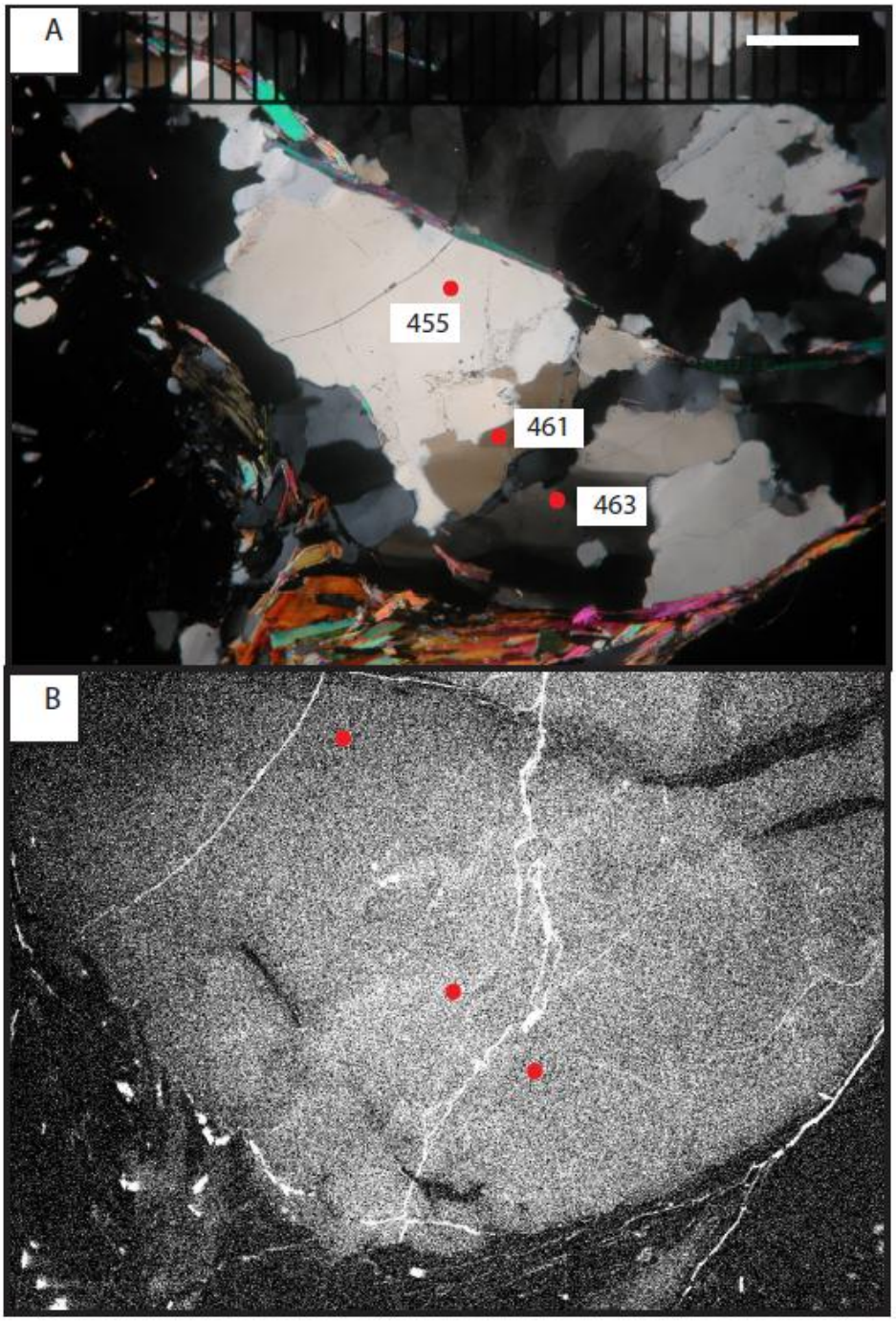

Figure A.10: A) Photomicrograph and B) CL image of sample SC10-30.1. Temperatures are in degrees Celsius. Scale bar is 500 microns. Dominant dynamic recrystallization mechanism operative in quartz is SR.

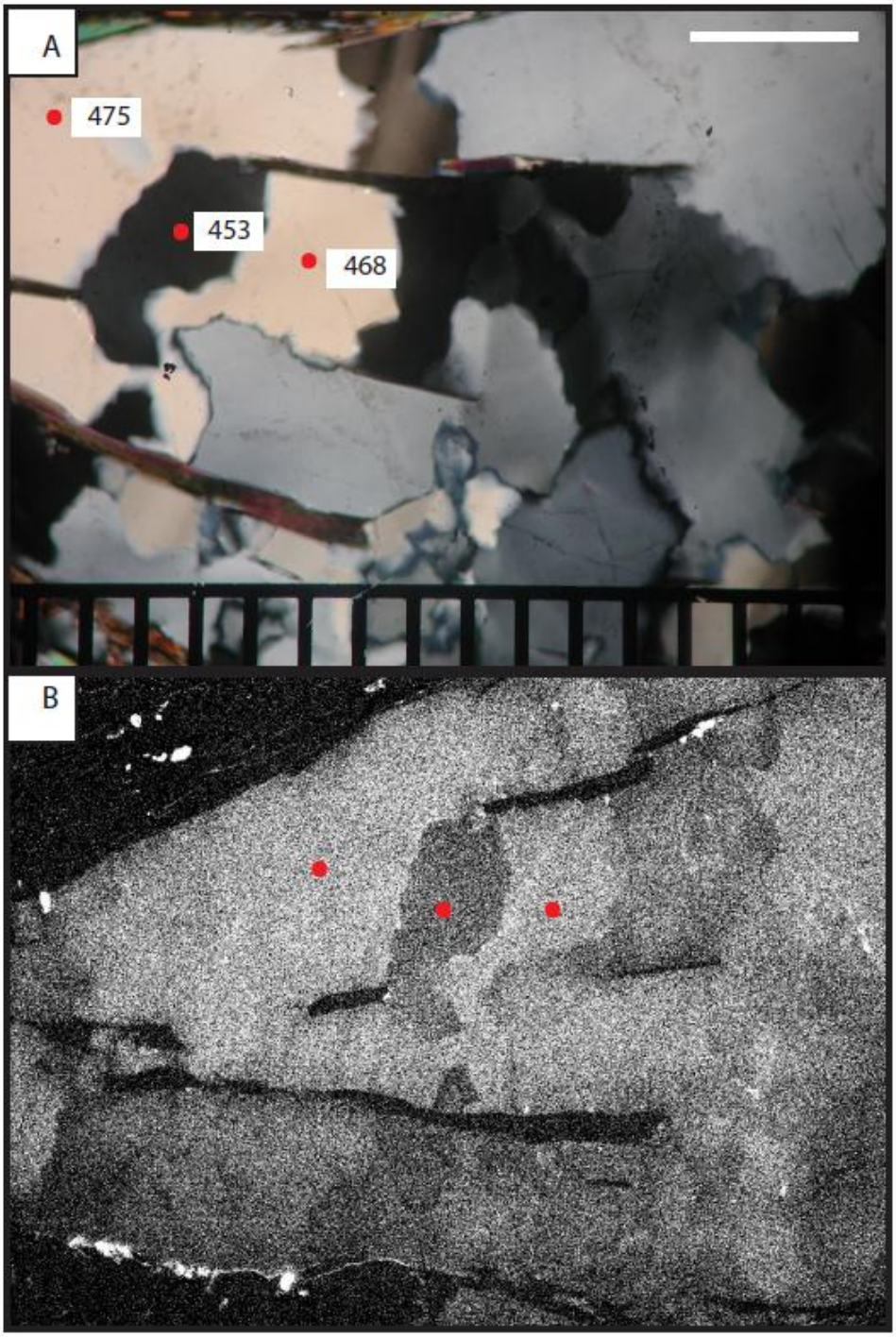

Figure A.11: A) Photomicrograph and B) CL image of sample SC10-30.2. Temperatures are in degrees Celsius. Scale bar is 300 microns. Dominant dynamic recrystallization mechanism operative in quartz is SR.

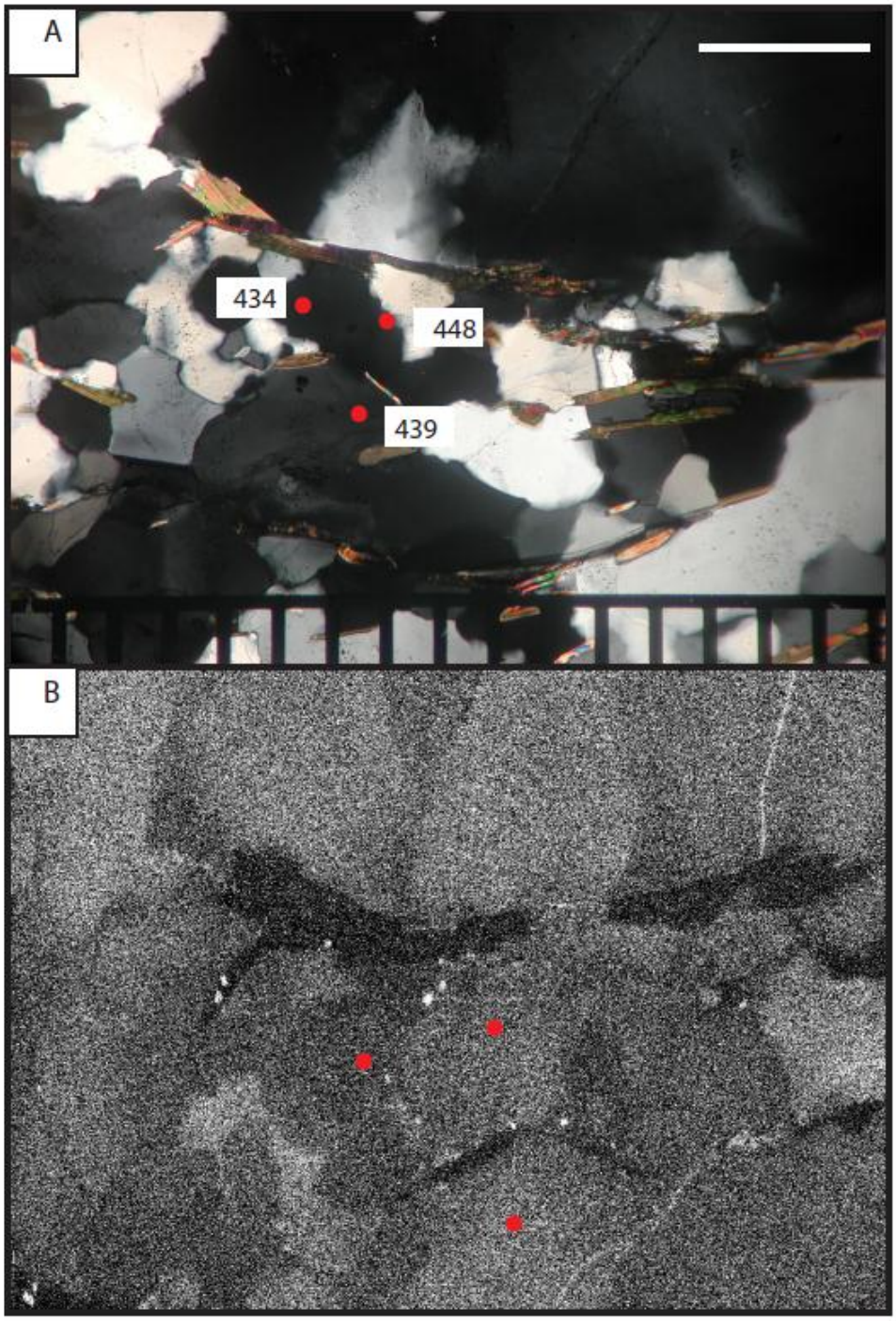

Figure A.12: A) Photomicrograph and B) CL image of sample SC10-30.3. Temperatures are in degrees Celsius. Scale bar is 300 microns. Dominant dynamic recrystallization mechanism operative in quartz is SR.

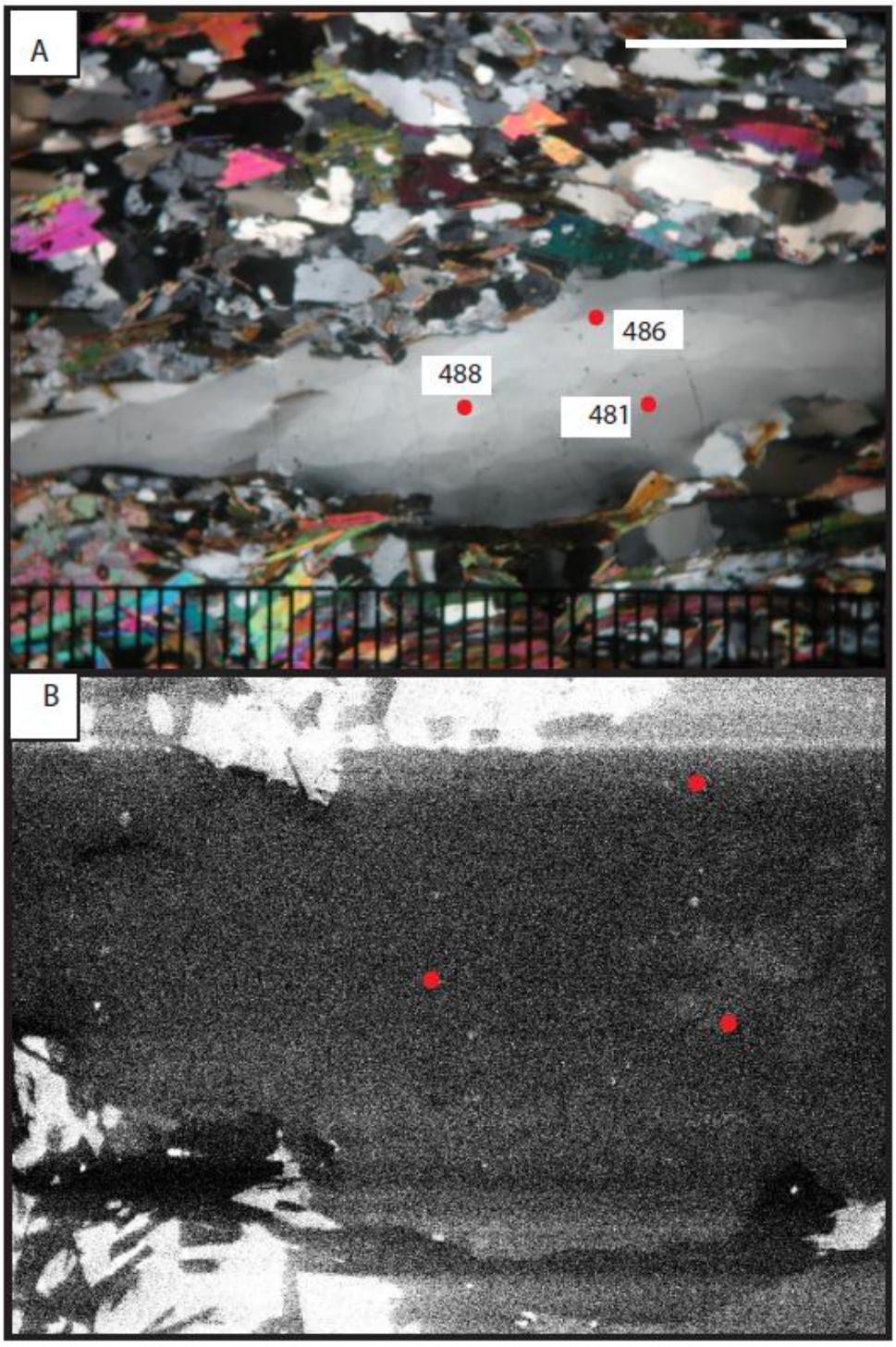

Figure A.13: A) Photomicrograph and B) CL image of sample SC10-31. Temperatures are in degrees Celsius. Scale bar is 1 mm. Dominant dynamic recrystallization mechanism operative in quartz is SR.

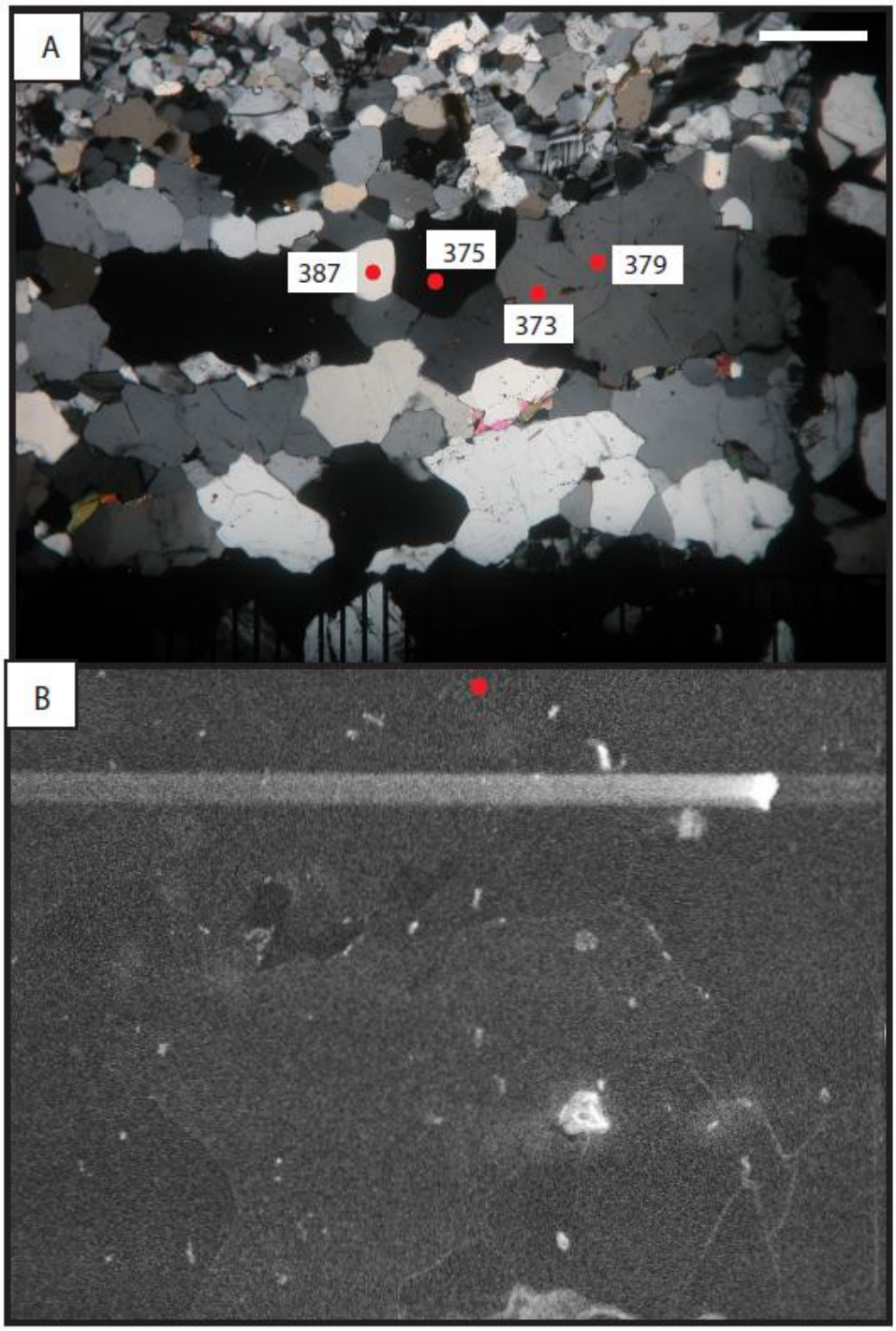

Figure A.14: A) Photomicrograph and B) CL image of sample SC10-32. Temperatures are in degrees Celsius. Scale bar is 500 microns. Dominant dynamic recrystallization mechanism operative in quartz is GBM.

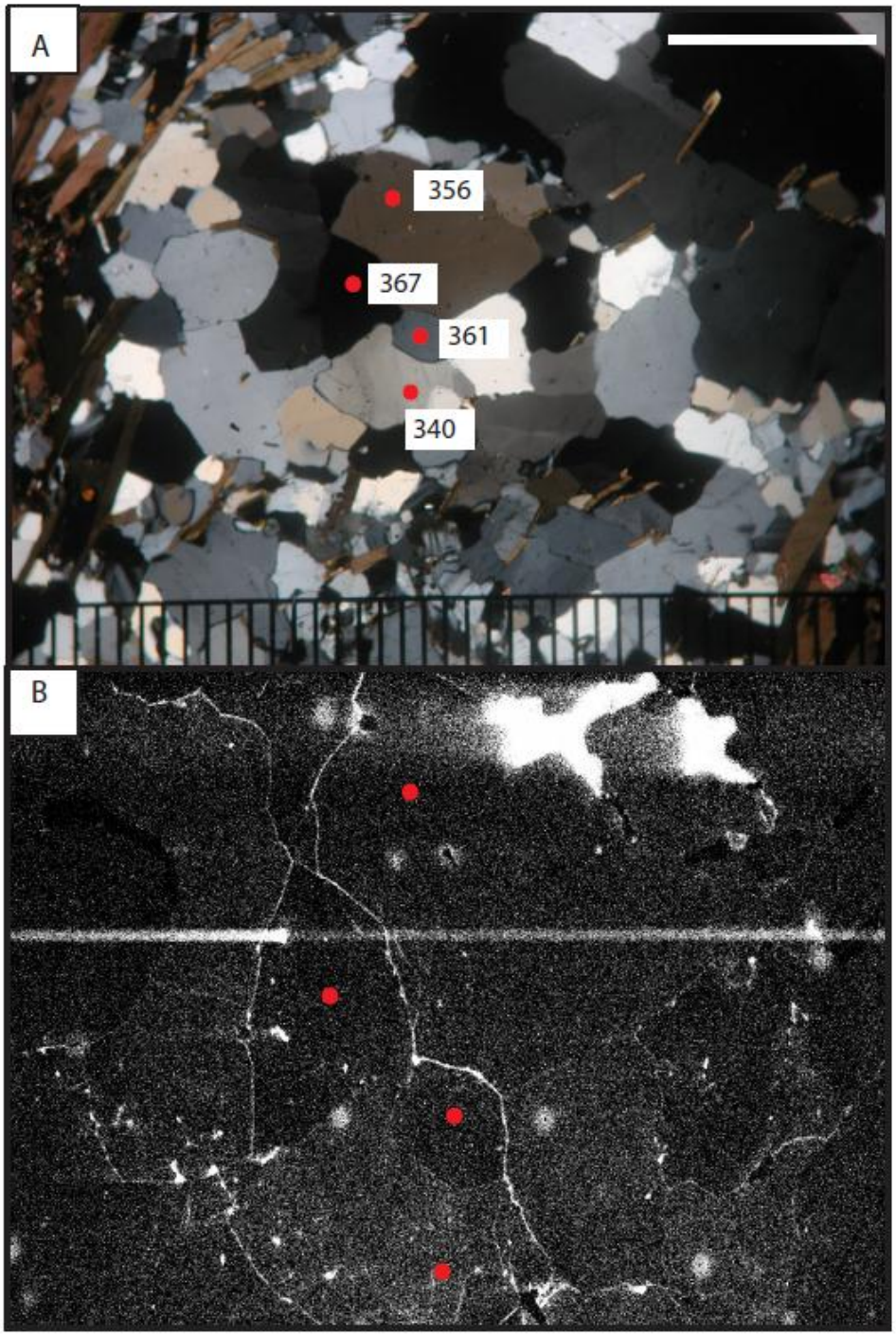

Figure A.15: A) Photomicrograph and B) CL image of sample SC10-33. Temperatures are in degrees Celsius. Scale bar is 1 mm. Dominant dynamic recrystallization mechanism operative in quartz is GBM

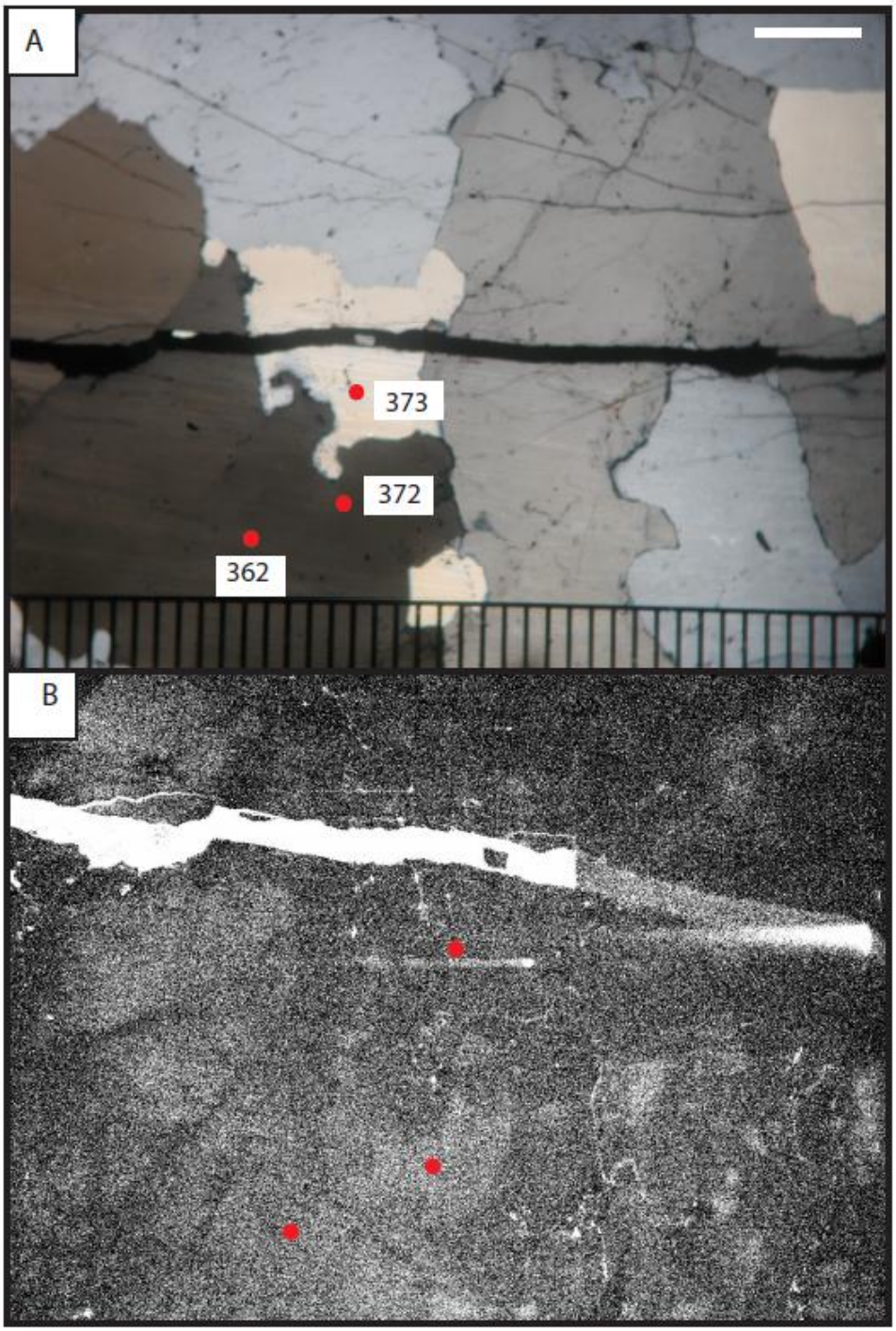

Figure A.16: A) Photomicrograph and B) CL image of sample SC10-34. Temperatures are in degrees Celsius. Scale bar is 500 microns. Dominant dynamic recrystallization mechanisms operative in quartz are BLG and GBM.

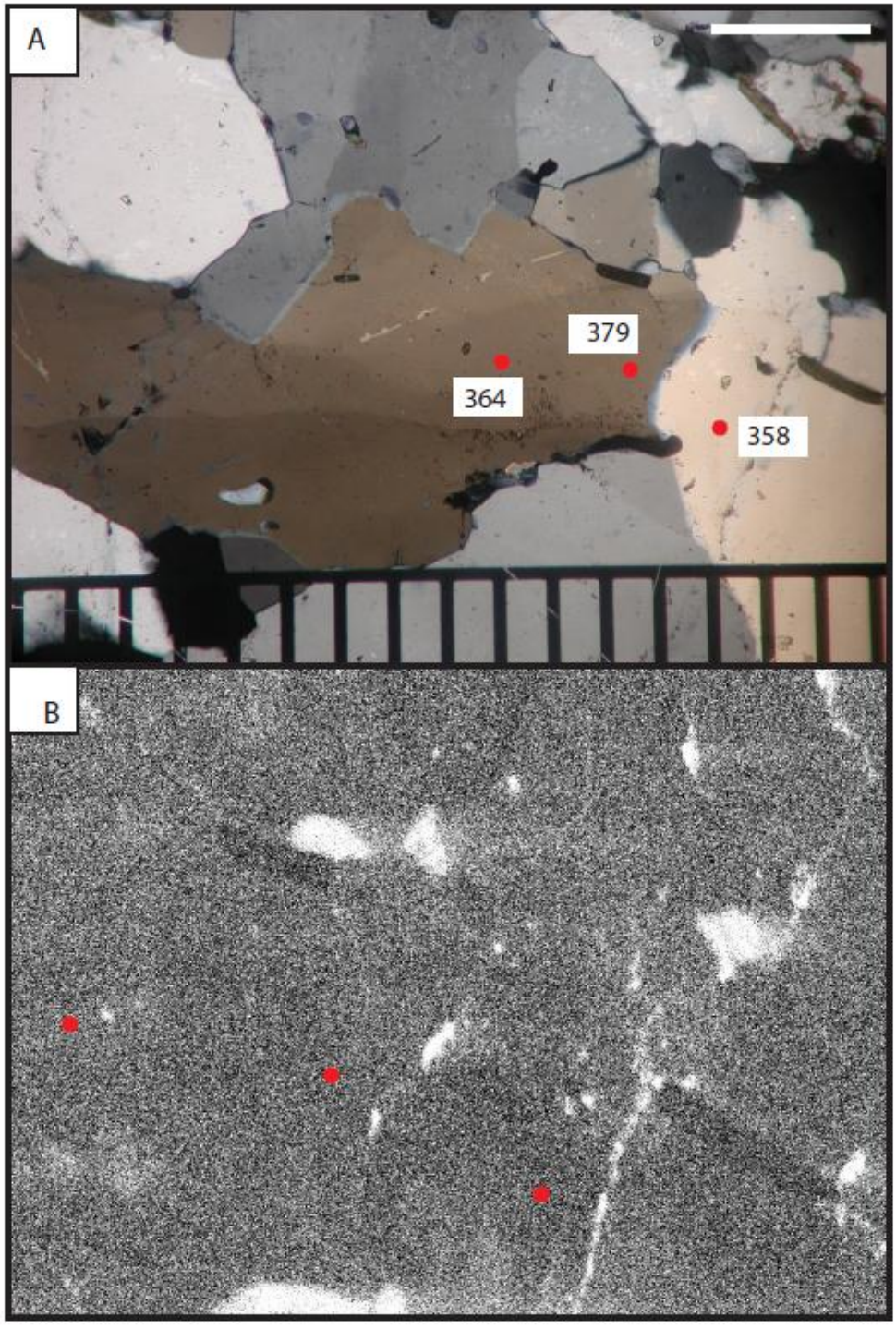

Figure A.17: A) Photomicrograph and B) CL image of sample SC10-35bii. Temperatures are in degrees Celsius. Scale bar is 300 microns. Dominant dynamic recrystallization mechanism operative in quartz is

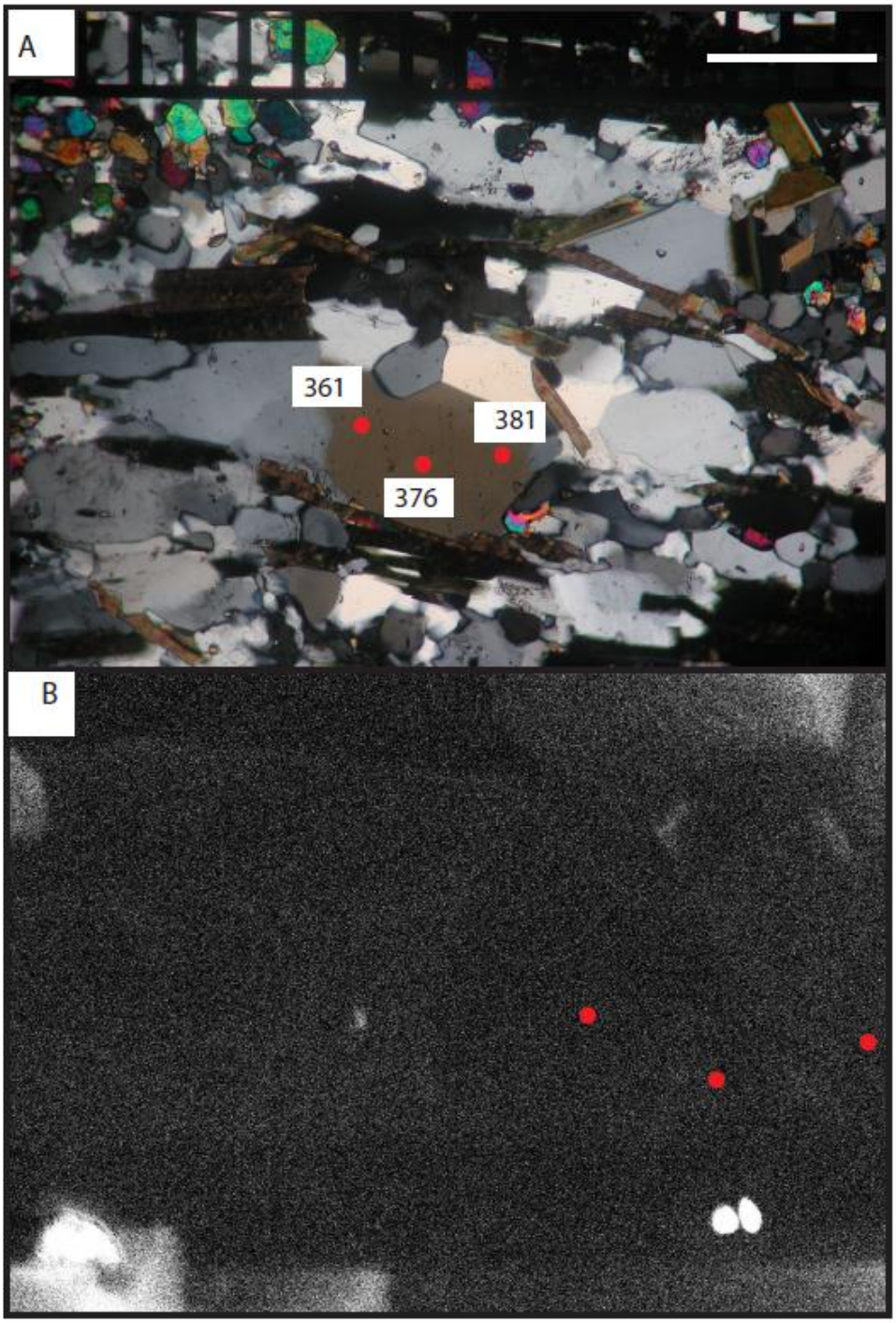

Figure A.18: A) Photomicrograph and B) CL image of sample SC10-38. Temperatures are in degrees Celsius. Scale bar is 300 microns. Dominant dynamic recrystallization mechanism operative in quartz is GBM.

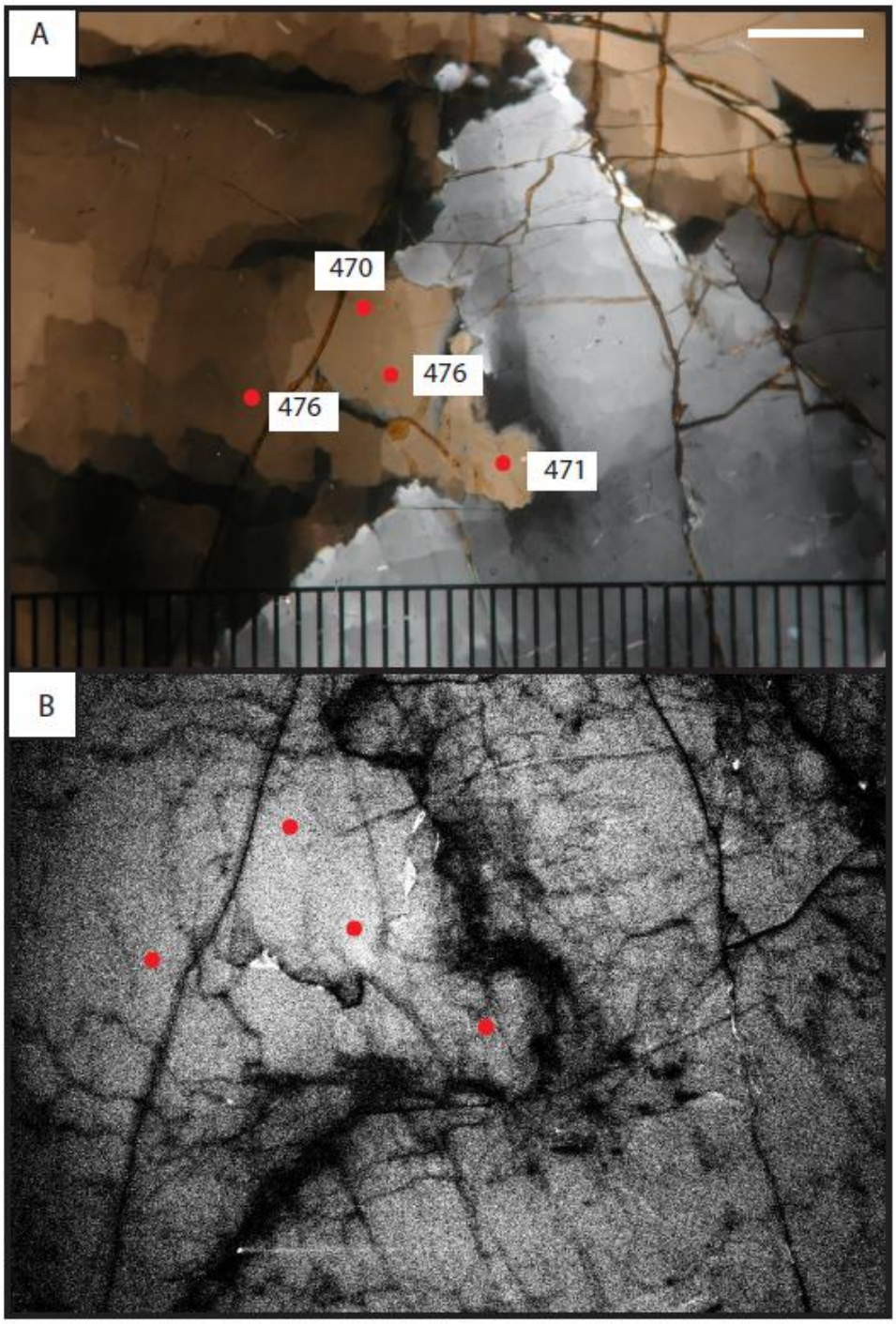

Figure A.19: A) Photomicrograph and B) CL image of sample SC10-45. Temperatures are in degrees Celsius. Scale bar is 500 microns. Dominant dynamic recrystallization mechanism operative in quartz is SR.

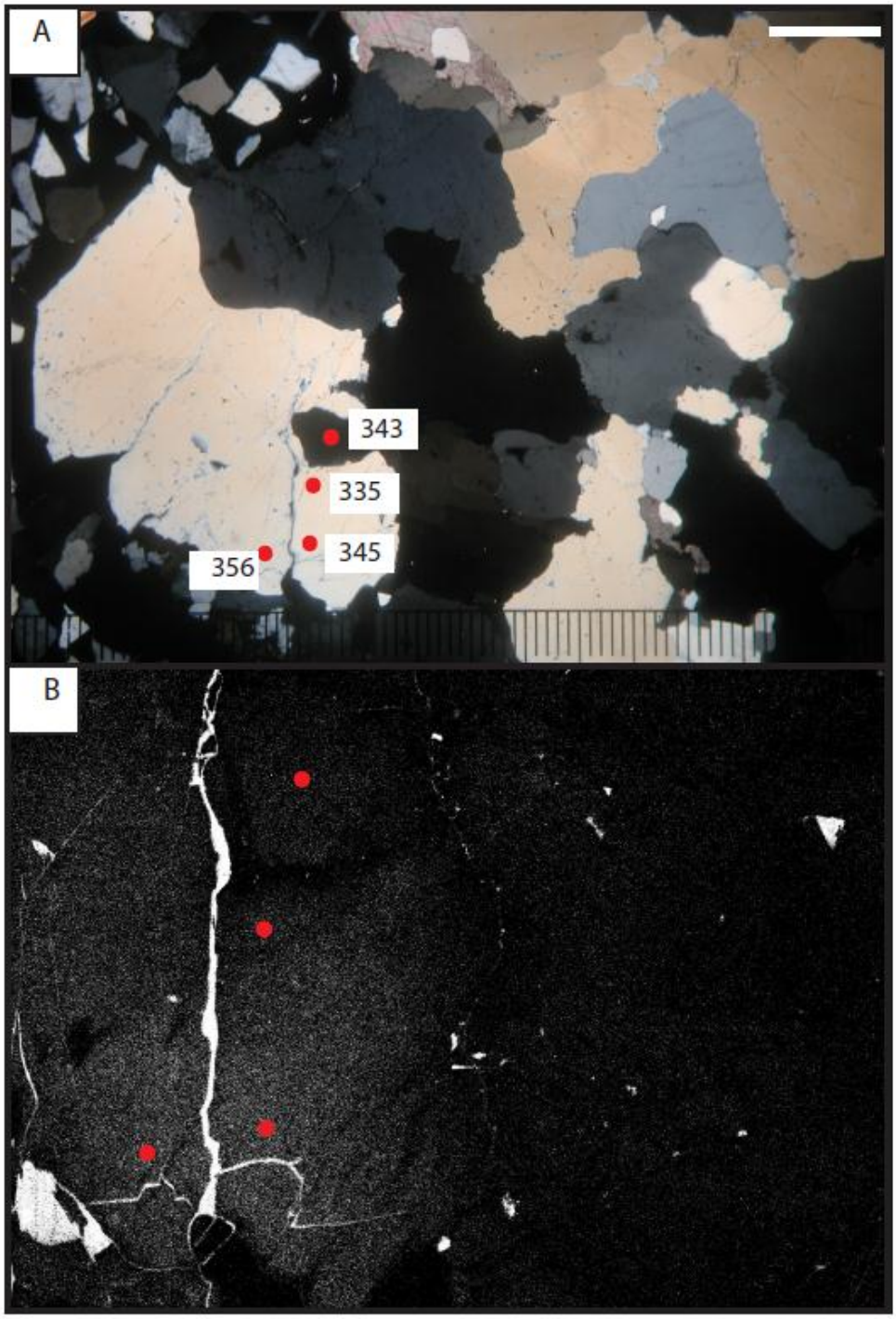

Figure A.20: A) Photomicrograph and B) CL image of sample SC10-46. Temperatures are in degrees Celsius. Scale bar is 1 mm. Dominant dynamic recrystallization mechanism operative in quartz is BLG.

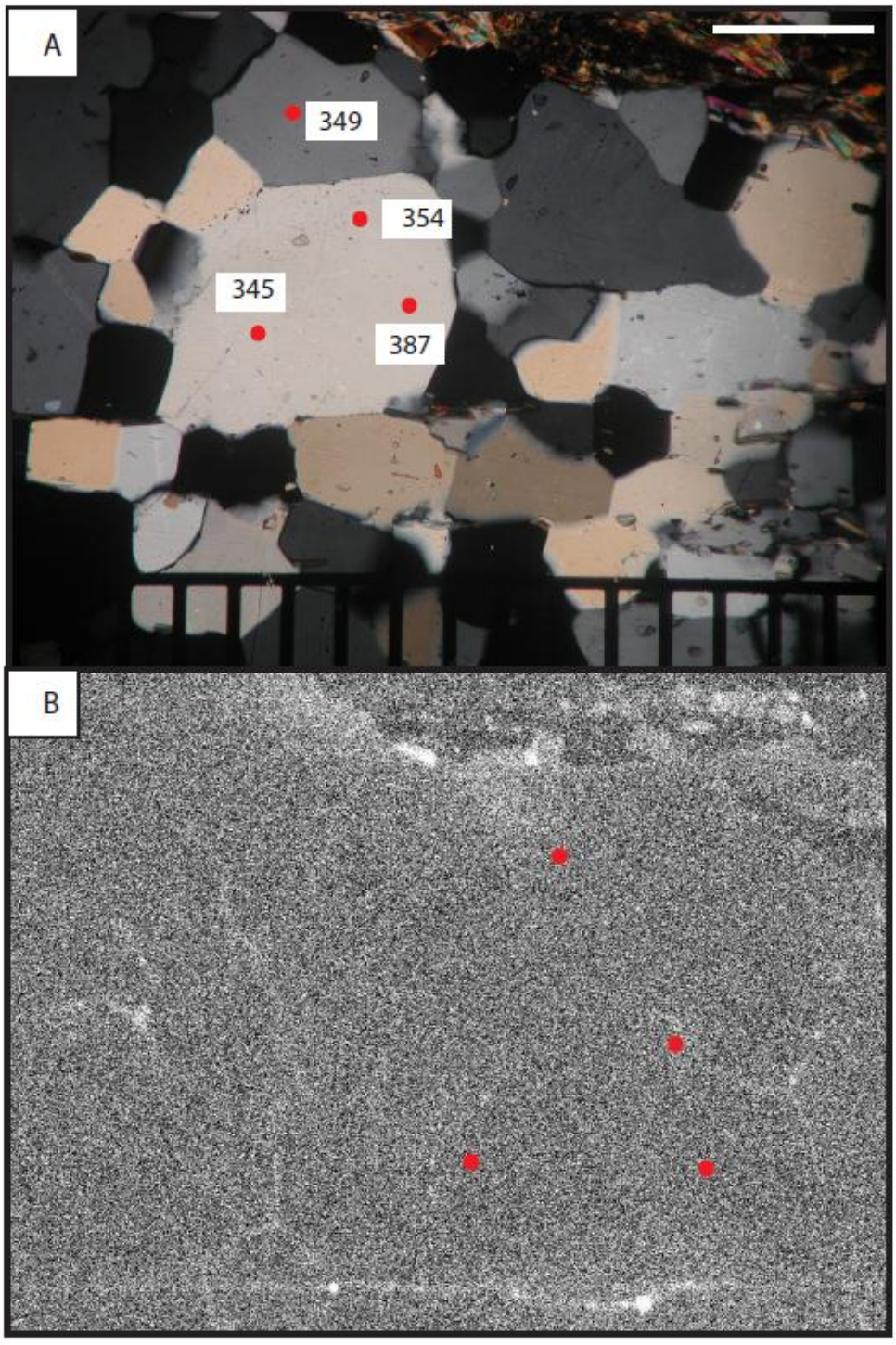

Figure A.21: A) Photomicrograph and B) CL image of sample SC10-48. Temperatures are in degrees Celsius. Scale bar is 300 microns. Dominant dynamic recrystallization mechanism operative in quartz is GBM.

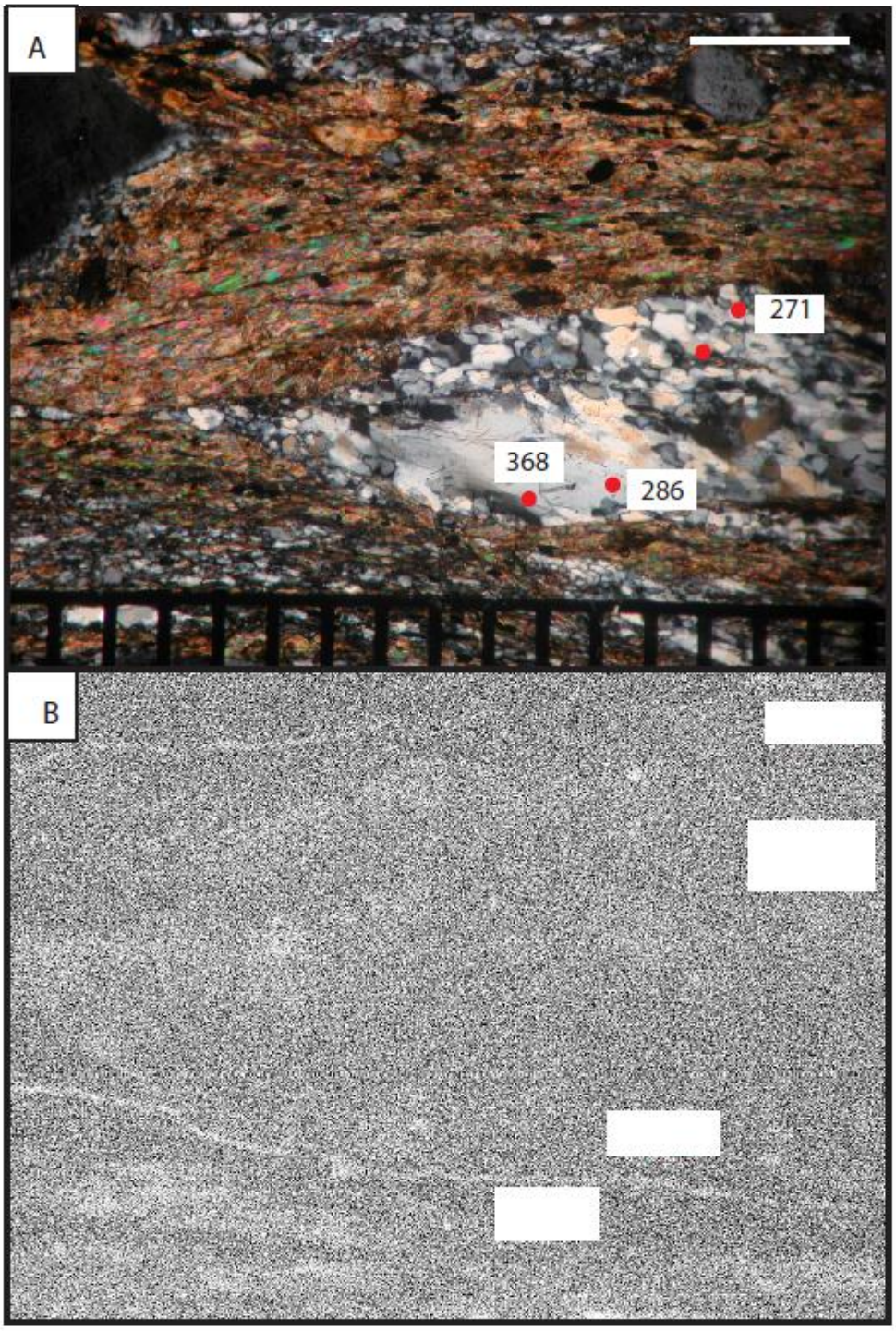

Figure A.22: A) Photomicrograph and B) CL image of sample SC10-49. Temperatures are in degrees Celsius. Scale bar is 300 microns. Dominant dynamic recrystallization mechanism operative in quartz is SR.

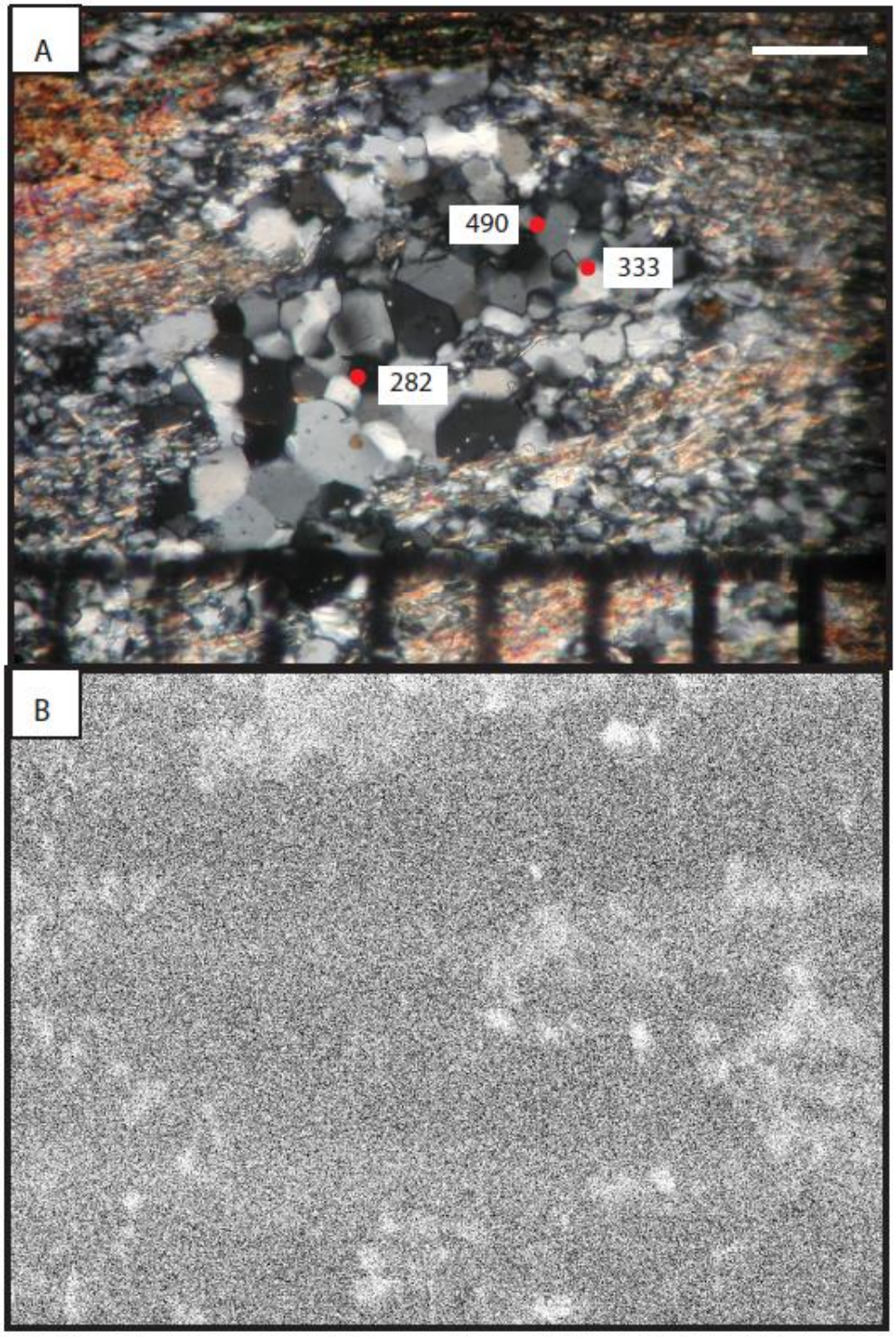

Figure A.23: A) Photomicrograph and B) CL image of sample SC10-51. Temperatures are in degrees Celsius. Scale bar is 100 microns. Dominant dynamic recrystallization mechanism operative in quartz is SR.

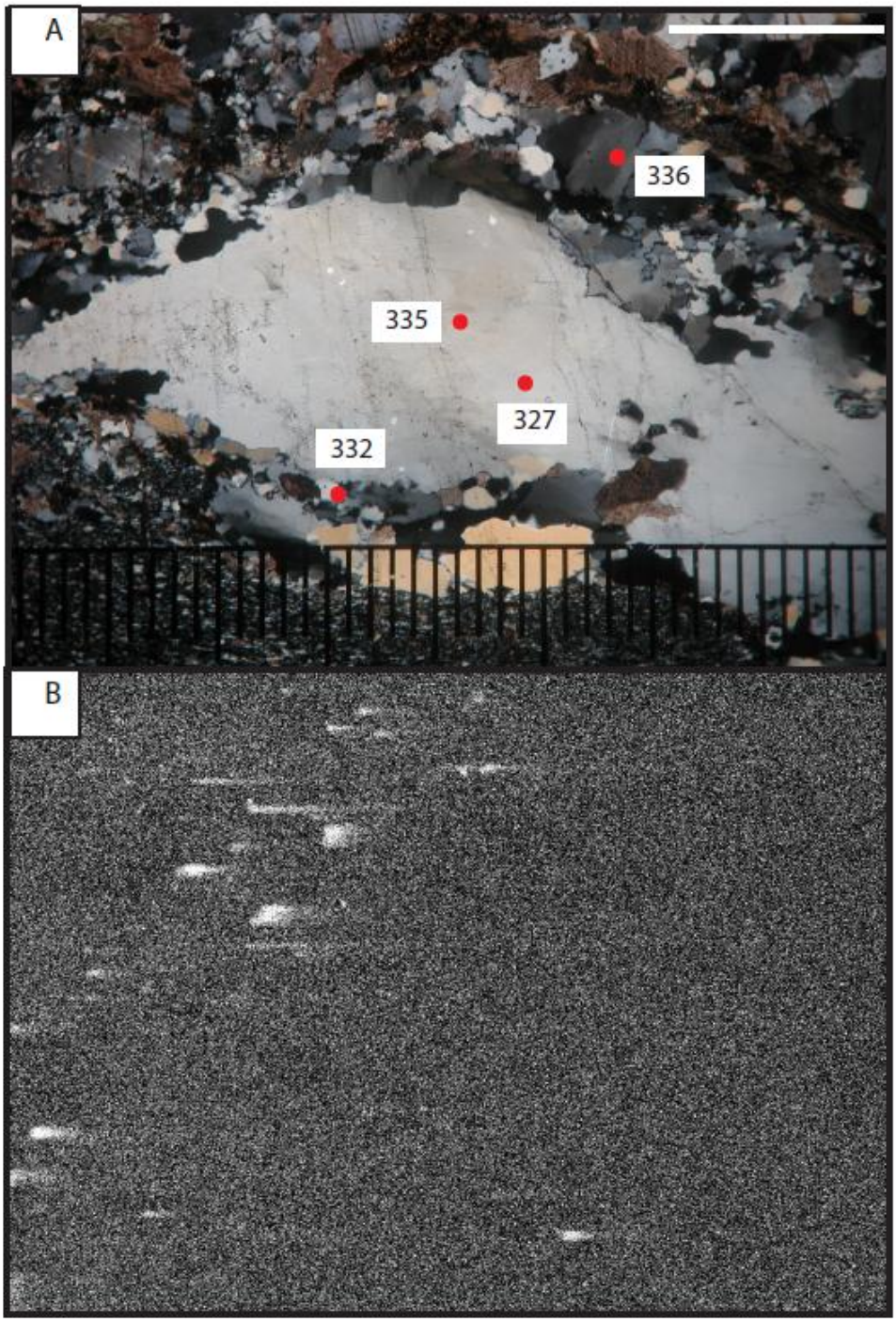

Figure A.24: A) Photomicrograph and B) CL image of sample SC10-55. Temperatures are in degrees Celsius. Scale bar is 1 mm. Dominant dynamic recrystallization mechanism operative in quartz is SR.